

**NONLINEAR STRUCTURAL MECHANICS OF
ELECTRICALLY ACTUATED CARBON NANOTUBE
BASED NEMS DEVICES USING A HIGHER-ORDER
STRAIN GRADIENT THEORY**

BY

ISWAN PRADIPTYA

A Thesis Presented to the
DEANSHIP OF GRADUATE STUDIES

KING FAHD UNIVERSITY OF PETROLEUM & MINERALS

DHAHRAN, SAUDI ARABIA

In Partial Fulfillment of the
Requirements for the Degree of

MASTER OF SCIENCE

In

MECHANICAL ENGINEERING

MAY 2017

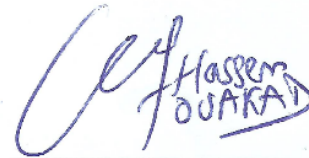
KING FAHD UNIVERSITY OF PETROLEUM & MINERALS


DHAHRAN- 31261, SAUDI ARABIA

DEANSHIP OF GRADUATE STUDIES

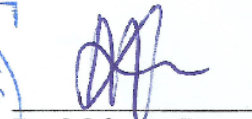
This thesis, written by **ISWAN PRADIPTYA** under the direction his thesis advisor and approved by his thesis committee, has been presented and accepted by the Dean of Graduate Studies, in partial fulfillment of the requirements for the degree of **MASTER OF SCIENCE IN MECHANICAL ENGINEERING.**


Dr. Zuhair M. Gasem
Department Chairman

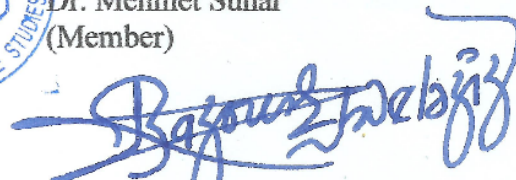

Dr. Hassen M. Ouakad
(Advisor)


Dr. Salam A. Zummo
Dean of Graduate Studies




Dr. Mehmet Sunar
(Member)

6/6/17
Date


Dr. Abdelaziz Bazoune
(Member)

© Iswan Pradiptya
May 2017

Dedicated to

my beloved wife, Ainunni'mah Zen, S.Si., my lovely daughter Kayyisa N. Pradiptya

and all of my brothers

ACKNOWLEDGMENTS

All praises and worship are for Allah, the most Beneficent, the Most Merciful. *Shalawat* and blessing be upon khotimul anbiya' Muhammad *shalallahu 'alaihi wa sallam*, his family, his companions, and all those who follow him.

I would like to thank my parents in-laws, Zainal M. Idris, L.c. and Umi Latifah, for their continuous supports and caring my wife and my lovely daughter during my study. A special thanks and billions of love to my beloved wife and daughter for her patience and love. She always support my ambition to reach higher education.

I deeply thank my academic advisor Dr. Hassen M. Ouakad for the continuous guidance and all the efforts. I am also indebted to him for his patience in teaching, discussions, inspirations, supports, and encouragement during my master program.

I express my appreciation to Dr. Abdelaziz Bazoune and Dr. Mehmet Sunar for the time and consideration to be part of thesis committee members. Thank for their evaluations, valuable advice and suggestions.

I owe many thanks to Dr. -Ing. Ismoyo Haryanto (University of Diponegoro), Dr. Achmad Widodo (University of Diponegoro) and Joga D. Setiawan, Ph.D. (Petronas University) for their recommendations, motivations, fruitful discussions, and their kind friendship.

I would like to express my appreciation to Mr. Suharto (formerly as Head of Division for Talent, PT. PLN Persero) and Mr. Eddy D. Erningpraja (formerly as

Director of Human Resources and General, PT. PLN Persero) for giving me a chance to pursue my master degree.

I would also like to thank Deanship of Scientific Research, KFUPM for the financial support during the IEEE MESA2016 oral presentation in Auckland, Zealand.

Millions of thanks should go to Mr. Muflih A. Adnan, Mr. Tri Bagus Susilo, Mr. Dwi Budi Suyanto, Mr. Dian Sumarhadi, Mr. Janu Prasetyo and all the families in VIP Membership++ PLN JMK JTBN , for the warm brotherhoods, supports and all the helps their provided.

I also thank to Mr. Tausif, Mr. Hammam, Mr. Binash, Mr. Aviandy, Lutfi Aziz, Rama Rizana, Pramoedya, and all the colleagues in Persatuan Pelajar dan Mahasiswa Indonesia (PPMI), Dhahran, KSA for their support and friendship.

TABLE OF CONTENTS

ACKNOWLEDGMENTS	v
TABLE OF CONTENTS	vii
LIST OF TABLES	x
LIST OF FIGURES	xi
LIST OF SYMBOLS	xv
ABSTRACT (ENGLISH).....	xix
ABSTRACT (ARABIC)	xxi
CHAPTER 1: INTRODUCTION.....	1
1.1 Motivation	1
1.2 Literature Review	5
1.2.1 Nanoresonators	5
1.2.2 Nanosensors.....	7
1.2.3 Nanoactuators	8
1.2.4 Size-dependent effects on the CNT-based nanobeam modeling.....	9
1.2.5 Temperature gradient effect.....	13
1.3 Thesis Objective and Organization	14
CHAPTER 2: BACKGROUND	16
2.1. The Classical Continuum Model of Beam	16
2.2. A short review of strain gradient elasticity theory	19
2.3. Thermal Gradient Effects	22
CHAPTER 3: PROBLEM DEFINITION, MODELING AND SOLUTION	
METHODOLOGY	23
3.1. Equation of Motion of Doubly Clamped Slacked CNT-based Nanobeam	23
3.1.1. Non-classical strain energy density derivation.....	24
3.1.2. The kinetic energy and work of non-conservative forces.....	28
3.1.3. Hamilton’s principle	29
3.2. Galerkin’s Modal Decomposition	32

3.3. Non-classical Mode Shapes.....	34
CHAPTER 4: STATIC ANALYSIS.....	38
4.1. The Size Scale Dependent Parameter Effects on the CNT Mode Shape	38
4.1.1. The size scale dependent effects on the mode shape parameters	38
4.1.2. The non-classical mode shape	40
4.2. Size Scale Dependent Parameter Effects.....	42
4.2.1. Numerical example and convergences	44
4.2.2. Size scale dependent effects on the maximum static deflection.....	47
4.3. The temperature gradient effects.....	51
4.3.1. Temperature gradient effect to the pull-in voltage and maximum static deflection	51
4.3.2. The critical temperature buckling analysis	54
CHAPTER 5: EIGENVALUE PROBLEM	57
5.1. Linearized Eigenvalue Problem Derivation	57
5.2. Linearized Eigenvalue Problem of straight CNT	60
5.2.1. Considering one mode LEVP using classical continuum theory	60
5.2.2. Considering five mode LEVP using classical continuum theory	62
5.2.3. Considering five mode LEVP using strain gradient theory.....	64
5.3. Linearized Eigenvalue Problem of Slacked CNT	67
5.3.1. Considering classical theory.....	68
5.3.2. Considering strain gradient theory	69
5.4. Thermal Gradient Effects on The Natural Frequency of CNT-based Nanobeam....	76
5.4.1. Considering one mode LEVP	76
5.4.2. Considering five mode LEVP.....	79
CHAPTER 6: DYNAMIC ANALYSIS.....	85
6.1. Reduced Order Model Prescription for Dynamic Analysis.....	85
6.1.1. Classical continuum theory	85
6.1.2. Strain gradient theory	87
6.2. Dynamic Response	89
6.2.1. The size scale dependent effect	89
6.2.2. The effect of alternating current gate voltage (V_{AC})	93

6.2.3. The effect of quality factor (Q).....	95
CHAPTER 6: DYNAMIC ANALYSIS.....	96
7.1. Conclusions	96
7.2. Future Recommendations	98
Appendix.....	99
REFERENCES.....	111
VITAE.....	119

LIST OF TABLES

Table 4.1:	The assumed CNT geometrical properties used to simulate the results of Figure 4.3	41
Table 4.2:	Geometrical properties of the case studies of CNTs considered in this work.....	45
Table 4.3:	Effect of the temperature gradient variation on the CNT pull-in gate voltage and its respective normalized maximum deflection.	52

LIST OF FIGURES

Figure 2.1:	Comparison of the static deflection of cantilever microbeams based on classical continuum, couple stress, and strain gradient theories and for various beam thickness h : (a) $h = 20 \mu\text{m}$; (b) $h = 50 \mu\text{m}$; (c) $h = 100 \mu\text{m}$; (d) $h = 200 \mu\text{m}$ [81].	21
Figure 3.1:	Schematic of a doubly clamped CNT based nanobeam assuming parallel-plates electrostatic actuation.	24
Figure 3.2:	Variation of the first four real roots with small values of the tuning parameter β_0 .	35
Figure 3.3:	Variation of the first six imaginary roots with small values of the tuning parameter β_0 .	36
Figure 4.1:	Comparison of the variation of the square root of the first frequency when assuming classical and non-classical beam equation as well as two set of non-classical boundary conditions.	39
Figure 4.2:	Variation of the absolute value of the first, second, and third characteristic roots of the eigenvalue problem when assuming classical and non-classical beam equation as well as two set of non-classical boundary conditions.	41
Figure 4.3:	Comparison between the CNT classical and non-classical mode shapes assuming the geometrical properties of Table 4.1.	42
Figure 4.4:	Variation of the normalized maximum static deflection of the CNT with the DC voltage for case 1 of Table 4.2, when assuming classical continuum theory, and for various number of modes in the ROM.	46
Figure 4.5:	Variation of the normalized maximum static deflection of the CNT with the DC voltage for case 1 of Table 4.2, when assuming non-classical continuum (strain gradient) theory, and for various number of modes in the ROM.	46
Figure 4.6:	Comparison of the normalized maximum static deflection variation of the CNT with the DC voltage when assuming the classical continuum theory (CCT) and the strain gradient theory (SGT) for cases 1, 2, and 3 of Table 4.2, respectively.	48
Figure 4.7:	Comparison of the normalized maximum static deflection variation of the CNT with the DC voltage when assuming the classical continuum theory (CCT) and the strain gradient theory (SGT) for case 4 of Table 4.2.	49
Figure 4.8:	Comparison of the CNT static profiles of cases 1, 2 and 3 of Table 4.2, for DC gate voltage of 16 <i>Volt</i> , and when considering the	

	classical continuum theory (CCT), and the strain gradient theory (SGT), respectively.....	50
Figure 4.9:	Thermal gradient effect on the CNT maximum static deflection of case 5 of Table 4.2 when assuming low-temperature regime.....	53
Figure 4.10:	Thermal gradient effect on the CNT maximum static deflection of case 5 of Table 4.2 when assuming high-temperature regime.	54
Figure 4.11:	Variation of CNT maximum static deflection with an assumed temperature gradient excitation and while assuming a SGT parameters of $l_0 = l_1 = l_2 = l = 1 \text{ nm}$	56
Figure 4.12:	Variation of the CNT maximum static deflection with an assumed temperature gradient excitation and while varying the strain gradient parameters as follows: $l = 0 \text{ nm}$ (the classical continuum theory case), $l = 1.0 \text{ nm}$, $l = 1.25 \text{ nm}$, and $l = 1.5 \text{ nm}$	56
Figure 5.1:	Variation of the first in-plane (fundamental) natural frequency with the DC load of the CNT of case 1 of Table 4.2 assuming the classical continuum theory.....	61
Figure 5.2:	Variation of the first in-plane (fundamental) natural frequency with the DC load of the CNT of case 3 of Table 4.2 assuming the classical continuum theory.....	62
Figure 5.3:	Variation of the first five in-plane natural frequencies with the DC load assuming the classical continuum theory of the CNT of (a) case 1 from Table 4.2. (b) case 3 from Table 4.2.....	63
Figure 5.4:	Variation of the first in-plane (fundamental) natural frequency with the DC load of the CNT of case 2 from Table 4.2 [95] assuming both the classical continuum theory and the strain gradient theory: (a) nondimensional form, and (b) dimensional form (in <i>MHz</i>).....	65
Figure 5.5:	Variation of the second in-plane natural frequency with the DC load of the CNT of case 2 from Table 4.2 [95] assuming both the classical continuum theory and the strain gradient theory: (a) nondimensional form, and (b) dimensional form (in <i>MHz</i>).	66
Figure 5.6:	Variation of the second, third, fourth and fifth in-plane natural frequencies (in <i>MHz</i>) with the DC load of the CNT of case 2 from Table 4.2 [95] assuming both the classical continuum theory and the strain gradient theory.	67
Figure 5.7:	Variation of the first five nondimensional in-plane natural frequencies with the slack level and for zero DC load of the CNT of case 8 from Table 4.2 assuming the classical continuum theory.	69
Figure 5.8:	Variation of the first five nondimensional in-plane natural frequencies with the slack level and for zero DC load of the CNT of case 8 from	

	Table 4.2 assuming the strain gradient theory (SGT) with: (a) $l = 1.0 \text{ nm}$, and (b) $l = 1.5 \text{ nm}$	70
Figure 5.9:	Variation of the modes-veering and modes-crossing locus with the SGT size dependent parameter and while assuming: (a) dimensional slack level b_0 in nm , and (b) slack levels in percentage.....	72
Figure 5.10:	Variation of the first five nondimensional in-plane natural frequencies with the DC load, for a slack level of $b_0 = 30 \text{ nm}$ of the CNT of case 8 from Table 4.2 while assuming: (a) the classical continuum theory $l = 0 \text{ nm}$, (b) the strain gradient theory $l = 1.0 \text{ nm}$, and (c) the strain gradient theory $l = 1.5 \text{ nm}$	74
Figure 5.11:	Variation of the first five nondimensional in-plane natural frequencies with the DC load, for a slack level of $b_0 = 60 \text{ nm}$ of the CNT of case 8 from Table 4.2 while assuming: (a) the classical continuum theory $l = 0 \text{ nm}$, (b) the strain gradient theory $l = 1.0 \text{ nm}$, and (c) the strain gradient theory $l = 1.5 \text{ nm}$	75
Figure 5.12:	Variation of the first nondimensional in-plane (fundamental) natural frequency with the DC load, for zero slack level of the CNT of case 5 from Table 4.2 and for various low temperature gradients, and while assuming SGT with $l = 1 \text{ nm}$	78
Figure 5.13:	Variation of the first nondimensional in-plane (fundamental) natural frequency with the DC load, for zero slack level of the CNT of case 5 from Table 4.2 and for various high temperature gradients, and while assuming SGT with $l = 1 \text{ nm}$	79
Figure 5.14:	Variation of the normalized first five in-plane natural frequencies with various higher temperature gradients, for zero DC load, and while assuming SGT with $l = 1 \text{ nm}$	80
Figure 5.15:	Variation of the first five nondimensional in-plane natural frequencies with the DC load, for a straight CNT ($b_0 = 0 \text{ nm}$) of case 8 from Table 4.2 assuming a strain gradient theory with $l = 1.0 \text{ nm}$, and for (a) $\Delta T_{high} = 0 \text{ K}$ (room temperature condition), (b) $\Delta T_{high} = 200 \text{ K}$, and (c) $\Delta T_{high} = 400 \text{ K}$	81
Figure 5.16:	Variation of the first five nondimensional in-plane natural frequencies with the DC load, for a straight CNT ($b_0 = 0 \text{ nm}$) of case 8 from Table 4.2 assuming a strain gradient theory with $l = 1.0 \text{ nm}$, and for (a) $\Delta T_{low} = -200 \text{ K}$, and (b) $\Delta T_{low} = -400 \text{ K}$	84
Figure 6.1:	Time history curve of the maximum dynamic response of the CNT of case 1 of Table 4.2 at a forcing frequency of $\Omega \approx 22$, forcing amplitude of $V_{DC} = V_{AC} = 2 \text{ Volt}$, a SGT parameter of $l = 1 \text{ nm}$, and a quality factor of $Q = 100$	90

Figure 6.2:	Frequency-response curve of the CNT of case 1 of Table 4.2 for various strain gradient parameters values, $V_{DC}=V_{AC}=2$ Volt, and a quality factor of $Q = 100$	91
Figure 6.3:	Frequency-response curve of the CNT of case 3 of Table 4.2 for various strain gradient parameters values, $V_{DC}=V_{AC}=0.25$ Volt, and a quality factor of $Q = 100$	92
Figure 6.4:	Frequency-response curve of the CNT of case 8 of Table 4.2 for various strain gradient parameters values, $V_{DC}=10$ milliVolt, $V_{AC}=2$ milliVolt, and a quality factor of $Q = 100$	93
Figure 6.5:	Frequency-response curve for case 1 of Table 4.2 showing the effect of V_{AC} and considering a quality factor of $Q = 100$ and $V_{DC}=2$ Volt and assuming SGT parameter of $l = 0.8$ nm.....	94
Figure 6.6:	Frequency-response curve for case 3 of Table 4.2 showing the effect of V_{AC} and considering a quality factor of $Q = 100$ and $V_{DC}=0.25$ Volt and assuming SGT parameter of $l = 0.8$ nm.....	94
Figure 6.7:	The effect of quality factor (Q) on the frequency response curve for case 3 of Table 4.2, considering the voltage values of $V_{AC} = 0.25$ Volt and $V_{DC}= 1$ Volt and assuming SGT parameter of $l = 0.8$ nm.	95

LIST OF SYMBOLS

A	Cross-sectional area
b	Nondimensional maximum initial slack
b_0	Maximum initial slack
c	Normalized damping coefficient (in the beam classical theory)
\tilde{c}	Viscous damping coefficient (in the beam classical theory)
C	Matrix constants of the mode shape
C_i	i^{th} constant coefficient of the mode shape function, i is indices
C_v	Viscous damping
\hat{C}_v	Normalized viscous damping
C_s	Structural damping
\hat{C}_s	Normalized structural damping
d	Gap width between bottom electrode and axis- x
E	Young's modulus
$F(t)$	External force per unit length
$F_{ax}(x, t)$	Axial force
$F_e(x, t)$	Electrostatic force
G	Lame constant for torsional rigidity
h	Shell thickness
I	Cross-sectional moment of inertia

I_{matrix}	Identity matrix
I_y	Moment of inertia respect to axis-y
J	Jacobian's Matrix
L	CNT effective length of the CNT in the straight state
L'	CNT length in the deformed/slacked state
l_0	Size scale gradient parameter which is related to dilatation gradient
l_1	Size scale gradient parameter which is related to deviatoric stretch gradient
l_2	Size scale gradient parameter which is related to rotation gradient
\mathbf{m}_{pq}	Second-order tensor quantity which is related to rotation gradient tensor
m_i	Roots of the characteristic Eq. (3.44), $i=1,2,3,4,5,6$
M	Bending moment
\mathbf{P}_p	Vector quantity which is related to dilatation gradient tensor
Q	Quality factor of the resonator
r	Radius of the CNT
\hat{r}	Normalized/nondimensional radius of the CNT
t	Time (second)
\hat{t}	Dimensionless time
$T_{classic}$	Time constant in classical theory as defined in Eq. (2.9)
T	Time constant in strain gradient theory as defined in Eq. (3.33)
U	Modal coordinate vector
$u(x,t)$	Axial displacement in the direction of axis-x

u_i	Displacement field in the framework of Euler-Bernoulli beam, $i=1,2,3$
$u_{1 \leq i \leq n}(t)$	Modal coordinates
U_A	Axial strain energy due to residual axial stresses
w	Transversal deflection of the beam
\hat{w}	Nondimensional transversal deflection of the beam
w_0	Initial slack function
\hat{w}_0	Nondimensional initial slack function
α_1	Constant coefficient of mid-plane stretching term in the classical beam equation of motion
α_2	Constant coefficient of electrostatic force term in the classical beam equation of motion
α_T	Coefficient of thermal expansion (CTE) of the CNT
β_0	Constant coefficient of the sixth-order partial derivation term in the strain gradient beam equation of motion
β_1	Constant coefficient of mid-plane stretching term in the strain gradient beam equation of motion
β_2	Constant coefficient of temperature gradient effect in the strain gradient beam equation of motion
β_3	Constant coefficient of electrostatic force term in the strain gradient beam equation of motion
Υ_p	Dilatation gradient vector
δ_{ij}	Kronecker delta
$\delta(f)$	Variational quantity of f

ε_0	Air dielectric constant
ε_{ij}	Strain tensor quantity (row- i^{th} and column- j^{th})
η_{pqr}^1	Deviatoric stretch gradient (third-order tensor quantity), where p , q , and r are tensor indices
ν	Poisson's ratio
ρ	Mass density of the carbon nanotube
σ_{ij}	Cauchy stress tensor quantity (row- i^{th} and column- j^{th})
τ_{pqr}^1	Third-order stress tensor, where p , q , and r are indices
ϕ_i	i^{th} mode shape function
χ_{pq}	Gradient of rotation tensor, where p and q are indices
ω_i	i^{th} natural frequency
Ω	AC harmonic frequency (dimensional)
$\hat{\Omega}$	AC harmonic frequency (nondimensional)

ABSTRACT

Full Name : Iswan Pradiptya
Thesis Title : Nonlinear Structural Mechanics of Electrically Actuated Carbon Nanotube based NEMS Devices
Major Field : Mechanical Engineering
Date of Degree : May 2017

This thesis aims to investigate the nonlinear size dependent behavior of electrically carbon nanotubes (CNTs) based nanoelectromechanical systems (NEMS) while including higher-order strain gradient deformations, the geometric nonlinearity due to the von Karman nonlinear strain as well as the slack (initial curvature) and temperature gradient effects. The assumed non-classical beam model adopts some internal material length scale parameters related to the material nanostructures and is capable of interpreting the size effect that the classical continuum beam model is unable to pronounce. The higher-order governing equations of motion and boundary conditions are derived using the so-called Hamilton principle. A Galerkin modal based reduced-order model (ROM) expansion is developed to prescribe the non-classical nanotube mode shape as well as its static behavior under any applied DC actuation voltage. Results of the static analysis is compared with those obtained by the classical elasticity continuum theory. Then, a Jacobian method is utilized to determine the variation of the natural frequencies of the nanobeam with the DC load as well as the slack level. A detailed parametric study is conducted to study the influences of the size scale dependent parameters, the CNT length-to-radius ratio, the slack level and temperature gradients on the free vibration characteristics of the nanobeam. Moreover, a forced vibration analysis using long time

integration is conducted to investigate the strain gradient effect mainly in the linear regime. It is found that the size effect based on the strain gradient deformation has significant influence on static deflection responses, the fundamental nanotube natural frequencies dispersion as well as the dynamical behavior of the CNT-based nanobeam. Also, varying this size effect have revealed the offering of numerous possibilities of modes veering and crossing, all shown to be dependent of the strain gradient parameters as well as the CNT slack level. In addition, taking into account the size scale dependent effect change the nonlinearity profile of the frequency response analysis.

This research may allow better understanding of the nonlinear behavior of CNT-based nanosystem and can guide NEMS engineers in the design consideration stage, accordingly.

ملخص الرسالة

الإسم الكامل	:	إسوان براديبنتيا
عنوان الرسالة	:	الميكانيكا الإنشائية غير الخطية للأجهزة الكهروميكانيكية النانوية على أساس أنابيب الكربون النانوية المثارة كهربائياً
التخصص	:	هندسة ميكانيكية
تاريخ الدرجة العلمية	:	شعبان 1438 هـ

تقترح هذه الرسالة التحقيق في السلوك غير الخطي المعتمد على الحجم لأنابيب الكربون النانوية (CNT) المثارة كهربائياً على أساس عارضة نانوية مع تضمين تشوه إنحدار الإنفعال ذو الطراز الأعلى، الهندسة غير الخطية الناتجة عن إنفعال فون كارمان غير الخطي، بالإضافة إلى تأثير الركود، وتأثيرات إنحدار درجة الحرارة. ويتبنى نموذج العارضة غير التقليدي المفترض بعض متغيرات مقياس طول المواد الداخلية متعلقة بالتركيب الداخلي النانوي وهو قادر على تفسير تأثير الحجم الذي لا يستطيع نموذج العارضة التقليدي المستمر على بيانه. المعادلات الحاكمة للحركة ذات الدرجة العليا تم اشتقاقها باستخدام ما يسمى بمبدأ هاميلتون. تم تطوير نموذج تحليلي منخفض الدرجة (ROM) على أساس غالركين لوصف هيئة النمط (الونيرة) غير الكلاسيكية وكذلك سلوكها السكوني (المتسقر) تحت تطبيق (تنفيذ) أي حمل تشغيل ذو تيار مباشر. تمت مقارنة نتائج التحليل السكوني مع تلك التي تم الحصول عليها من خلال نظرية استمرارية المرونة الكلاسيكية. ثم تم استخدام طريقة جاكوبي لتحديد التغيير في الترددات الطبيعية للعارضة النانوية مع حمل التيار المباشر وكذلك مستوى الركود. وقد أجريت دراسة تفصيلية بارامترية لدراسة تأثيرات المعاملات (المتغيرات) المعتمدة على مقياس الحجم، نسبة طول أنابيب الكربون النانوية إلى نصف قطرها، مستوى الركود وانحدارات درجات الحرارة على خصائص الاهتزاز الحر لأنابيب الكربون النانوية. علاوة على ذلك، تم إجراء تحليل الإهتزاز القسري الخطي باستخدام تكامل طويلة المدة لتقصي تأثير إنحدار الإنفعال في المنطقة الخطية. وُجد أن تأثير الحجم على أساس تشوه إنحدار الإنفعال له تأثير كبير على استجابات الانحراف السكوني، وتشنت (تتاثر) الترددات الطبيعية الأساسية لأنابيب الكربون النانوية بالإضافة إلى السلوك الديناميكي للعارضة النانوية القائمة على أنابيب الكربون النانوية. أيضاً، قد أظهر تغيير تأثير الحجم هذا عرض

(تقديم) العديد من الاحتمالات من انماط الإنحراف ونقاط التقاطع ، وكلها أظهرت أنها تعتمد على عوامل انحدرت الإنفعال المتغيرة بالإضافة إلى مستوى ركود انابيب الكربون النانوية. بالإضافة إلى ذلك، مع الأخذ بعين الاعتبار التأثير المعتمد على مقياس الحجم يغيّر المظهر غير الخطي لتحليل استجابة التردد. هذا البحث قد يسمح بفهم أفضل للسلوك غير الخطي للأنظم النانوية على اساس انابيب الكربون النانوية ويمكن أن يوجه مهندسين الأجهزة الكهروميكانيكية النانوية في مرحلة إعتبرات التصميم وفقا لذلك.

CHAPTER 1

INTRODUCTION

In this chapter, a preliminary background, main interest, and motivation of the thesis are presented. An adequate literature survey is also cited to overview the main contributions of the CNT-based continuum models development. The literature survey is including few technical applications of the use of CNT-based nanobeam devices, the applicability of the continuum elasticity theory to model the structural behaviors of CNT in a certain condition, the size scale dependent effect of small structure modeling, and the temperature gradient effects. In the last sub-section of this chapter, the objectives of the research are outlined.

1.1 Motivation

The era of nanotechnology was inspired by the following famous Richard Feynman's speech entitled "There's Plenty of Room at the Bottom" in 1959 [1]:

"I would like to describe a field, in which little has been done, but in which an enormous amount can be done in principle. This field is not quite the same as the others. Furthermore, a point that is most important is that it would have an enormous number of technical applications. What I want to talk about is the problem of manipulating and controlling things on a small scale."

Richard Feynman

He announced to the entire world the possibility of manipulating and controlling things in the small scales (sub-macro scales). Nowadays people call this term as micro

and nanotechnology. One of the particular applications of nanotechnology is the subject so-called nanoelectromechanical system (NEMS). This area has been attracting a considerable amount of research interest from the scientific communities. One of the notable milestones in nanotechnology development is the invention of Carbon Nanotube. Carbon nanotubes (CNTs) have attracted an enormous wave of research interest since its discovery back in the earlier 90s [2]. These tiny structures represent the most promising contenders in various nano-based applications in numerous fields such as: physical, biological and electromechanical devices, etc. This is mainly due to their favorable mechanical and electrical properties.

A wide-ranging of research has been conducted to characterize the mechanical properties of CNTs, it mostly concluded that CNTs are showing remarkable results such as a high tensile strength, a low mass density, high length-to-radius ratio, and relatively thermally robust. The aforementioned properties have led CNTs to be widely used in the various type of nanoelectromechanical systems (NEMS) such as nanoresonators, nanoactuators, and nanosensors [3-8]. The interest of developing fully functioning CNT-based NEMS have been growing expeditiously since the last two decades in the academic and industrial scale [9-11]. Given that, a huge wave of research interest has been conducted, aiming the fully understanding of CNT behaviors.

In order to design a NEMS device principally utilizing CNTs as the main and effective structures, understanding their structural behaviors including the natural and resonant frequency and dynamic response are becoming indispensable. These challenges are mostly tackled by conducting an experimental analysis which is costly, demands a lot of complex apparatus requirements, and mainly challenging due to further technological

difficulties [11]. To overcome those constraints, people then think to use modeling approach as a promising alternative. Molecular dynamics (MD) was then developed by computational scientist to tackle these difficulties, and used by many researchers in this field [12-20]. In fact, MD is the most successful tool to model accurately the CNT behaviors, but there are some limitations in term of computational capabilities and effectiveness, i.e. limited atom numbers, very short time step, and extremely time-consuming computation [11, 21]. To be able to possibly overcome this limitation, researchers have been competing, in the past few decades, to improve analytical/numerical modeling tools base on the continuum mechanics, capable of predicting the structural behaviors of the CNT-based nanostructure.

Classical continuum theory has been used by many engineers working in this nano-scale field, since the originating work of Yakobson et al. [22]. They are touted as the first group who proposed an equivalent of the structural mechanics simplified model of CNTs and shells continuum elasticity to study their structural behaviors [11, 23-28]. They have concluded that these approaches are simple and computationally efficient. Moreover, when analyzing nanoscale structures, size-dependent effects were recently described as significant factors in the nanoscale continuum modeling of nano based structures [29-34]. Knowing that the classical continuum theory is not able to capture the size scale dependent effect, a non-classical modeling approaches are somehow needed. Eringen's nonlocal elasticity theory and the strain gradient theory (SGT) are the most used approach to model the size-dependent effects [11, 35-37]. In the latter approach, and instead of using one length scale dependent parameter which is taken into account in the Eringen's nonlocal theory, the SGT uses three size scale dependent parameters to be able

to capture the 3-D size dependent effects. It is worth noting that considering 3-D size dependent effects are somehow more powerful and offering flexibility to the NEMS design engineer. Commonly, most of the aforementioned investigations of the size dependent effects have raised the following similar conclusions: (1) The static behaviors of size dependent model were showing significant discrepancy compared to the classical theory, and (2) The natural frequencies of the micro/nano beams are somehow size-dependent, where, in many cases, the classical continuum underestimates the fundamental frequencies. Nevertheless, and since most of the previously published works deal numerically the nonlinear excitation forces by using either a fitting approach or series approximating functions, the nonlinear strain gradient-based structural behavior of single-walled carbon nanotubes (SWCNTs) under the nonlinear term of electrostatic force has not been studied thoroughly.

In addition to the size dependent effects, CNT-based nanodevices may experience high-temperature changes during their manufacturing and operation, leading to thermal deformation (i.e. shrinkage or expansion) and therefore residual stress affecting consequently their overall behaviors and reliability. Several works have been published regarding the estimation of the coefficient of thermal expansion (CTE), useful as critical parameter to investigate the thermal gradient effect on the CNT-based nanostructures. Later, many investigations of the thermal properties and thermal effects of CNTs based nano-devices have been conducted, and the majority have shown that any temperature changes could greatly influence the mechanical and electrical behaviors of these devices [19, 38-44]. Their results showed a significant effect of temperature in the variation of resonance frequencies of the CNT based nano-resonators.

To the best of the authors knowledge, and after a thorough survey of the literature, it is concluded that a very limited number of investigations considered the nonlinear structural problem of CNT based nanobeam, using the strain gradient elasticity theory, in which the nonlinearity due to the geometry (mainly due to the von Karman nonlinear strains of the CNT as well as the slack effect), the nonlinear actuating force exact term and thermal gradient effect are taken into consideration. To fill this gap in the literature, the present study aims to develop a non-classical CNT-beam model incorporating a modified strain gradient theory that accounts for the strain deformations gradients to capture the size effects of a CNT nanobeam with nonlinearities due to von Karman nonlinear strains, electrostatic forcing and thermal gradient effect.

1.2 Literature Review

In this section, we summarize several applications of CNT-based nanosystem in order to overview the remarkable and promising future in the world of nanotechnology. We then review the main contributions of employing non-classical elasticity theories in the modeling of nanostructure as well as its significant effects to their structural behaviors. We also cite several publications addressing the imperative of thermal gradient effect.

1.2.1 Nanoresonators

Nano-resonators are nano-devices or nano-systems vibrating at a so-called resonant frequency in order to exhibit the so-called resonance. These systems are also well known as oscillators. Thanks to their tiny (in the nano-scale) sizes, these nanostructures, which are mainly utilized as nanoresonators, possess high natural/resonant frequencies, and hence offer an important range for sensitivity to their *environment*. This high sensitivity

is favorable for sensing applications in the nano-scale. In this regards, a research group from Cornell University introduced a tunable CNT-based oscillator [3]. They reported a doubly clamped CNT under electrical actuation could be tuned. Moreover, they showed the possibility of using this kind of structure to measure very small amount of forces in the nano-scale. Truax et al. [45] proposed a mechanism of the so-called co-integrated micro-actuators to axially tune the fundamental frequencies of single-walled carbon nanotube (SWCNT) based resonators. They claimed that this method is capable to increase the resonant quality factor and removing residual slack. Li et al. [46] fabricated nano-cantilever with very high frequency in the application of fast scanning probe microscope (SPM). Hüttel et al. [47] investigated the mechanical resonance of a doubly clamped CNT suspended over platinum electrodes with a 800 *nm* trench. They reported that their structure can resonate at around 120 to 360 MHz with a high quality factor Q around 10^5 . In addition, they stressed on the importance of the nonlinear structural behaviors of the nano-structure mainly in coupling both the actuation (forcing) frequencies and the operating temperature.

In the structural dynamics field, it is known that the vibrational behaviors of mechanical structure are highly affected by their mechanical damping. Eichler et al. [48] deeply explored the nonlinear damping of both the CNT-based and graphene-based resonator. Their method represented an important breakthrough in improving the understanding of the nonlinearity of the damping represented as $\eta x^2 dx/dt$, where η is the nonlinear damping coefficient. They also demonstrated that the quality factor significantly depend upon the variation of the driving force applied to the structure. Recently, the research conducted by Island et al. [49] successfully developed high

frequency SWCNT-based NEMS clamped-clamped beam with a quality factor up to 10^6 . They tuned the structure frequency by altering the effective length of the structure and tension from the electrodes. They reported extremely high fundamental frequencies up to ≈ 280 GHz. In an another similar effort to improve the quality factor and higher fundamental frequencies, Moser et al. [8] claimed that their CNT-based resonator measured the highest possible to resonant frequency f in micro/nano resonators of around $Q \cdot f \approx 300$ THz, with a comparable quality factor Q with the previously mentioned published work [49] , i.e. $Q \approx 4.5 \times 10^6$. Therefore, these results are offering very promising CNT-based NEMS devices to be used as candidate in ultra-sensitive mass and force detections and other quantum mechanics applications.

1.2.2 Nanosensors

Nanosensors are getting a considerable attention from the scientific communities in the last decade. These tiny structures are promising in numerous applications such as ultrasensitive mass and force sensors, quantum macromechanical experiments, medical applications (in mass detection of viruses and bacteria), drugs deliveries, and biological applications [4, 6, 7, 50-55]. To mention few, Chiu et al. [4] used the shifting concept of resonance frequency of some CNT-based structures to detect and estimates the inertial mass of atoms. They adapted the method proposed by Sazonova et al. [3] to tune the frequencies. An alternating DC and AC voltages were applied between the source and drain electrodes. The resonance was achieved by tuning the forcing AC voltage frequency near the fundamental frequency of the CNT based nanobeam. The vibrations will modulate the gate capacitance and then one can measure the variations of the

capacitor induced currents which correlates with the carbon nanotube structural vibration amplitudes.

Noting the smart sensing idea in the nano-scale, we can state that if one assumed a very small mass in the neighborhood of the CNT based nano-structure, the resonant frequency will be shifted, and the vibration amplitudes decrease slightly. This scenario is effective to measure mass in the atomic level. The group led by Adrian Bachtold from The Institute of Photonic Science, in Barcelona, Spain, was reported an outstanding ultrasensitive mass sensor resolution with a yoctogram (10^{-24} g) mass sensitivity [6]. This latter group published their research on CNT-based ultrasensitive force detection with the sensitivity of $12 \times 10^{-21} \text{ N} / \text{Hz}^{1/2}$. This remarkable design is probably tribute as the most advance of their kind. The same group also reported a design of ultrasensitive force detection system based on the CNT-nanoresonator. They used a known capacitive force to assess the force sensitivity. They set the enclosed system at 1.2 K operating temperature and successfully reported 12 zeptoNewton $\text{Hz}^{-1/2}$ force-sensor sensitivity. They claimed that this achievement may open the possibility of individual nuclear spins detection.

1.2.3 Nanoactuators

Along with the rapid development of the nano and molecular electronics, scientists and engineers were driven to explore the possibility to use CNTs as actuators. An article published in *Science* and conducted by Rueckes et al. [5] designed a nanodevice employing suspended SWCNT with cross bar array configuration as nanoswitch. This work were tremendously relevant for many scientists mainly working in this area to exploit the use of CNT based nano-structures as nonvolatile random access memory for

molecular computing. In fact, the bistable behavior nature of the system, primarily due to the crossed and curved CNTs geometry, was useful to perform the switching (ON and OFF) action under the application of electrostatic actuations. Fennimore et al. [56] successfully built and operated a nano-motor incorporating a rotatable plate with the MWCNT used as bearing. This nano-motor can be precisely controlled by changing the actuating electric voltages. A group from Nagoya University published a work on nanorobotics manipulations [57]. Kuznetsov et al. [58] demonstrated the possibility of using CNT as nano-actuators by presenting some numerical analysis approving the principle of operation of this kind of nano-devices. Unfortunately, the development and use of CNT-based nano-actuators is somehow limited in the literatures compared with the nano-resonators and nano-sensors.

1.2.4 Size-dependent effects on the CNT-based nanobeam modeling

Size-dependent effects were recently described as significant factors in the nanoscale continuum modeling of nano based structures [29-34]. In fact, many groups investigated experimentally the size dependent effects in the micro/nano scales. To cite a few: Namazu et al. [29] reported that a silicon beam with the order of hundred nanometers in thickness is almost 4 times stiffer than larger dimension of silicon beam. By experimental investigation, Fleck [30] reported that the torsional rigidity of a copper rod with 12 μm diameter was almost three times larger than the copper rod with the diameter of 170 μm . The similar conclusions were also reported by other groups stressing the size-dependent effect on the small structures [31-34]. Hence this effect should be appropriately investigated.

Several elastic continuum models that incorporate the effect of size scale dependent effect have been proposed in the literature to predict the structural behaviors of nanobeams. These include Eringen's nonlocal elasticity theory [26, 33, 35, 36, 59-74], Mindlin's couple stress theory [75], modified couple stress theory [31, 37, 76-80], and strain gradient theory (SGT) [32, 73, 77-79, 81-88]. Contrast with the classical elasticity theory, Eringen's nonlocal theory assumes that the stress at a point is not only a function of the strain at the corresponding point but also is a function of the strains on the other points. This theory takes into account the inter-atomic long-range force. Several published works based on this theory are available in the literature. To mention a few: Peddieson et al. [33] introduced the applicability of nonlocal elastic beam theory to nanotechnology applications. Sudak [59] developed a complex model governing the column buckling of double-walled CNT (DWCNT) behaviors using nonlocal continuum theory. The van der Waals force was also considered in the model along with length scale dependent parameter. He demonstrated that the size effect dependencies should not be ignored in the analysis of DWCNT. Following the work of Sudak, Zhang et al. studied free transverse vibration analysis of DWCNT. They calculated analytically the natural frequencies of the DWCNT and the effects of size scale dependent parameter on the amplitude and frequencies of free vibration scenarios. They concluded that the classical theory might overestimate the natural frequencies prediction in the low magnitude regime, reciprocally, the classical one could underestimate the results in the higher frequency.

The SWCNT and DWCNT were incorporated in the framework of nonlocal elastic beam by Wang and Varadan [61]. They studied the effects of length and diameter scale on the dimensionless natural frequencies of the CNT. Their conclusions were similar to the

aforementioned works. Reddy [62] reformulated the available beam theories including Euler-Bernoulli, Timoshenko, Reddy and Levinson using the Eringen's nonlocal theories. He used Hamilton's principle to obtain the equation of motion via variational mathematics. The analytical solutions for bending, buckling and free vibration were presented briefly. Reddy and Pang [66] studied in deep the nonlocal elastic Timoshenko beam theory applied in several boundary conditions, including simply supported, clamped-clamped, cantilever and propped cantilever. Further, the size dependent effects to the deflections, buckling load, and natural frequencies were investigated in the normal and transverse shear stress components. Recently, Ansari et. el. [72] proposed the variational differential quadrature method to study the thermal loading in the vibrational characteristic of SWCNT employing nonlocal shell model in the framework. In the implementation of the nonlocal elastic beam theory, the magnitude of the size scale parameter is the key issue in order to obtain astonishing results compared to either molecular dynamics or experiments. The nonlocal parameter is related to the atomic structure and their lattice dynamics. While the classical parameters such as Young's moduli and shear elastic moduli are unable to represent the phonons dispersion of CNT, the energy dispersion phonons analysis will be useful to estimate nonlocal parameter represented the interatomic interactions within the CNT structure. Several works regarding the size scale parameter estimation are available in the literatures [36, 63, 67, 74]

On the other hand, the strain gradient theory considers the higher-order strain gradient of the microstructure but does not consider the inter-atomic long-range force. Instead of using one length scale dependent parameter, the SGT uses three size scale

dependent parameters to be able to capture the 3-D size dependent effects. The strain gradient theory (SGT) was formerly known as the higher-order elasticity theory developed earlier by Mindlin back in 1960s [89, 90]. The most important argument in this theory is that the strain energy density [79] depends on the classical strain (first-order deformation gradient) as well as the higher order deformation gradients. A modified strain gradient theory was proposed by Lam et al. [32], which mainly incorporates three size scale dependent parameters by considering higher order strain gradients.

There are several works [77-79, 83] employing the modified SGT to predict the structural behaviors of the micro and nanobeam such as buckling, bending, free vibrations, and forced vibrations. To name few: Wang et al. [77] studied the deflection, rotation, and natural frequencies of microbeam assuming SGT in the framework of the Timoshenko beam theory. Kahrobaiyan et al. [78] developed a nonlinear size-dependent Euler-Bernoulli beam model incorporating the beam geometric nonlinearity arising principally from the mid-plane stretching effects. They solved the free-vibration problem of hinged-hinged microbeam using a perturbation technique. Akgöz and Civalek [79] studied the size scale dependent and Poisson's effects on the static behaviors of SGT-based microbeam. They also explored the effect of various boundary conditions on the size scale base microbeam. The sequential work of Fakhrabadi et al. [86, 91] studied the effects of size dependent parameters in the static behaviors of doubly clamped and cantilever CNT-based nanobeam under parallel electrostatic load. They reported a significant discrepancies of the static analysis results between SGT and classical theory. By fitting the highly nonlinear electrostatic force term, Miandoab et al. [92, 93] solved both static, free vibration and dynamic problems of nanobeam. In addition, the

bifurcation diagram and resonant frequencies plot of the bi-stable resonator was compared between SGT and classical theory. As a particular case of the SGT, the modified couple stress theory is a specific case of strain gradient theory by assuming l_0 and l_1 which are the first and second size scale dependent parameters are zero, respectively [31, 75-80]. It is mostly been used due to their simplicity, and the classical boundary conditions are still valid to be used without any miscalculation doubt.

1.2.5 Temperature gradient effect

In addition to the size dependent effects, CNT-based nanodevices may experience high-temperature changes during their manufacturing and operation, leading to thermal deformation (i.e. shrinkage or expansion) and therefore residual stress affecting consequently their overall behaviors and reliability. Several works have been published in this regards: Jiang et al. [94] developed an analytical method to calculate the coefficient of thermal expansion (CTE) for CNTs, and reported that these values are negative at low and room temperature and then become positive at high temperature. Later, many investigations of the thermal properties and thermal effects of CNTs based nano-devices have been conducted, and the majority have shown that any temperature changes could greatly influence the mechanical and electrical behaviors of these devices [19, 38-43]. The axial and radial thermal expansion of SWCNTs was investigated using molecular structural mechanics by Li and Chou [38]. Zang et al. [39] and Alamus et al. [19] reported CNT softening behavior proliferation with any assumed temperature increase. Kang et al. [44] studied the temperature dependent effect on the mass detection sensitivity of CNT based nano-resonators. They used simple sinusoidal force as an actuation method. They solved the problem by converting the continuous equation of

motion to a Duffing-like single-degree of freedom oscillator equation without accounting for the electrostatic actuating term. Their results showed a significant effect of temperature in the variation of resonance frequencies of the CNT based nano-resonators.

1.3 Thesis Objective and Organization

The objectives of this thesis are:

1. To derive the equation of motion of the doubly clamped CNT-based nanobeam incorporating both size scale dependent parameters and temperature gradient effects in the framework of strain gradient Euler-Bernoulli beam theory.
2. To prescribe the non-classical mode-shape function by considering linearized eigenvalue problem.
3. To perform the static analysis of doubly clamped CNT-based nanobeam under parallel plate electrostatic actuation load and investigate the effect of size scale dependent parameters as well as the temperature gradient effects.
4. To solve the linearized eigenvalue problem of doubly clamped CNT-based nanobeam and predict the natural frequency of the nanobeam while varying the size scale dependent parameters, electrostatic load, and temperature gradients.
5. To perform the dynamic analysis of doubly clamped CNT-based nanobeam under parallel plate electrostatic actuation load and investigate the effect of size scale dependent parameters.
6. To perform parametric study for the above mentioned cases for various nanobeam parameters.

This thesis is organized as follows. Following this introduction, a brief and useful background is presented. The classical continuum, the strain gradient elasticity theory and the thermal gradient effects are briefly reviewed in Chapter 2. In Chapter 3, a nonlinear beam model employing a modified strain gradient theory is presented, where the von Karman nonlinear strain deformations (mid-plane stretching), initial curvature (slack), temperature gradient effect, and electrostatic forcing nonlinearities are all taken into consideration. Then, in order to get the non-classical expression of mode shapes assuming the non-classical beam model, an eigenvalue problem is first constructed and then solved numerically using singular value decomposition method, to obtain the eigenvalues and eigenfunctions while varying the size scale parameters. In the same chapter, a Galerkin based reduced-order discretization technique to convert the nonlinear partial differential equation into ordinary differential equations is presented. In Chapter 4, numerical results related to the static deflections analysis of the CNT-based nanobeam with nonlinear mid-plane stretching when subjected to a static DC voltage and temperature gradients are presented. In Chapter 5, an eigenvalue problem analysis is carried out to investigate the natural frequency dispersion of the straight and slacked CNT. Further, the investigation of modes veering and modes crossing possibilities are carried out in the presence of higher-order strain gradient deformation and temperature gradients effects. The effects of the size scale dependent parameters to the dynamics behavior of the CNT-based nanobeam in very low actuation load regime are presented in Chapter 6. Finally, Chapter 7 will conclude the thesis and outlines few recommendations as future research.

CHAPTER 2

BACKGROUND

In this chapter we introduce general concepts in modeling the nonlinear structural mechanics of CNT-based nanobeams. The commonly assumed classical continuum theory is reviewed, following with the non-classical continuum modeling incorporating the size scale dependent parameters effects. A brief review of simple one dimensional (1D) thermal stress modeling is also presented in the last section of this chapter.

2.1. The Classical Continuum Model of Beam

The general expression of the CNT-based Euler-Bernoulli nanobeam model for either straight or slacked configuration (with initial curvature) are available in the literatures [23-25, 42, 95]. The model was developed based on classical continuum theory. The most common procedure of deriving the classical beam equation of motion can be outlines as follows:

1. Define the elastic strain model while assuming the von Karman-type nonlinear strain-displacement relation given as follows:

$$\varepsilon_{11} = \frac{\partial u(x,t)}{\partial x} + \frac{1}{2} \left(\frac{\partial w(x,t)}{\partial x} \right)^2 - z \frac{\partial^2 w(x,t)}{\partial x^2}, \quad (2.1)$$

where $u(x,t)$ and $w(x,t)$ are the axial and transverse displacements of a point on the neutral axis. Simply, the strain energy density U , kinetic energy T , and non-conservative work of the considered system W_{non} are given by,

$$U = \frac{1}{2} \int_V \sigma \varepsilon dV = \frac{EA}{2} \int_0^L \left(\frac{\partial u(x,t)}{\partial x} + \frac{1}{2} \left(\frac{\partial w(x,t)}{\partial x} \right)^2 \right)^2 dx + \frac{EI}{2} \int_0^L \left(\frac{\partial w(x,t)}{\partial x} \right)^2 dx, \quad (2.2)$$

$$T = \frac{\rho A}{2} \int_0^L \left(\left(\frac{\partial u(x,t)}{\partial t} \right)^2 + \left(\frac{\partial w(x,t)}{\partial t} \right)^2 \right) dx, \quad (2.3)$$

$$W_{non} = \int_0^L F(t)w(x,t)dx, \quad (2.4)$$

where E is Young's modulus, A is cross section area, ρ is mass density, σ is Cauchy stress tensor, ε is strain tensor, L is length of the beam, and the external force $F(t)$ is given as the external force per unit length.

2. Then, obtain the variational form of the above energy expressions, and integrate the expressions assuming an initial time t_1 and a final time t_2 .
3. Employ the Hamilton's principle to get the equation of motion and its respective boundary conditions, which call be written as follows [23, 95]:

$$EI \frac{\partial^4 w}{\partial x^4} + \rho A \frac{\partial^2 w}{\partial x^2} = \left(\frac{EA}{2L} \int_0^L \left(\frac{\partial w}{\partial x} \right)^2 \right) \frac{\partial^2 w}{\partial x^2} + F(x,t), \quad (2.5)$$

$$w(0,t) = 0; w(L,t) = 0; \frac{\partial w(0,t)}{\partial x} = 0; \frac{\partial w(L,t)}{\partial x} = 0; \quad (2.6)$$

Another form of the above equation (2.5) while including the damping dissipating terms as well as the slack effect is given by [24, 25, 96]

$$EI \frac{\partial^4 w}{\partial x^4} + \rho A \frac{\partial^2 w}{\partial t^2} + c \frac{\partial w}{\partial t} = \frac{EA}{2L} \left(\int_0^L \left(\frac{\partial w}{\partial x} \right)^2 - 2 \frac{\partial w}{\partial x} \frac{dw_0}{dx} \right) \left[\frac{\partial^2 w}{\partial x^2} - \frac{d^2 w_0}{dx^2} \right] + F(x, t), \quad (2.7)$$

where the initial slack function and the damping coefficient are denoted by $w_0(x)$ and c , respectively. The slack function is commonly modeled as the first Euler-buckling instability function $w_0 = b_0 \sin(\pi x / L)$, where b_0 represents the beam mid-point elevation [24, 25, 88, 96].

For convenience and in order to avoid numerical errors when manipulating small dimensional quantities in this nano-scale, the following nondimensional parameters were assumed to construct a normalized version of the equation of motion [23-25, 59, 61, 88, 95]:

$$\hat{w} = \frac{w}{d}; \quad \hat{b}_0 = \frac{b_0}{d}; \quad \hat{w}_0 = \frac{w_0}{d}; \quad \hat{x} = \frac{x}{L}; \quad \hat{t} = \frac{t}{T_{classic}}; \quad \hat{r} = \frac{r}{d}; \quad (2.8)$$

We substitute the above expression of Eq. (2.8) into Eq. (2.7), the nondimensional equation of motion is given as,

$$\frac{\partial^4 \hat{w}}{\partial \hat{x}^4} + \frac{\partial^2 \hat{w}}{\partial \hat{t}^2} + c \frac{\partial \hat{w}}{\partial \hat{t}} = \alpha_1 \left(\int_0^1 \left(\frac{\partial \hat{w}}{\partial \hat{x}} \right)^2 - 2 \frac{\partial \hat{w}}{\partial \hat{x}} \frac{d\hat{w}_0}{d\hat{x}} \right) \left[\frac{\partial^2 \hat{w}}{\partial \hat{x}^2} - \frac{d^2 \hat{w}_0}{d\hat{x}^2} \right] + \alpha_2 F(\hat{x}, \hat{t}), \quad (2.9)$$

$$\alpha_1 = \frac{Ad^2}{2I}; \quad \alpha_2 = \frac{\pi \varepsilon_0 L^4}{EI d^2}; \quad T_{classic} = \sqrt{\frac{\rho AL^4}{EI}}; \quad c = \frac{\hat{c} L^4}{EIT_{classic}}.$$

We note here that all the above defined normalized variables in Eq. (2.8) are dimensionless. The above described classical models can be used to predict the static,

linearized fundamental frequency, and the dynamic behaviors of any geometrical dimensions. These models are reported to be unable of capturing the size scale dependencies which are imperative in the micro/nano-scale structure, as reported by many researchers (detailed literature review available in Chapter 1). Moreover, the above classical model does still lack of temperature dependencies because of the absence of coefficient of thermal expansion, which is known to become significant, when the beam is being excited by a thermal gradient load. Therefore, an improved model incorporating the above conditions is still needed.

2.2. A short review of strain gradient elasticity theory

In the classical Cauchy stress theory, the strain energy only depends on the stress and strain tensor [31, 32]. Whereas, in the framework of a strain gradient theory [32], one should consider the higher strain terms involving a dilatation gradient term which represents a vector quantity, denoted by γ_p , a deviatoric stretch gradient which is a third order tensor, denoted by η^1_{pqr} , and a gradient of rotation tensor denoted as χ_{pq} . Hence, the total strain energy within a considered domain volume \forall can be written as [32]:

$$U = \frac{1}{2} \int_{\forall} (\sigma_{pq} \epsilon_{pq} + \mathbf{p}_p \gamma_p + \tau^1_{pqr} \eta^1_{pqr} + \mathbf{m}_{pq} \chi_{pq}) dv \quad (2.10)$$

where σ_{pq} represents the Cauchy stress tensor, and \mathbf{p}_p , τ^1_{pqr} and \mathbf{m}_{pq} are the higher-order stress tensors corresponding to the higher-order tensor terms. The remaining parameters in Eq. (2.10) are summarized below [32, 81]:

$$\epsilon_{pq} = \frac{1}{2} (u_{p,q} + u_{q,p}), \quad (2.11)$$

$$\gamma_i = \varepsilon_{mm,i}, \quad (2.12)$$

$$\begin{aligned} \eta_{pqr}^1 = & \frac{1}{3}(\varepsilon_{qr,p} + \varepsilon_{rp,q} + \varepsilon_{pq,r}) - \frac{1}{15} \delta_{pq} (\varepsilon_{ss,r} + 2\varepsilon_{sr,s}) + \\ & - \frac{1}{15} [\delta_{qr} (\varepsilon_{ss,p} + 2\varepsilon_{sp,s}) + \delta_{rp} (\varepsilon_{ss,q} + 2\varepsilon_{sq,q})], \end{aligned} \quad (2.13)$$

$$\chi_{pq} = \frac{1}{2}(\theta_{p,q} + \theta_{q,p}), \quad (2.14)$$

$$\theta_p = \frac{1}{2}(\text{curl}(u))_p, \quad (2.15)$$

$$\sigma_{pq} = \lambda[\varepsilon]^T \delta_{pq} + 2G\varepsilon_{pq}, \quad (2.16)$$

$$p_p = 2Gl_0^2 \gamma_p, \quad (2.17)$$

$$\tau_{pqr}^1 = 2Gl_1^2 \eta_{pqr}^1, \quad (2.18)$$

$$m_{pq} = 2Gl_2^2 \chi_{pq}, \quad (2.19)$$

where u_p is the CNT axial displacement, θ_p is the rotation vector, γ_p is the dilatation gradient vector, δ_{pq} is the Kronecker's delta operator, λ and G are the Lamé constants, respectively. The size scale dependent parameters noted above as l_0 , l_1 , and l_2 are the dilatation, the deviatoric stretch, and the rotation gradients, respectively.

The above described strain energy density had been used by Kong et al. [81] to develop the equation of motion governing the static behaviors of the microbeam. They derived the model of micro cantilever beam problem. They developed the model in the framework of Bernoulli-Euler beam. They used simple concentrated force, and then formulated the analytical procedure to solve static bending problem. They concluded with the significant deviations of those obtained by strain gradient theory, couple stress theory

(as simple as taking l_0 and l_1 are zero), and the classical theory. The results of static analysis are represented in Figure 2.1.

The results of Figure 2.1 show the significance of the size scale effects on several beam case studies and with various beam thickness and length. Figures 2.1a-d show that that the bending rigidity of the small beam increases with the decrease of the beam thickness. The deviations with the classical continuum model are almost diminishing when the thickness of the beam is approaching the size scale dependent parameters. These results are qualitatively in agreement with the experimental study of Lam et al. [32] who proposed the modified strain gradient theory.

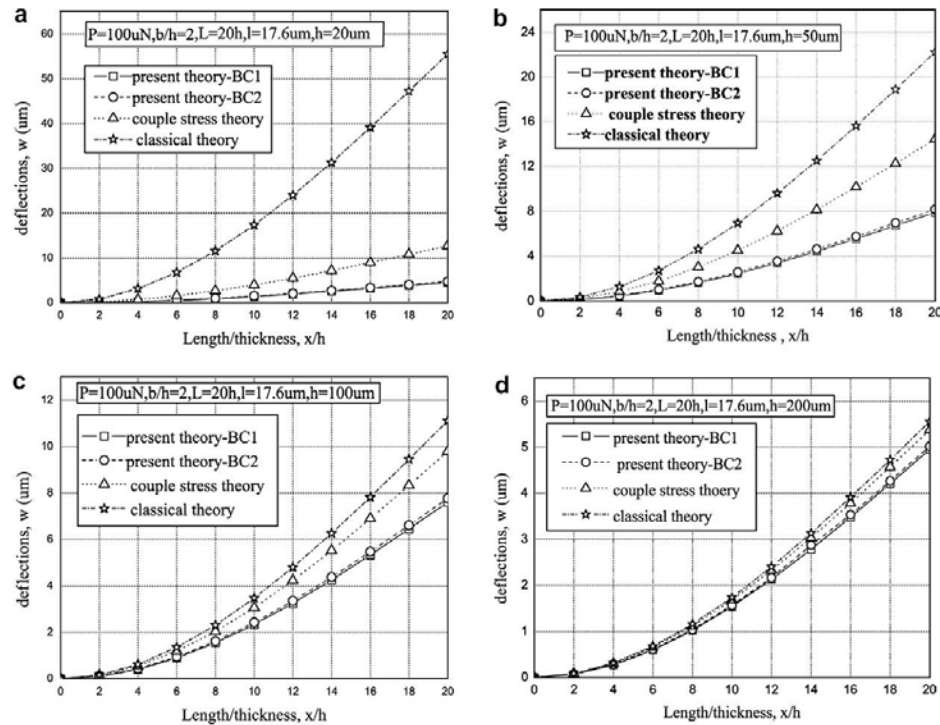


Figure 2.1: Comparison of the static deflection of cantilever microbeams based on classical continuum, couple stress, and strain gradient theories and for various beam thickness h : (a) $h = 20\mu\text{m}$; (b) $h = 50\mu\text{m}$; (c) $h = 100\mu\text{m}$; (d) $h = 200\mu\text{m}$ [81].

2.3. Thermal Gradient Effects

Another effect which had been reported to be imperative in the CNT-based nanobeam modeling is the temperature gradient effect. Ansari et al. [42] studied CNT-based nanobeam with several boundary conditions. They incorporated the thermal effect embedded in the classical beam theory, then solved the equation using variational iteration method (VIM). The thermal effect term was assumed as $N_T = \frac{EA}{1-2\nu}\alpha T$, where N_T is axial load due to thermal gradient, ν is Poisson's ratio, α is coefficient of thermal expansion, T is temperature. They concluded that the beam is experiencing stiffening behavior, leading to an increase of the effective natural frequency when operated at lower temperature gradient conditions. Contrary, the beam experiences softening behavior tending to decrease its effective natural frequency when operated at higher temperature gradients. The limitation of the work of Ansari et al. [42] was the absence of the electrostatic actuating load mostly used in numerous applications of CNT-based devices. Another work was reported in this same topic by Kang et al. [44] while using the finite element method. They solved the nonlinear classical beam equation with thermal effect subjected by simple harmonic load. They concluded on the resonance frequencies drop of CNT-based nanobeam in higher temperature environments. Their study is useful in providing an insight on the thermal effect on nano-structures when subjected to harmonic excitations.

CHAPTER 3

PROBLEM DEFINITION, MODELING AND SOLUTION METHODOLOGY

In this chapter, the derivations of equation of the CNT-based nanobeam are presented briefly incorporating the size scale dependent effect. The proposed model would also incorporate the von-Karman nonlinearity for mid-plane stretching effect, the nonlinear electrostatic force exact term and the temperature gradient effects. The CNT-based nanobeam is modeled in the framework of an Euler-Bernoulli beam assuming both ends clamping boundary condition. We used the Hamilton's principle to derive the equation of motion of the doubly clamped CNT-based nanobeam while considering the non-classical strain energy expression using a modified strain gradient theory proposed by Lam et al. [32].

3.1. Equation of Motion of Doubly Clamped Slacked CNT-based Nanobeam

Figure 3.1 shows a schematic of a parallel-plates electrically actuated CNT. The CNT-based nanobeam is modeled in the framework of an Euler-Bernoulli beam assuming doubly-clamped boundary condition, with a radius r , a shell thickness h , an effective length L , a mass density ρ , a Young's modulus E , a cross-sectional area A , and a cross-sectional moment of inertia I . It is worth mentioning first, that few previous studies have

reported the imperfect (slack) geometry of nanostructure made of clamped-clamped CNTs [3, 97-100]. They all concluded that due to their fabrication process using the so-called chemical vapor deposition (CVD) technique, fabricating perfectly straight CNTs with controlled geometry and orientation is somehow difficult. They also established that the level of slack can significantly affect the structural/dynamical behavior of these nanostructures. Therefore, the below investigated CNT based nanobeam will be assumed initially curved with some slack levels.

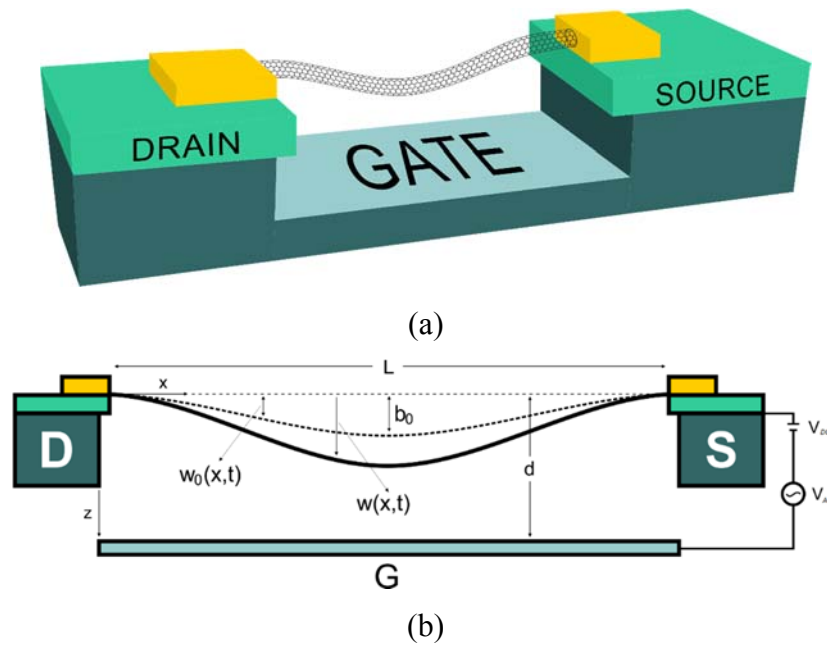


Figure 3.1: Schematic of a doubly clamped CNT based nanobeam assuming parallel-plates electrostatic actuation.

3.1.1. Non-classical strain energy density derivation

In order to obtain the equation of motion of the problem in Figure 3.1, we will use the so-called Hamilton's principle to derive the governing equation of motion of the CNT while considering the non-classical strain energy expression as was previously presented in [32]. Strain energy density expression incorporating the size scale dependent

parameters is presented in this subsection. By assuming an Euler-Bernoulli beam model, the carbon nanotube displacement field can be expressed as:

$$u_1 = u(x, t) - z \left\{ \frac{\partial w(x, t)}{\partial x} - \frac{dw_0(x)}{dx} \right\}; u_2 = 0; u_3 = w(x, t) - w_0(x), \quad (3.1)$$

By considering the von-Karman nonlinearity of the clamped-clamped CNT for mid-plane stretching effect, the first order nonlinear strain-displacement relations for an initially curved beam can be written as follows [62, 87, 101]:

$$\varepsilon_{11} = \frac{\partial u}{\partial x} + \frac{1}{2} \left(\frac{\partial w(x, t)}{\partial x} \right)^2 - \frac{1}{2} \left(\frac{dw_0(x)}{dx} \right)^2 - z \left(\frac{\partial^2 w(x, t)}{\partial x^2} - \frac{d^2 w_0(x)}{dx^2} \right), \quad (3.2)$$

where $w_0(x)$, $u(x, t)$, and $w(x, t)$ represent the initial slack profile function in the x - z plane, the axial displacement along the x -axis and the transverse displacements along the- z axis, all measured from the initial slack profile, respectively.

Next, we evaluate the higher strain terms as function of the beam displacement components, we are left with the following expressions [32]:

$$\gamma_1 = \frac{\partial \varepsilon_{11}}{\partial x} = \frac{\partial^2 u}{\partial x^2} + \frac{\partial w}{\partial x} \frac{\partial^2 w}{\partial x^2} - \frac{dw_0}{dx} \frac{d^2 w_0}{dx^2} - z \left(\frac{\partial^3 w}{\partial x^3} - \frac{d^3 w_0}{dx^3} \right), \quad (3.3)$$

$$\gamma_3 = \frac{\partial \varepsilon_{11}}{\partial z} = - \left(\frac{\partial^2 w}{\partial x^2} - \frac{d^2 w_0}{dx^2} \right), \quad (3.4)$$

$$\chi_{12} = \chi_{21} = \frac{1}{2} \left\{ \frac{\partial}{\partial y} \left(\frac{1}{2} \frac{\partial u_3}{\partial y} - \frac{1}{2} \frac{\partial u_2}{\partial z} \right) + \frac{\partial}{\partial x} \left(\frac{1}{2} \frac{\partial u_3}{\partial x} - \frac{1}{2} \frac{\partial u_1}{\partial z} \right) \right\} = - \left(\frac{\partial^2 w}{\partial x^2} - \frac{d^2 w_0}{dx^2} \right), \quad (3.5)$$

where γ_1 and γ_3 are non-zero components of dilatation gradient terms. χ_{12} and χ_{21} are non-zero components of gradient of rotation tensors. Expanding the indices of Eq. (2.13)

and Eqs. (2.17)-(2.19), while imposing a non-zero components of deviatoric stretch gradient tensor, $\boldsymbol{\eta}_{pqr}^1$, we obtain the following non-zero terms [32]:

$$\eta_{111}^1 = \frac{2}{5} \left(\frac{\partial^2 u}{\partial x^2} + \frac{\partial w}{\partial x} \frac{\partial^2 w}{\partial x^2} - \frac{dw_0}{dx} \frac{d^2 w_0}{dx^2} - z \left(\frac{\partial^3 w}{\partial x^3} - \frac{d^3 w_0}{dx^3} \right) \right), \quad (3.6)$$

$$\eta_{113}^1 = \eta_{311}^1 = \eta_{131}^1 = -\frac{4}{15} \left(\frac{\partial^2 w}{\partial x^2} - \frac{d^2 w_0}{dx^2} \right), \quad (3.7)$$

$$\eta_{122}^1 = \eta_{133}^1 = \eta_{212}^1 = \eta_{221}^1 = \eta_{313}^1 = \eta_{331}^1 = -\frac{1}{5} \left(\frac{\partial^2 u}{\partial x^2} + \frac{\partial w}{\partial x} \frac{\partial^2 w}{\partial x^2} - \frac{dw_0}{dx} \frac{d^2 w_0}{dx^2} - z \left(\frac{\partial^3 w}{\partial x^3} - \frac{d^3 w_0}{dx^3} \right) \right), \quad (3.8)$$

$$\eta_{223}^1 = \eta_{232}^1 = \eta_{332}^1 = \frac{1}{15} \left(\frac{\partial^2 w}{\partial x^2} - \frac{d^2 w_0}{dx^2} \right); \quad \eta_{333}^1 = \frac{1}{5} \left(\frac{\partial^2 w}{\partial x^2} - \frac{d^2 w_0}{dx^2} \right), \quad (3.9)$$

Next, we obtain the non-zero components of higher-order stress tensor, \mathbf{p}_p , $\boldsymbol{\tau}_{pqr}^1$ and \mathbf{m}_{pq} ,

$$p_1 = 2l_0^2 G \gamma_1; \quad p_3 = 2l_0^2 G \gamma_3, \quad (3.10)$$

$$m_{12} = m_{21} = 2Gl_2^2 \chi_{12} = 2Gl_2^2 \chi_{21}, \quad (3.11)$$

$$\tau_{111}^1 = 2Gl_1^2 \eta_{111}^1, \quad (3.12)$$

$$\tau_{113}^1 = \tau_{131}^1 = \tau_{311}^1 = -\frac{8}{15} Gl_1^2 \left(\frac{\partial^2 w}{\partial x^2} - \frac{d^2 w_0}{dx^2} \right), \quad (3.13)$$

$$\begin{aligned} \tau_{122}^1 &= \tau_{133}^1 = \tau_{212}^1 = \tau_{221}^1 = \\ &= \tau_{313}^1 = \tau_{331}^1 = -\frac{2}{5} Gl_1^2 \left(\frac{\partial^2 u}{\partial x^2} + \frac{\partial w}{\partial x} \frac{\partial^2 w}{\partial x^2} - \frac{dw_0}{dx} \frac{d^2 w_0}{dx^2} - z \left(\frac{\partial^3 w}{\partial x^3} - \frac{d^3 w_0}{dx^3} \right) \right), \end{aligned} \quad (3.14)$$

$$\tau_{223}^1 = \tau_{232}^1 = \tau_{322}^1 = -\frac{2}{15} Gl_1^2 \left(\frac{\partial^2 w}{\partial x^2} - \frac{d^2 w_0}{dx^2} \right), \quad (3.15)$$

$$\tau_{333}^1 = 2Gl_1^2 \eta_{333}^1, \quad (3.16)$$

Then, substituting Eqs. (3.3-3.16) into the strain energy density function, Eq. (2.10), yields the following variational of the potential energy due to the classical and nonlocal strain gradient terms:

$$\delta U = P \int_0^L \Gamma_0 \delta \Gamma_0 dx + Q \int_0^L \Gamma_1 \delta \Gamma_1 dx + EA \int_0^L \Gamma_2 \delta \Gamma_2 dx + R \int_0^L \Gamma_3 \delta \Gamma_3 dx, \quad (3.17)$$

where the operators Γ_0 , Γ_1 , Γ_2 , and Γ_3 , are defined as follows:

$$\Gamma_0 = \frac{\partial^2 w}{\partial x^2} - \frac{d^2 w_0}{dx^2}; \quad \Gamma_1 = \frac{\partial^3 w}{\partial x^3} - \frac{d^3 w_0}{dx^3}, \quad (3.18)$$

$$\Gamma_2 = \frac{\partial u}{\partial x} + \frac{1}{2} \left(\frac{\partial w}{\partial x} \right)^2 - \frac{1}{2} \left(\frac{dw_0}{dx} \right)^2; \quad \Gamma_3 = \frac{\partial^2 u}{\partial x^2} + \frac{\partial w}{\partial x} \frac{\partial^2 w}{\partial x^2} - \frac{dw_0}{dx} \frac{d^2 w_0}{dx^2},$$

and where the constants P , Q , and R , are defined with the following explicit expressions

$$P = \left(EI_y + GA \left(2l_0^2 + \frac{8}{15} l_1^2 + l_2^2 \right) \right), \quad Q = GI_y \left(2l_0^2 + \frac{4}{5} l_1^2 \right), \quad R = GA \left(2l_0^2 + \frac{4}{5} l_1^2 \right), \quad (3.19)$$

The size scale dependent parameters, l_0 , l_1 , and l_2 are the dilatation, the deviatoric stretch, and the rotation gradients, respectively [32].

Subsequently, and in order to include the effect of nonlinear geometric mid-plane stretching, we consider the following axial strain energy function due to residual axial stress denoted as U_A , and defined as follows:

$$U_A = \int_0^L \left\{ \sigma_A \int_A \varepsilon_{11} dA \right\} dx = \int_0^L \frac{N_0}{A} \left(\int_A \varepsilon_{11} dA \right) dx = \int_0^L N_0 \left(\frac{\partial u}{\partial x} + \frac{1}{2} \left(\frac{\partial w}{\partial x} \right)^2 - \frac{1}{2} \left(\frac{dw_0}{dx} \right)^2 \right) dx, \quad (3.20)$$

where N_0/A represents the residual axial stress, mainly assumed to be uniformly distributed over the cross-sectional area of the beam. The above expression, as will be

embedded in the equation of motion, would account for both linear part (normal force), and the nonlinear part (mid-term stretching effect) of the residual stress force. Next, using Eq. (3.20), we can approximate the variational of the axial strain energy as follows:

$$\delta U_A = \int_0^L N_0 \left(\frac{\partial(\delta u)}{\partial x} + \frac{\partial w}{\partial x} \frac{\partial(\delta w)}{\partial x} \right) dx = N_0 \delta u + N_0 \frac{\partial w}{\partial x} \delta w \Big|_0^L - N_0 \int_0^L \frac{\partial^2 w}{\partial x^2} \delta w dx, \quad (3.21)$$

3.1.2. The kinetic energy and work of non-conservative forces

The variational of kinetic energy function δT can simply be defined as:

$$\begin{aligned} T &= \frac{1}{2} \rho A \int_0^L \left(\left(\frac{\partial u}{\partial t} \right)^2 + \left(\frac{\partial w}{\partial t} \right)^2 \right) dx, \\ \Rightarrow \delta T &= \rho A \int_0^L \left(\frac{\partial u}{\partial t} \frac{\partial}{\partial t} \delta(u) + \frac{\partial w}{\partial t} \frac{\partial}{\partial t} \delta(w) \right) dx, \\ \Rightarrow \int_{t_1}^{t_2} \delta T dt &= -\rho A \int_{t_1}^{t_2} \left(\int_0^L \frac{\partial^2 u}{\partial t^2} \delta(u) dx + \int_0^L \frac{\partial^2 w}{\partial t^2} \delta(w) dx \right) dt, \end{aligned} \quad (3.22)$$

The last component that will be included in Hamilton's principle is the work of non-conservative forces, denoted by δW , and can be expressed as:

$$\delta W = \int_0^L F_e(x, t) \delta w dx + \int_0^L F_{ax}(x, t) \delta u dx - C_s \int_0^L \frac{\partial^2 w}{\partial t \partial x} \delta w dx - C_v \int_0^L \frac{\partial w}{\partial t} \delta w dx, \quad (3.23)$$

where F_e and F_{ax} symbolizes the electrostatic and axial forces, respectively, and the quantities C_s , and C_v are the structural and the viscous damping coefficient terms, respectively.

3.1.3. Hamilton's principle

Finally, we can get the CNT-based nanobeam equation of motion by substituting Eqs. (3.17), (3.21), (3.22), and (3.23) into the following extended Hamilton's principle equation:

$$\int_{t_1}^{t_2} \delta L dt = \int_{t_1}^{t_2} (\delta T - \delta U - \delta U_A + \delta W) dt = 0, \quad (3.24)$$

Afterward, integrating by part, and then simplifying the mathematical expression by gathering the terms multiplying both arbitrary operators “ δu ” and “ δw ”, we can write the following two coupled equations of motion governing both the axial and the transverse displacement functions governing the motion of the CNT nanobeam neutral axis:

$$0 = \frac{\partial}{\partial x} \left\{ EA \left[\frac{\partial u}{\partial x} + \frac{1}{2} \left(\frac{\partial w}{\partial x} \right)^2 - \frac{1}{2} \left(\frac{dw_0}{dx} \right)^2 \right] \right\} - \frac{\partial}{\partial x} \left\{ R \frac{\partial^2}{\partial x^2} \left[\frac{\partial u}{\partial x} + \frac{1}{2} \left(\frac{\partial w}{\partial x} \right)^2 - \frac{1}{2} \left(\frac{dw_0}{dx} \right)^2 \right] \right\} + \quad (3.25)$$

$$+ F_{ax}(x, t) - \rho A \frac{\partial^2 u}{\partial t^2},$$

$$0 = P \left(\frac{\partial^4 w}{\partial x^4} - \frac{d^4 w_0}{dx^4} \right) - Q \left(\frac{\partial^6 w}{\partial x^6} - \frac{d^6 w_0}{dx^6} \right) - \frac{\partial}{\partial x} \left\{ \frac{\partial w}{\partial x} \left[N_0 + EA \left[\frac{\partial u}{\partial x} + \frac{1}{2} \left(\frac{\partial w}{\partial x} \right)^2 - \frac{1}{2} \left(\frac{dw_0}{dx} \right)^2 \right] \right] \right\} + \quad (3.26)$$

$$+ \frac{\partial}{\partial x} \left\{ \frac{\partial w}{\partial x} R \left[\frac{\partial^2}{\partial x^2} \left[\frac{\partial u}{\partial x} + \frac{1}{2} \left(\frac{\partial w}{\partial x} \right)^2 - \frac{1}{2} \left(\frac{dw_0}{dx} \right)^2 \right] \right] \right\} + \rho A \frac{\partial^2 w}{\partial t^2} + C_s \frac{\partial^2 w}{\partial t \partial x} + C_v \frac{\partial w}{\partial t} - F_e(x, t),$$

where the parameters P , Q , and R are defined in Eq. (3.19). Note here that as the longitudinal dynamics is low prominent for a flexible structure as compared to its transverse dynamics, the inertia term in Eq. (3.25) can be assumed small and therefore can be neglected. Also note that in the above Eqs. (3.25) and (3.26), the internal axial force due to a temperature gradient is considered through the axial force function F_{ax} . For

this, we consider the conventional thermal elasticity theory, where the thermal axial force can be written as follows $F_{ax} = EA\alpha_T\Delta T$, where α_T is the coefficient of thermal expansion (CTE) of the CNT, and ΔT is the temperature gradient.

After re-arranging Eq. (3.25) and substitute it into Eq. (3.26), one can write the following equation of motion governing only the transverse displacement of the CNT based nanobeam:

$$P\left(\frac{\partial^4 w}{\partial x^4} - \frac{d^4 w_0}{dx^4}\right) - Q\left(\frac{\partial^6 w}{\partial x^6} - \frac{d^6 w_0}{dx^6}\right) + \rho A \frac{\partial^2 w}{\partial t^2} + C_s \frac{\partial^2 w}{\partial t \partial x} + C_v \frac{\partial w}{\partial t} = \frac{\partial}{\partial x} \left(\frac{\partial w}{\partial x} \{N_0 + EA\alpha_T\Delta T\} \right) + F_e \quad (3.27)$$

Then, we compute the internal axial force by integrating the axial stress of a discretionary beam cross-section as follows:

$$N = N_0 + \int_A E \varepsilon_{11} dA = N_0 + \int_A E \left(\frac{\partial u}{\partial x} + \frac{1}{2} \left(\frac{\partial w(x,t)}{\partial x} \right)^2 - \frac{1}{2} \left(\frac{dw_0(x)}{dx} \right)^2 \right) dA \quad (3.28)$$

Assuming a uniformly distributed axial force induced by transverse deflection and zero external axial force ($N = 0$), the geometric nonlinearity due to the mid-plane stretching of the beam along the x -axis can be described by the average of its stretching axial force over the whole beam length and shown in the integral-differential term, hence Eq. (3.28) reduces to:

$$N_0 = -\frac{EA}{2L} \int_0^L \left[\left(\frac{\partial w}{\partial x} \right)^2 - \left(\frac{dw_0}{dx} \right)^2 \right] dx \quad (3.29)$$

Substituting Eq. (3.29) into Eq. (3.26), we get the subsequent equation of motion with its respective corresponding boundary conditions governing the transverse displacement of

the CNT based nanobeam, and while considering both the size dependent parameters as well as the thermal gradient effects:

$$\begin{aligned} & \rho A \frac{\partial^2 w}{\partial t^2} + C_s \frac{\partial^2 w}{\partial t \partial x} + C_v \frac{\partial w}{\partial t} - Q \left(\frac{\partial^6 w}{\partial x^6} - \frac{d^6 w_0}{dx^6} \right) + P \left(\frac{\partial^4 w}{\partial x^4} - \frac{d^4 w_0}{dx^4} \right) + \\ & + \left(EA \alpha_T \Delta T - \frac{EA}{2L} \int_0^L \left[\left(\frac{\partial w}{\partial x} \right)^2 - \left(\frac{dw_0}{dx} \right)^2 \right] dx \right) \frac{\partial^2 w}{\partial x^2} = F_e(x, t), \end{aligned} \quad (3.30)$$

$$w(0, t) = w(L, t) = 0, \quad \left. \frac{\partial w}{\partial x} \right|_{x=0} = \left. \frac{\partial w}{\partial x} \right|_{x=L} = 0, \quad \left. \frac{\partial^2 w}{\partial x^2} \right|_{x=0} = \left. \frac{\partial^2 w}{\partial x^2} \right|_{x=L} = 0, \quad (3.31)$$

Note that in Eq. (3.31), the first four boundary conditions are the classical one and the last two are quoted as the non-classical one both associated with the clamped-clamped nano-structure.

The electrostatic force function, $F_e(x, t)$, for a carbon nanotube under a parallel-plates electric field assumption can be written as [23-25, 95]:

$$F_e(x, t) = \frac{\pi \varepsilon_0 (V_{DC} + V_{AC} \cos(\Omega t))^2}{\sqrt{(d - w - w_0)(d - w - w_0 + 2r) \left(\cosh^{-1} \left(1 + (d - w - w_0)/r \right) \right)^2}}, \quad (3.32)$$

Where, ε_0 is air dielectric constant, V_{DC} is DC gate voltage, V_{AC} is AC gate voltage, Ω is AC harmonic frequency, and d is the gap width between bottom electrode and axis- x , as shown in Figure 3.1. For convenience and to get rid of any numerical computation problems that may arise when solving for the previous equations, we assume the following non-dimensional variables:

$$\hat{w} = \frac{w}{d}; \quad \hat{b}_0 = \frac{b_0}{d}; \quad \hat{w}_0 = \frac{w_0}{d}; \quad \hat{x} = \frac{x}{L}; \quad \hat{t} = \frac{t}{T}; \quad \hat{r} = \frac{r}{d}; \quad (3.33)$$

where time constant of $T = \sqrt{\frac{\rho AL^4}{P}}$. Next, by substituting Eq. (3.33) into Eqs. (3.30)-

(3.32), the normalized equation of motion can be written in normalized form as:

$$\beta_0 \hat{w}^{vi} + \hat{w}^{iv} + \ddot{\hat{w}} + \hat{C}_s \dot{\hat{w}}' + \hat{C}_v \dot{\hat{w}} = \left[-\beta_2 \alpha_T \Delta T + \beta_1 \left(\int_0^1 (\hat{w}')^2 dx - 2 \int_0^1 (\hat{w}' \hat{w}'_0)^2 dx \right) \right] (\hat{w}'' - \hat{w}''_0) + \beta_3 F_e(\hat{x}, \hat{t}), \quad (3.34)$$

where:

$$F_e = \frac{(V_{DC} + V_{AC} \cos(\hat{\Omega} \hat{t}))^2}{\sqrt{(1 - \hat{w} - \hat{w}_0)(1 - \hat{w} - \hat{w}_0 + 2\hat{r})} \left(\cos^{-1} \left(1 + \frac{1 - \hat{w} - \hat{w}_0}{\hat{r}} \right) \right)^2} \quad (3.35)$$

$$\beta_0 = -\frac{Q}{PL^2}; \quad \hat{C}_s = \frac{C_s L}{\sqrt{\rho AP}}; \quad \hat{C}_v = \frac{C_v L^2}{\sqrt{\rho AP}}; \quad \beta_1 = \frac{EA d^2}{2P}, \quad (3.36)$$

$$\beta_2 = \frac{EAL^2}{P}; \quad \beta_3 = \frac{\pi \epsilon_0 L^4}{Pd^2}; \quad \hat{\Omega} = \Omega \sqrt{(\rho AL^4)/P},$$

and the following corresponding normalized boundary conditions:

$$\hat{w}(0) = 0, \quad \hat{w}(1) = 0, \quad \frac{\partial \hat{w}(0)}{\partial \hat{x}} = 0, \quad \frac{\partial \hat{w}(1)}{\partial \hat{x}} = 0, \quad \frac{\partial^2 \hat{w}(0)}{\partial \hat{x}^2} = 0, \quad \frac{\partial^2 \hat{w}(1)}{\partial \hat{x}^2} = 0, \quad (3.37)$$

The detailed derivation can be referred in the Appendix of this thesis.

3.2. Galerkin's Modal Decomposition

In order to solve the above nonlinear equation of motion, Eq. (3.34), we propose the use of the Galerkin decomposition technique, useful to discretize the partial differential equation into finite number of coupled ordinary differential equations through a reduced-order modeling (ROM) process [102]. This approach along with its

applications to nonlinear analysis is available in the following textbook [103]. As a result, we assume that the transverse deflection of the slacked CNT-based nanobeam can be approximated as:

$$w(x, t) = \sum_{i=1}^n u_i(t) \phi_i(x), \quad (3.38)$$

where, $\phi_{1 \leq i \leq n}(x)$ represent trial functions, assumed here as the mode shape functions of the clamped-clamped nanobeam, and $u_{1 \leq i \leq n}(t)$ are their respective modal coordinates. The trial (admissible) functions for the clamped-clamped beam mode shapes are assumed to be orthonormal functions so that:

$$\int_0^1 \phi_i(x) \phi_j(x) dx = \delta_{ij} = \begin{cases} 1 & i = j \\ 0 & i \neq j \end{cases} \quad (3.39)$$

By substituting Eq. (3.38) into Eq. (3.34), multiplying by $\phi_{1 \leq j \leq n}(x)$, and then integrating the whole equation of motion from 0 to 1, we obtain set of ordinary differential equations (ODEs) in term of modal coordinates functions $u_{1 \leq i \leq n}(t)$. These ODEs can be solved numerically using suitable nonlinear coupled differential equations algorithms. The above constructed ROM will be used in the coming section to solve the eigenvalue problem in order to calculate the CNT natural frequencies and their corresponding eigenvectors, which represent the mode shapes, expressions as functions of the CNT non-classical parameters.

3.3. Non-classical Mode Shapes

In this sub-section, the non-classical mode shapes prescription is presented. It is worth mentioning here that, as we are dealing with some non-classical boundary conditions, Eq. (3.37), considering the classical mode-shapes expressions will no longer be valid to construct the ROM. Therefore, we need to develop a linearized eigenvalue analysis in this regards. The governing equation of a linear eigenvalue problem can be obtained by assuming the modal coordinates $u_i(t)$ as an exponential function in term of each modal natural frequency of the nanobeam, i.e.:

$$u_i(t) = e^{j\omega_i t}, \quad (3.40)$$

Substituting Eqs. (3.40) and (3.38) into Eq. (3.34),

$$\begin{aligned} 0 = & \beta_0 \sum_{i=1}^n e^{i\omega t} \phi^{vi} + \sum_{i=1}^n e^{i\omega t} \phi^{iv} - \omega^2 \sum_{i=1}^n e^{i\omega t} \phi_i + i\omega \sum_{i=1}^n C_s e^{i\omega t} \phi'_i + i\omega \sum_{i=1}^n C_v e^{i\omega t} \phi_i + \\ & - \left[-\beta_2 \alpha_T \Delta T + \beta_1 \left(\int_0^1 \left(\sum_{i=1}^n e^{i\omega t} \phi'_i \right)^2 d\hat{x} - 2 \int_0^1 \left(\sum_{i=1}^n e^{i\omega t} \phi'_i \hat{w}'_0 \right) d\hat{x} \right) \right] \left(\sum_{i=1}^n e^{i\omega t} \phi_i'' - \frac{d^2 \hat{w}_0}{d\hat{x}^2} \right) + \\ & -\beta_3 \frac{(V_{DC} + V_{AC} \cos(\Omega \hat{t}))}{\sqrt{\left(1 - \sum_{i=1}^n e^{i\omega t} \phi_i - \hat{w}_0 \right) \left(1 - \sum_{i=1}^n e^{i\omega t} \phi_i - \hat{w}_0 + 2\hat{r} \right)}} \left(\cosh^{-1} \left(1 + \frac{1 - \sum_{i=1}^n e^{i\omega t} \phi_i - \hat{w}_0}{\hat{r}} \right) \right)^2 \end{aligned} \quad (3.41)$$

Then, in order to get the linear eigenvalue problem governing equation, we substitute Eq. (3.40) into the ROM equations while neglecting the effect of all external and nonlinear forces (the electric force, the damping forces, the axial thermal effect force, and the mid-

plane stretching terms). Hence, we end up with the following the sixth-order ODE needed to obtain the expression of the non-classical mode shape functions:

$$\beta_0 \phi_i^{vi} + \phi_i^{iv} - \omega_i^2 \phi_i = 0, \quad (3.42)$$

where ω_i are i^{th} natural frequency of the beam. A general solution of Eq. (50) can be expressed as [104]

$$\phi_i(x) = C_1 e^{m_1 x} + C_2 e^{m_2 x} + C_3 e^{m_3 x} + C_4 e^{m_4 x} + C_5 e^{m_5 x} + C_6 e^{m_6 x}, \quad (3.43)$$

where m_i symbolize the roots of the characteristic equation of the eigenvalue problem governed by Eq. (3.42). The acquired roots will then be used to determine the constants of integrations C_i of the non-classical mode shape functions. We can obtain the characteristic equation of the Eq. (3.42),

$$f(m) = \beta_0 m^6 + m^4 - \omega^2 = 0, \quad (3.44)$$

We evaluate the real and imaginary parts of all the roots for small value of β_0 as depicted in both Figure 3.2 and Figure 3.3 respectively.

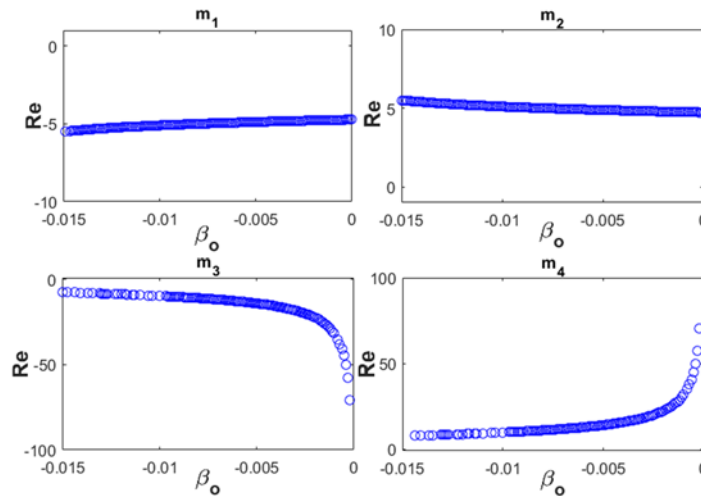


Figure 3.2: Variation of the first four real roots with small values of the tuning parameter β_0 .

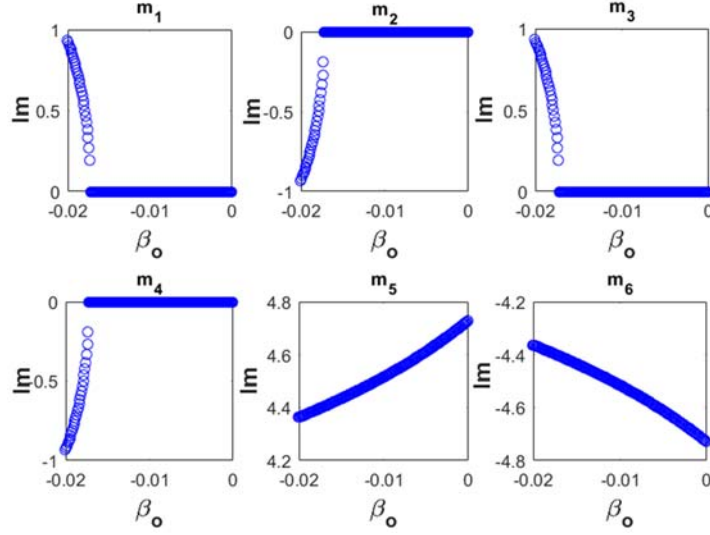


Figure 3.3: Variation of the first six imaginary roots with small values of the tuning parameter β_0 .

It should be noted from Figure 3.2 that the real part of both roots m_5 and m_6 are zero for any small value of β_0 . Moreover, along with dispersion roots plot in the Figure 3.3, one can be added that the imaginary part of first four roots are all zero, and the remaining two roots are complex conjugates. Therefore, one can conclude that the roots characteristic equation can be written considering small values of β_0 as follows:

$$m_{1,2} = \pm\lambda_1, \quad m_{3,4} = \pm\lambda_2, \quad m_{5,6} = \pm j\lambda_3, \quad (3.45)$$

Next, we substitute Eq. (3.45) into the characteristic equation Eq. (3.44), then straightforwardly function of λ_i in term of ω_i or $i = 1, 2, 3$ can be obtained. It can be noted here that the general solution of Eq. (3.44) is also function of ω_i , where i represents the i^{th} mode shape.

From Eq. (3.45) and (3.43), the mode shape function can written as:

$$\phi(x) = C_1 \cosh(\lambda_1 x) + C_2 \sinh(\lambda_1 x) + C_3 \cos(\lambda_3 x) + C_4 \sinh(\lambda_3 x) + C_5 \frac{e^{-\lambda_2 x}}{\lambda_2^2} + C_6 \frac{e^{-\lambda_3 x - \lambda_2}}{\lambda_2^2} \quad (3.46)$$

Since the mode shape function should satisfy the boundary conditions, next we substitute Eq. (3.46) into Eq. (3.37), the matrix eigenvalue problem can be written as:

$$[\mathbf{A}(\beta_0, \lambda_1, \lambda_2, \lambda_3)][C_1, C_2, C_3, C_4, C_5, C_6]^T = 0, \quad (3.47)$$

$$|\mathbf{A}(\beta_0, \omega_i)| = 0, \quad (3.48)$$

One notes here that matrix \mathbf{A} in Eq. (3.48) is a 6x6 matrix appears as a function of ω_i . Not to get trivial solutions, the constants coefficients of matrix \mathbf{C} should not be zero, hence, $\mathbf{C} = [C_1, C_2, C_3, C_4, C_5, C_6]^T \neq 0$. Consequently, we have to make sure that the determinant of matrix \mathbf{A} is identically zero, thus solving for the unknown coefficients λ_i and lastly get the remaining parameters necessary to generate the non-classical mode shape functions, which are satisfying all of the classical and non-classical boundary conditions. The obtained mode shape functions will be used with Eq. (3.38), to solve the equation of motion, Eq. (3.30), either statics or dynamics. Toward this, these methods will be used to investigate the statics and dynamics of the doubly-clamped CNT-based nanobeam.

CHAPTER 4

STATIC ANALYSIS

In this chapter, the size scale dependent parameters effects on the CNT mode shapes are first studied. Then, the higher-order strain gradient parameters effects on the static deflections of the doubly-clamped CNT based nanobeam are carried out. The results of static analysis is then compared with those obtained when assuming classical elasticity theory. The Galerkin's modal decomposition technique which has been described in Chapter 3 is applied in this static analysis. The chapter also outlines the temperature gradient effects on the CNT-based nanobeam when assuming high CNT length-to-radius ratio.

4.1. The Size Scale Dependent Parameter Effects on the CNT Mode Shape

4.1.1. The size scale dependent effects on the mode shape parameters

As previously described in Chapter 3, it is clearly stated that by considering very small β_0 , we can easily solve Eq. (3.48). The solutions of ω_i are depicted in Figure 4.1, which is representing the first linear frequency. In this figure, one compares the current results with those obtained by Miandoab et al. [93]. The results are showing significant deviations due to the different adopted boundary conditions as will be explained subsequently. Figure 4.1 shows that the strain gradient theory is sensitive to the boundary conditions indicated by the significant deviations of first natural frequency of the

considered nanobeam. Based on the previously described derivation of the equation of motion (see Appendix for the details regarding the equation of motion derivations), it was found that the first derivative (the slope) and the second derivative (the moment) of the beam in-plane transverse deflection are set equal to zero. In is worth mentioning here that in previous attempt to solve such equations, a research group [93] assumed the first derivative (the slope) and third derivative (the shear) should all be equal to zero, respectively. It is important to note that, in the modified strain gradient theory, the bending moment not only depends on the second derivative of the transverse deflection but also depends on the fourth derivative of the transverse deflection [32]. This is consistent with few other published works [81, 84, 101, 105], in which the moment equation is written as:

$$M = P \frac{\partial^2 w}{\partial x^2} - Q \frac{\partial^4 w}{\partial x^4}, \quad (4.1)$$

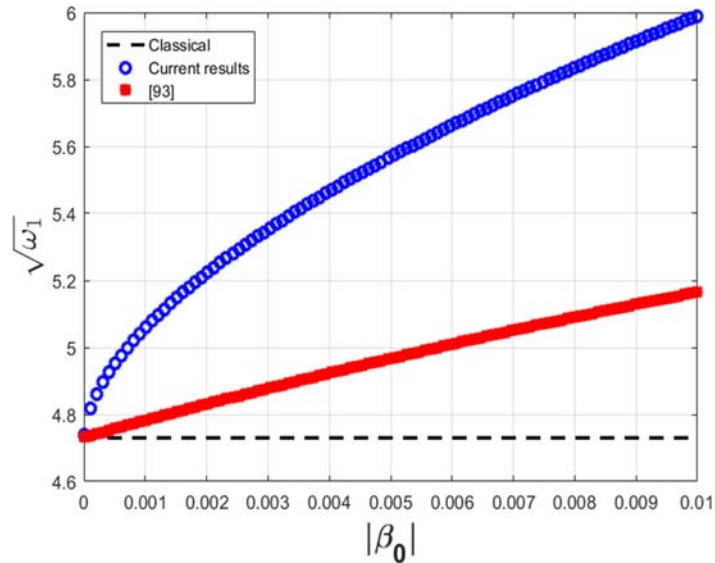


Figure 4.1: Comparison of the variation of the square root of the first frequency when assuming classical and non-classical beam equation as well as two set of non-classical boundary conditions.

From Figure 4.1, through analyzing the parameters effect mainly defined here as β_0 as given in Eq. (3.36), we can clearly see that, as we decrease the CNT dimensions (the radius), the estimations of the fundamental natural frequency using non-classical beam model are drastically deviating from the classical continuum beam theory.

Next, we investigate the strain gradient effects on the roots of the characteristic equation, Eq. (3.45) which are important parameters of the mode shape function. The results are shown in the Figure 4.2(a), Figure 4.2(b), and Figure 4.2(c). The figures are clearly showing significant result deviations between the one considering the boundary conditions in Eq. (4.1) and the boundary conditions as assumed in [93] specifically for λ_1 and λ_3 which are the first and third roots, respectively. The second root results are almost negligible, as depicted in Figure 4.2(b). It is again showing that the boundary conditions assumption is critical in the application of strain gradient theory in the case of doubly-clamped beam. However, the previously stated conclusion is still can be adopted here about the deviations will increase toward the decrease of beam dimension.

4.1.2. The non-classical mode shape

We consider several CNT-based nanobeam dimensions as a numerical example to see the size dependent effects on the mode shape. One compares up to four mode shape functions to be investigated. The CNT-beam geometrical parameters are listed in the Table 4.1.

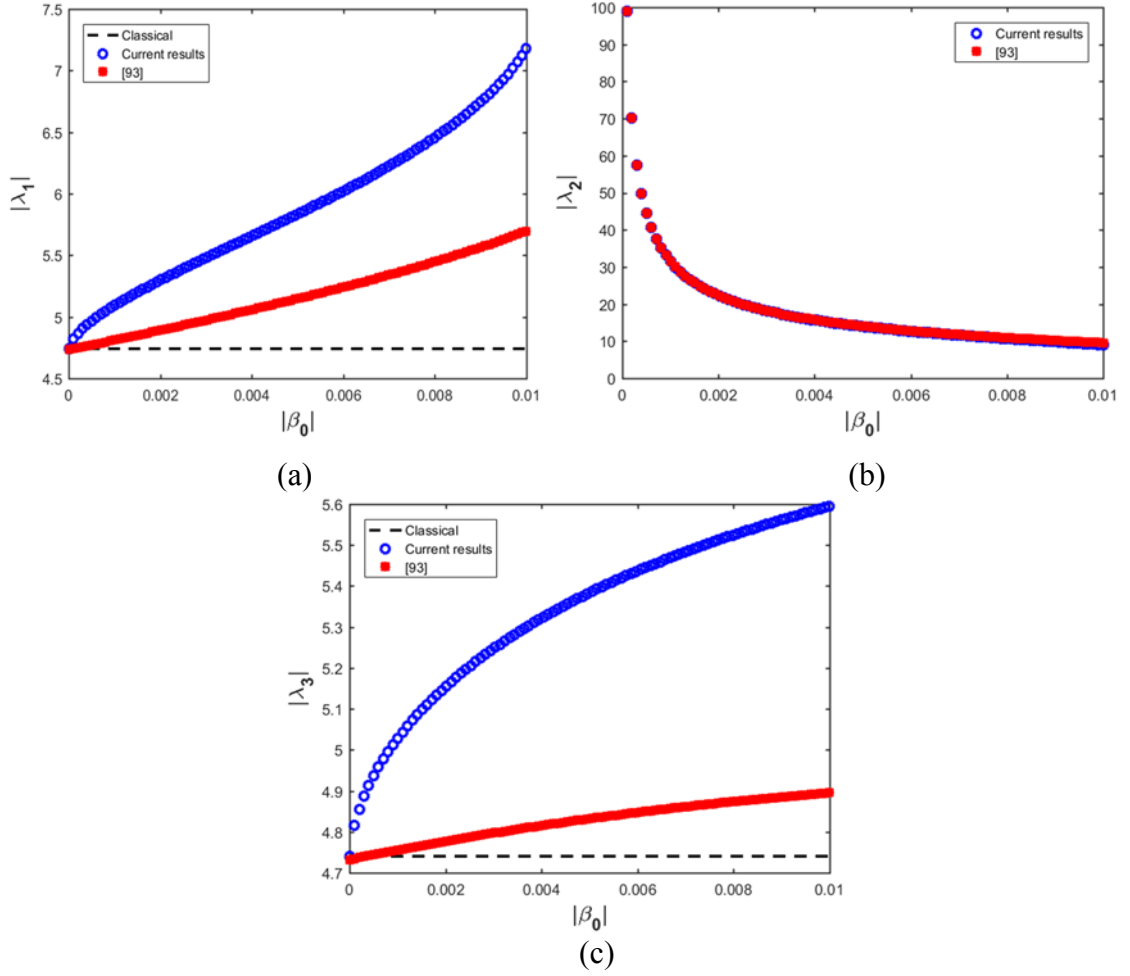


Figure 4.2: Variation of the absolute value of the first, second, and third characteristic roots of the eigenvalue problem when assuming classical and non-classical beam equation as well as two set of non-classical boundary conditions.

Table 4.1: The assumed CNT geometrical properties used to simulate the results of Figure 4.3

d	L	r	l
(nm)	(nm)	(nm)	(nm)
100	2000	0.65	5.0

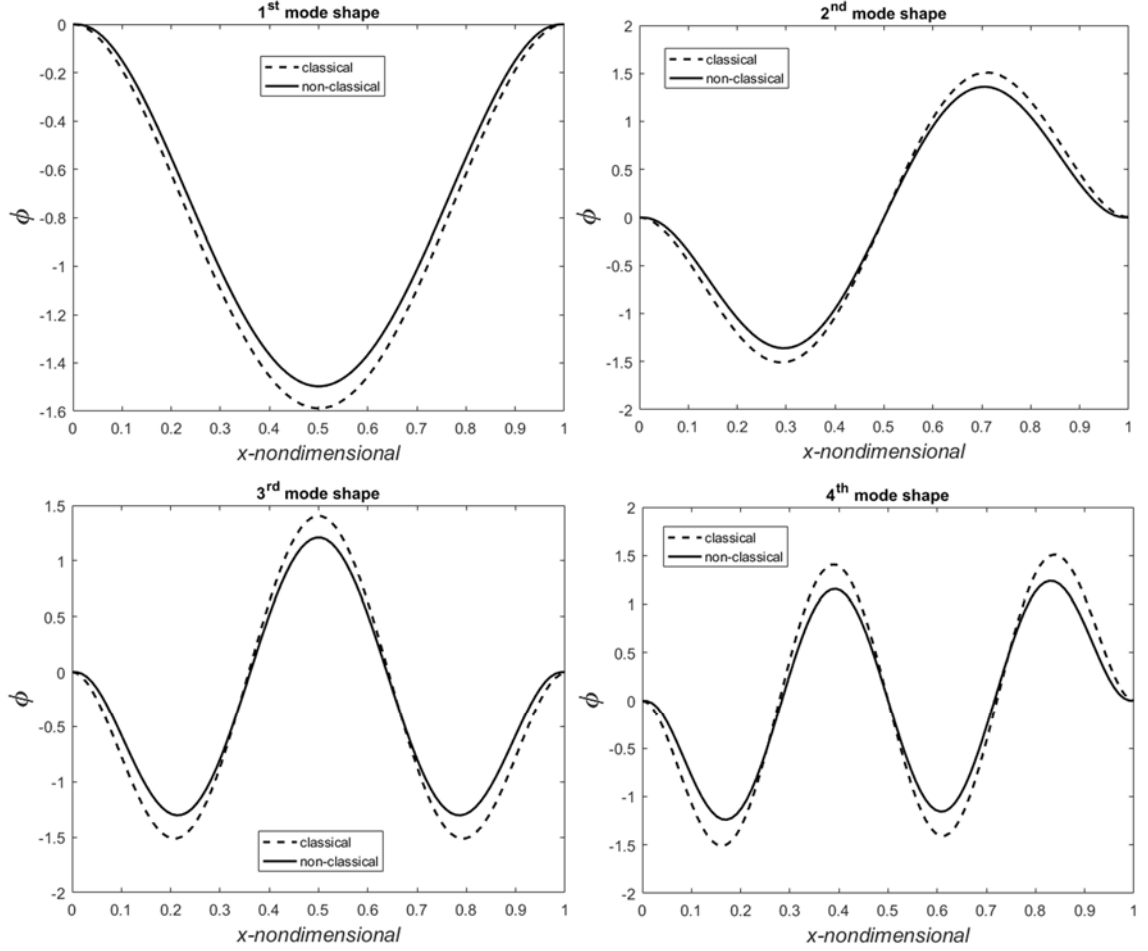


Figure 4.3: Comparison between the CNT classical and non-classical mode shapes assuming the geometrical properties of Table 4.1.

It is visibly shown that taking into account the size scale dependent parameters in the equation will significantly affect the mode shape functions. Despite the statement in [70] that the classical mode shape function are still valid to be used in the strain gradient model, it depends on how much the accuracy is specified by the NEMS designer.

4.2. Size Scale Dependent Parameter Effects

In order to get the static solution of the CNT based nano-beam, the time dependent terms are neglected in Eq. (3.38), and the admissible solution of the differential equation can be written as:

$$\hat{w}(\hat{x}) = \sum_{i=1}^n a_i \phi_i(\hat{x}), \quad (4.2)$$

where $\phi_{1 \leq i \leq n}(x)$ are the normalized non-classical mode shapes of each considered beam, and $a_{1 \leq i \leq n}$ are time-independent constant coefficients. Substituting the above approximated solution, Eq. (4.2), into the equation of motion while satisfying the orthogonality conditions of the eigenvector when multiplying the outcome equation with each mode-shapes function $\phi_{1 \leq i \leq n}(x)$, then integrating numerically from 0 to 1, we get with the following ROM governing the static behavior of the CNT based nanobeam:

$$\begin{aligned} & \sum_{i=1}^n \beta_0 a_i \int_0^1 \phi_i^{VI}(\hat{x}) \phi_j(\hat{x}) d\hat{x} + \sum_{i=1}^n a_i \int_0^1 \phi_i^{IV}(\hat{x}) \phi_j(\hat{x}) d\hat{x} - \beta_3 \int_0^1 F_e(\hat{x}) \phi_j d\hat{x} + \\ & + \int_0^1 \left\{ \left[\beta_2 \alpha_T \Delta T - \beta_1 \left(\int_0^1 \left(\sum_{i=1}^n a_i \phi_i'(\hat{x}) \right)^2 d\hat{x} - 2 \int_0^1 \left(\sum_{i=1}^n a_i \phi_i'(\hat{x}) \hat{w}_0' \right) d\hat{x} \right) \right] \left(\sum_{i=0}^n a_i \phi_i''(\hat{x}) - \hat{w}_0'' \right) \phi_j(\hat{x}) \right\} d\hat{x} = 0, \end{aligned} \quad (4.3)$$

$j = 1, 2, 3, \dots$

Finally, through solving the above coupled non-linear algebraic equation as function of the constant parameters a_i , one can approximate the static responses of any assumed CNT nanobeam case study.

As Eq. (4.3) cannot be solved analytically due to the complicated nonlinear functions embedded in all almost all the integral terms, we propose to implement a numerical approach in which the above-coupled nonlinear algebraic equations would be considered as an unconstrained minimization problem; subsequently one can solve them using a modified trust-region algorithm. The basic idea behind this numerical algorithm is iterating on the value of k so that the nonlinear function $f(x, \eta)$ is minimized around

zero, where x , assumed to be the control variable in this process, is the non-dimensional position of the beam. Formerly, one approximate the function f with an estimate function $\xi(k)$ which should mimic the same behavior of the function f in the neighborhood of a trust region denoted by S , and around an initial guess point denoted by η . A set of loops should be properly designed to ensure that the value of the function f is minimum over the trust region S , which can be described by the following sub-problem:

$$\min_s \{ \xi(k), k \in S \}, \quad (4.4)$$

The loop is repeated until the objective point of $\eta+k$, would satisfy the following condition: $f(\eta+k) < f(\eta)$. Finally, the acquired objective point will be embedded in the ROM nonlinear-coupled equations to get a full expression of the beam deflection profile. One develops the MATLAB codes to solve this coupled equations. Several parameters were studied to investigate the static transversal deflection of the CNT-based nanobeam with the present of higher order strain gradient effects.

4.2.1. Numerical example and convergences

In the below simulations, the CNT nanobeam is assumed as a cylinder beam with length of $L=3000 \text{ nm}$, Young's modulus $E=1.0 \text{ TPa}$ and a mass density $\rho =1.35 \text{ g/cm}^3$. Various case studies of are considered. Table 4.2 summarizes these cases with their respective geometrical properties. We first examine the convergence of the constructed reduced-order model. Therefore, the solutions of classical theory are verified using the previously published work [23] to ensure the numerical solution convergences.

Table 4.2: Geometrical properties of the case studies of CNTs considered in this work.

Case	d (nm)	r (nm)	Ref.
1	100	30	[23, 95, 106]
2	100	20	[23, 95, 106]
3	100	10	Current work
4	100	1	Current work
5	300	1	Current work
6	300	3	Current work
7	300	5	Current work
8	500	1	[24, 95]

By easily dropping the strain gradient term, the model is become very much equivalent with the classical model. We then calculate the maximum static deflection of both classical model and non-classical model from cases 1, 2, 3, and 4, and first four symmetric/odd modes, ensuring the convergences results. Figure 4.4 and Figure 4.5 show the convergence results of classical model and non-classical model for case 1 of Table 4.2, respectively. Figure 4.4 shows that considering five modes are quietly acceptable convergences. Also the figure reveals that asymmetric modes are not significant in the static deflection results. We can clearly observe from the mode shape curve that the middle point of asymmetric modes (even modes) are almost zero. For the case of doubly-clamped beam which the maximum deflections mostly located in the $L/2$ of the beam, hence, ignoring the even modes are somehow still valid without any significant errors. We did the same checking approach for strain gradient model as shown in the Figure 4.5, accordingly.

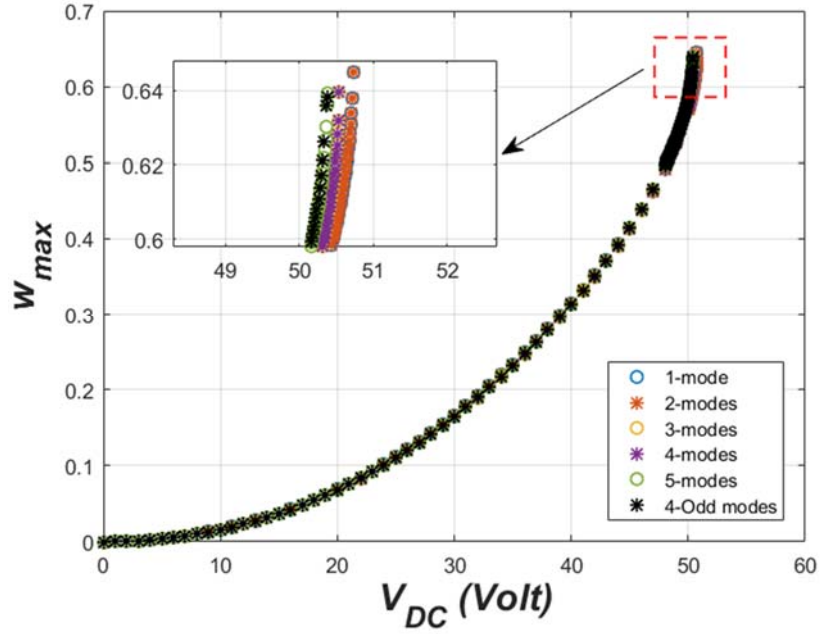


Figure 4.4: Variation of the normalized maximum static deflection of the CNT with the DC voltage for case 1 of Table 4.2, when assuming classical continuum theory, and for various number of modes in the ROM.

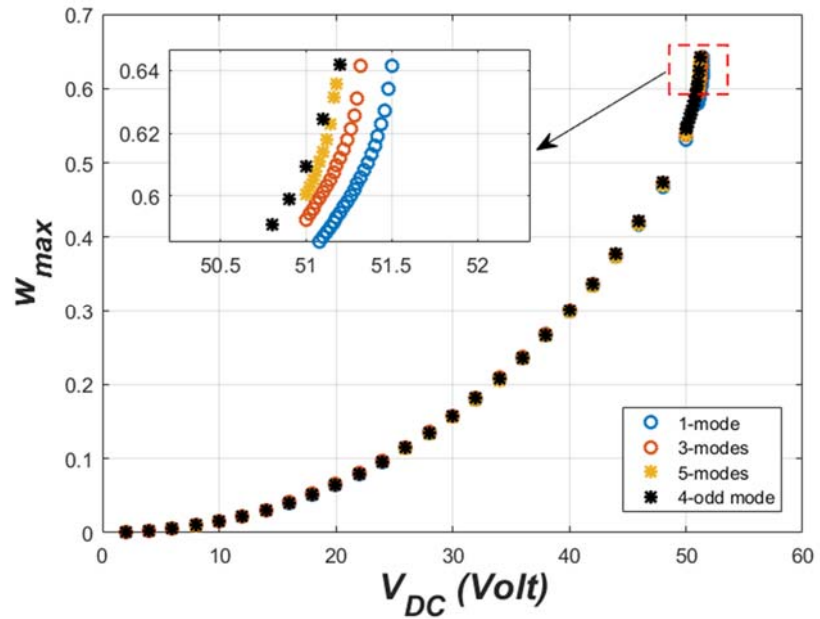


Figure 4.5: Variation of the normalized maximum static deflection of the CNT with the DC voltage for case 1 of Table 4.2, when assuming non-classical continuum (strain gradient) theory, and for various number of modes in the ROM.

4.2.2. Size scale dependent effects on the maximum static deflection

Next, we calculate the maximum static deflection of the beam parameters available in the Table 4.2 while varying the size scale dependent parameters. Figure 4.6 shows the normalized maximum deflection of doubly-clamped CNT for the cases 1, 2 and 3 of Table 4.2, while assuming all length scales parameters to be equal, i.e: $l_0 = l_1 = l_2 = l$ [32, 81, 83]. In the same figure, we consider several values of l while comparing the outcomes with the classical continuum theory (CCT), for several electrostatic DC gate voltages. As presented in the Figure 4.6, we can clearly discern the discrepancy between the static response curves assuming the classical continuum theory and the one of the strain-gradient theory. It is observed that, for a certain fixed DC gate voltage, the SGT theory static solutions are smaller as compared to the classical static solution. This discrepancy is becoming larger for higher size scale parameters.

It is also interesting to note that the SGT, which is taking into consideration the higher order strain gradients as compared to the CCT, is somehow stiffening the CNT nanobeam. As consequence, we can clearly observe that the pull-in voltages of the doubly clamped CNT beam are increasing with the SGT testifying that the classical continuum theory is underestimating the pull-in instability values for small-scale beam. Also note that zooming around the pull-in instability region in Figure 4.6, one can notice that the strain gradient effect is more prominent, but this effect reduces as we consider CNT with smaller length-to-radius ratio (L/r). In contrary, far from the pull-in instability, the same figure shows that the strain gradient has more significant effect in the low actuation load regime for CNT with larger length-to-radius ratio (L/r).

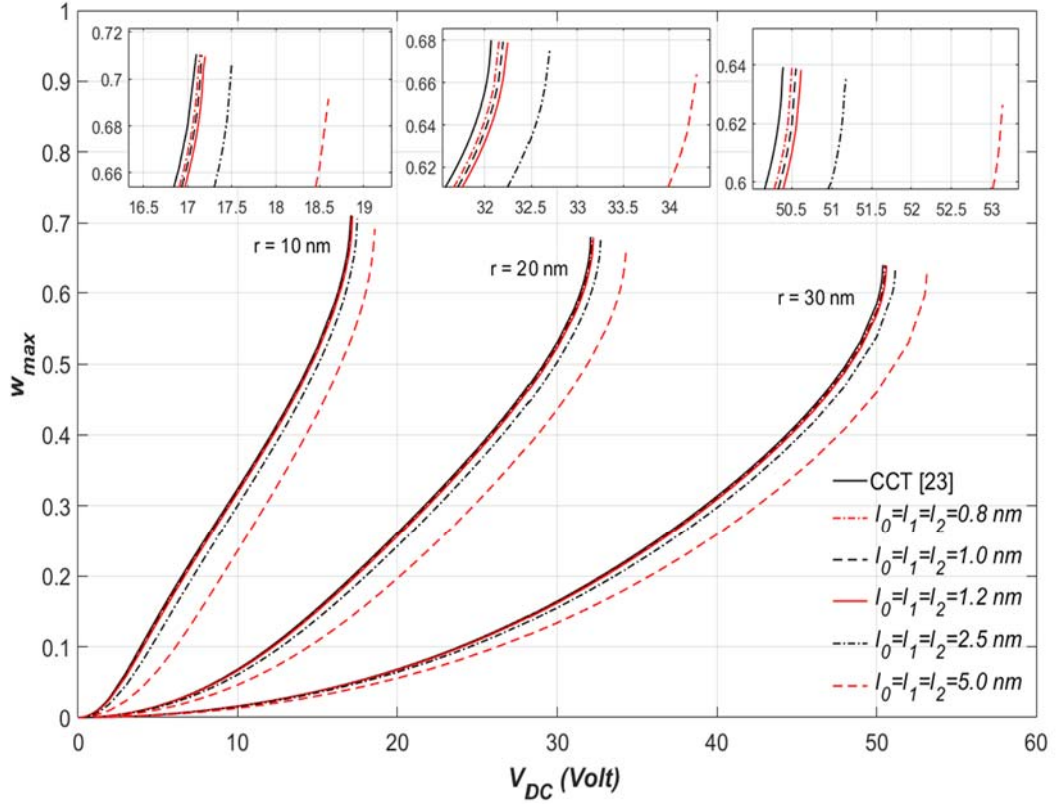


Figure 4.6: Comparison of the normalized maximum static deflection variation of the CNT with the DC voltage when assuming the classical continuum theory (CCT) and the strain gradient theory (SGT) for cases 1, 2, and 3 of Table 4.2, respectively.

In the next coming example, the effect of the strain gradient parameters on the static behavior of the CNT of case 4 in Table 4.2 is investigated. Figure 4.7 depicts the variation of the normalized CNT static with the DC voltage. The figure shows interesting behaviors in the low gate voltage regime, where the inclusion of size scale dependent parameters increases nonlinearly the discrepancies between CCT and SGT for CNT with larger length-to-radius ratio (L/r), as was previously explained in Figure 4.6. This nonlinear effect in the low actuation domain diminishes for CNT with lower length-to-radius ratio (L/r). Furthermore, in the region near the pull-in instability, the size-dependent effect is almost showing a linear stiffening effect resulting in an increase in the

pull-in voltage. Further investigation of strain gradient parameters effects in the low voltage regime will be discussed in later subsection.

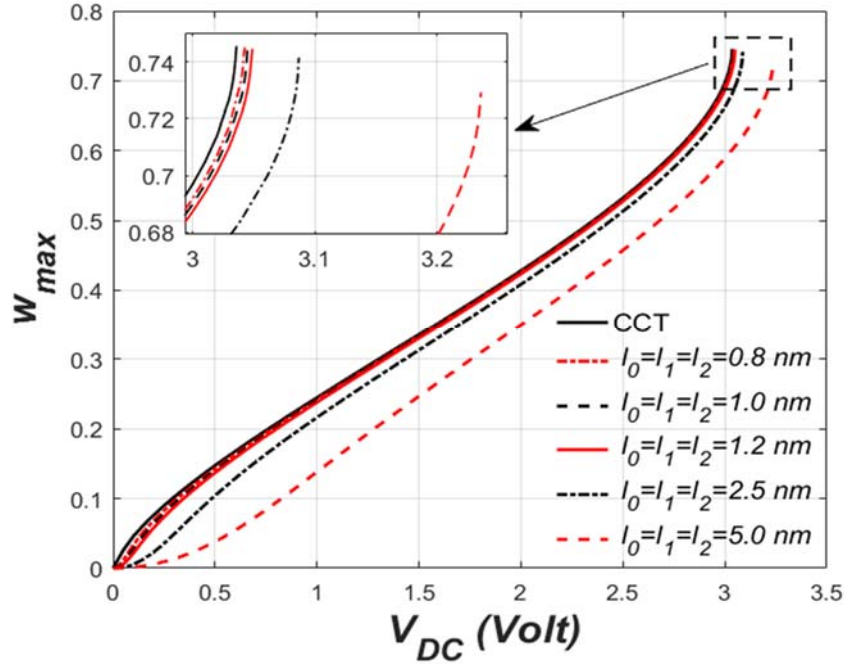


Figure 4.7: Comparison of the normalized maximum static deflection variation of the CNT with the DC voltage when assuming the classical continuum theory (CCT) and the strain gradient theory (SGT) for case 4 of Table 4.2.

To more elucidate the size scale dependent effects on the static deflection profile, we plot the first mode which is the most dominant mode of cases 1, case 2 and 3 of Table 4.2. We assume $l_0 = l_1 = l_2 = l = 5 \text{ nm}$ as a size scale dependent parameter for CNT-based nanobeam with relatively large diameter as presented in Table 4.2. Again, the results show that the size scale dependent parameters are becoming more prominent for smaller diameter of the SCT-based nanobeam. The static deflection deviations between those calculated using classical and non-classical are becoming larger for small diameter, i.e. case 3 in Table 4.2. The results are in agreement with the theory, stated that the size scale

dependent effects are much significant on the smaller geometrical dimensions of the structure.

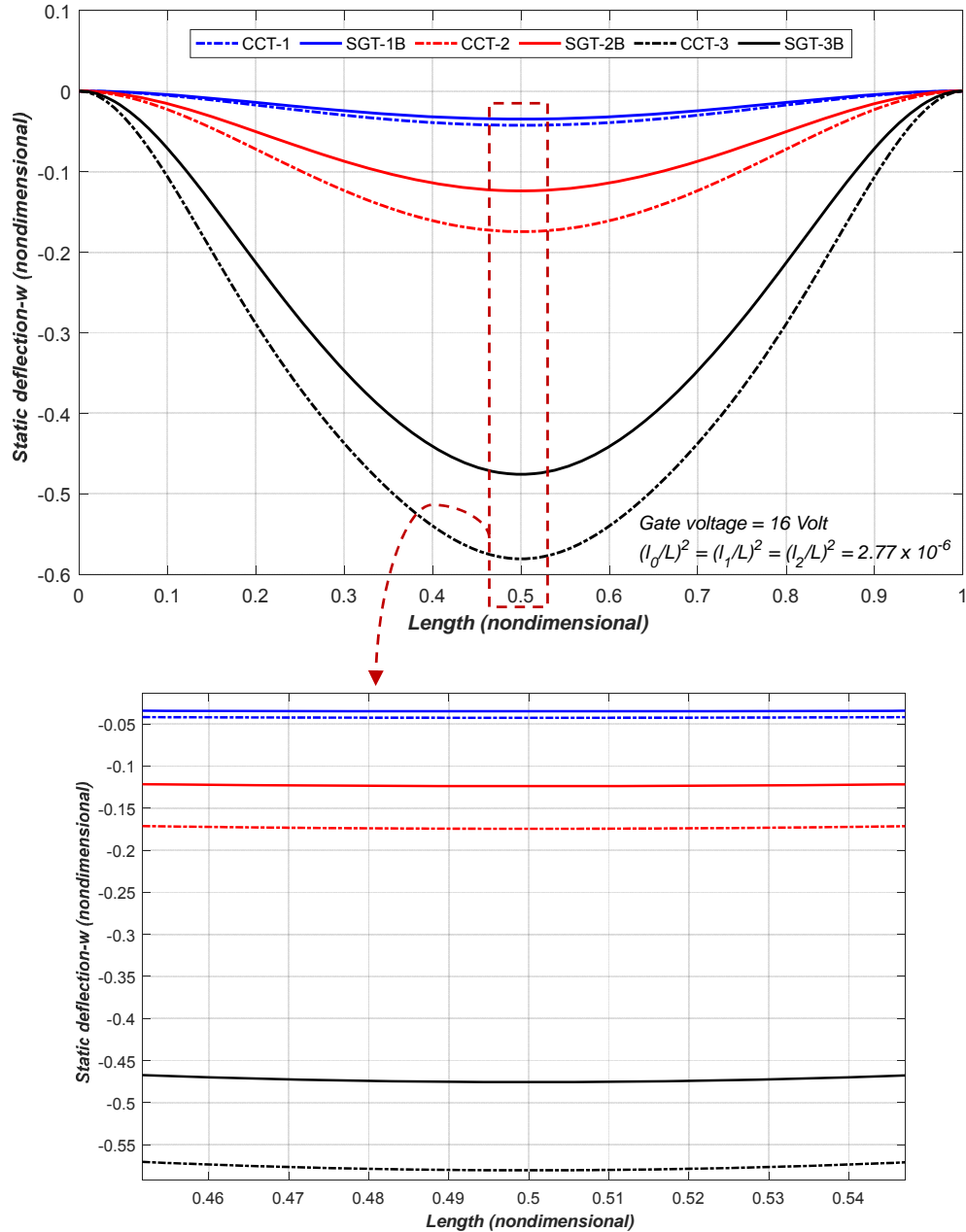


Figure 4.8: Comparison of the CNT static profiles of cases 1, 2 and 3 of Table 4.2, for DC gate voltage of 16 Volt, and when considering the classical continuum theory (CCT), and the strain gradient theory (SGT), respectively.

4.3. The temperature gradient effects

We propose next to investigate the thermal gradient effect on the CNT based nanobeam while considering the SGT. For this, we consider a doubly clamped CNT nanobeam with parameters of cases 5, 6, and 7 of Table 4.2. A straight CNT configuration is assumed to investigate the effect of the thermal gradient only without including the initial curvature (slack) effect. Further discussion about this consideration will be presented later. The CNT coefficient of thermal expansion coefficient was assumed to be equal to $\alpha_T = -1.6 \times 10^{-6} \text{K}^{-1}$ and $\alpha_T = 1.1 \times 10^{-6} \text{K}^{-1}$ for low and high temperature values, respectively, as compared to the room temperature value [42, 44, 72, 107].

4.3.1. Temperature gradient effect to the pull-in voltage and maximum static deflection

In the below, we consider cases 5, 6, and 7 while varying the temperature gradient from -300 K to 300 K . From the summarized results of Table 4.3, we can clearly observe that decreasing the temperature value way below the room temperature tends to stiffen the CNT as indicated by the increase of the pull-in voltage (shrinking effect) and with the decrease of the maximum deflection at the pull-in. The total contrary behavior is occurring for the cases of a temperature increase with respect to the room temperature. This is demonstrating that with any increase of the thermal gradient, the nanobeam would feel a positive axial compressive stresses tending to affect its initial deflection state before even applying any actuating load (expansion effect).

Table 4.3: Effect of the temperature gradient variation on the CNT pull-in gate voltage and its respective normalized maximum deflection.

Case ΔT (K)	Case 5		Case 6		Case 7	
	Volt _{PI} *	w_{max}^{PI} *	Volt _{PI}	w_{max}^{PI}	Volt _{PI}	w_{max}^{PI}
-300	31.24	0.7520	43.59	0.7410	50.29	0.7354
-250	31.15	0.7528	43.46	0.7418	50.14	0.7362
-200	31.06	0.7535	43.33	0.7425	49.98	0.7370
-150	30.98	0.7541	43.21	0.7432	49.85	0.7377
-100	30.89	0.7548	43.08	0.7440	49.70	0.7385
-50	30.80	0.7555	42.96	0.7447	49.55	0.7393
0	30.72	0.7562	42.83	0.7455	49.41	0.7400
+50	30.63	0.7569	42.71	0.7464	49.26	0.7408
+100	30.54	0.7576	42.58	0.7469	49.11	0.7415
+150	30.46	0.7582	42.45	0.7477	48.97	0.7423
+200	30.36	0.7591	42.33	0.7484	48.82	0.7430
+250	30.27	0.7598	42.20	0.7492	48.67	0.7438
+300	30.18	0.7605	42.07	0.7500	48.52	0.7446

* PI and w_{max} stand for pull-in and non-dimensional maximum deflection

Moreover, and in order to investigate the temperature gradient effect in the low voltage regime, we compute the non-dimensional maximum static deflection for the case of $r = 1 \text{ nm}$ (case 5) while varying the gate voltage. The results are depicted in both Figure 4.9 and Figure 4.10, for low and high temperature gradient, respectively. As depicted in Figure 4.9, the CNT static profiles are completely different due to the

shrinking effect in the low-temperature regime. In fact, the nonlinear effect of the temperature appears from the low gate voltage until approximately one-third the pull-in voltage, then all static curves share almost a linear temperature gradient effect till the pull-in instability. In comparison, Figure 4.10 shows that considering high-temperature gradient values, the CNT would be initially curved due to the thermal axial compressive stresses. This effect is somehow similar to the initially curved (slacked) doubly clamped structures [24]. In addition, and as previously reported in [24], the pull-in voltage of slacked CNT is decreased and the non-dimensional maximum deflections in the pull-in point slightly increase. This is what we are exactly getting in Figure 4.10, assuming positive thermal gradient effect.

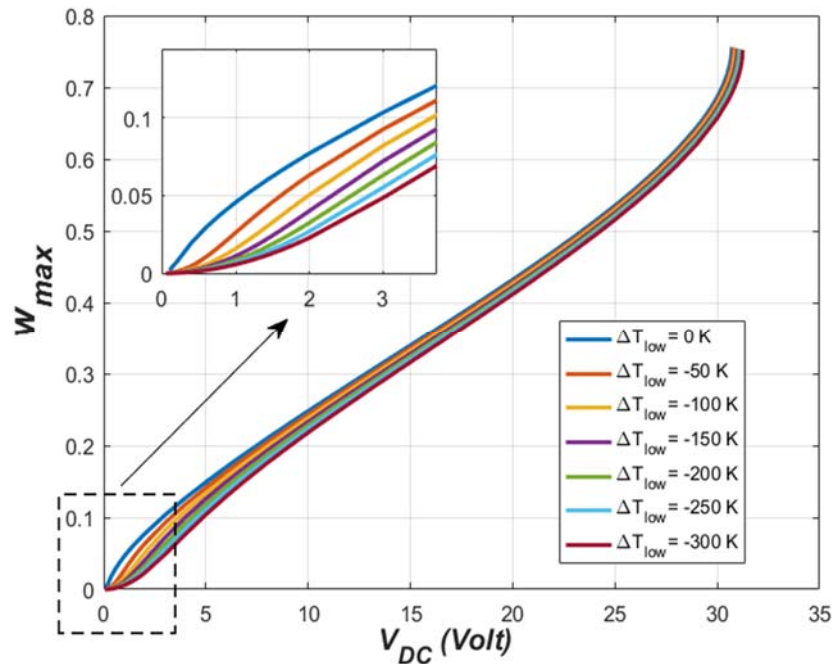


Figure 4.9: Thermal gradient effect on the CNT maximum static deflection of case 5 of Table 4.2 when assuming low-temperature regime.

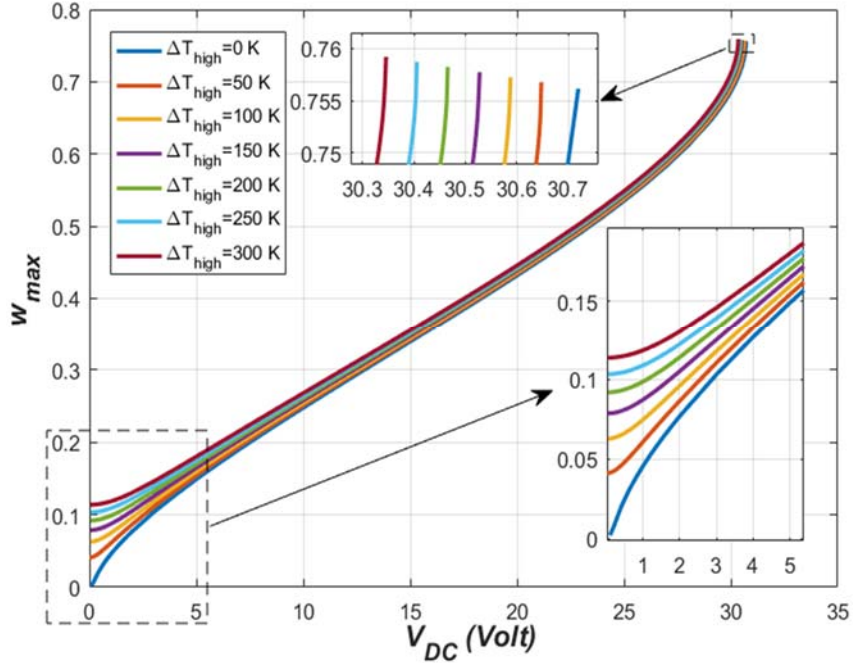


Figure 4.10: Thermal gradient effect on the CNT maximum static deflection of case 5 of Table 4.2 when assuming high-temperature regime.

4.3.2. The critical temperature buckling analysis

This part is organized mainly to investigate the critical (threshold) temperature value that would trigger a thermal expansion sufficient for the buckling initiation of the clamped-clamped CNT based nano-resonator. We calculate this onset value thermal expansion of the CNT by neglecting all the time dependent functions as well as the electrostatic force in the nonlinear beam equation of motion, Eq. (4.3), while conserving the mid-plane stretching term and the temperature gradient. As a numerical case, we consider a CNT on case 5 of Table 4.2. Figure 4.11 displays the CNT static deflection versus an assumed temperature gradient using one mode shape in the ROM process. In the same figure, we assume all size scale dependent parameters equal to $l_0 = l_1 = l_2 = l = 1$ nm. The figure shows that for this case study, a critical buckling thermal threshold is occurring at around 9.4 K. Increasing the temperature gradient value

above this critical thermal threshold will initiate a post-buckling state. The same figure is demonstrating that the CNT exhibits in a nonlinear manner the post-buckling regime when the temperature gradient is furtherly increased.

To compliment the above numerical results, we propose next to compute the CNT critical buckling temperatures while considering different SGT parameters, Figure 4.12. Additionally and in the same figure, the SGT results will be compared with those obtained while assuming classical continuum theory. The classical results show that the critical buckling while considering one mode in the calculation is very small. This finding is in agreement with what was previously reported in Lee and Chang [108]. In fact, they have investigated in their work the critical buckling temperatures of single wall carbon nanotube (SWCNT) using the classical continuum theory, and they have concluded that these critical temperatures are relatively small values for all for the fundamental mode (the first mode of vibration).

Figure 4.12 shows that taking into account the nonlinear geometric terms due to the assumed thermal gradient along with the mid-plane stretching are affecting significantly the computation of the critical thermal buckling thresholds. Similarly, it is clearly shown that increasing the SGT parameters i.e. decreasing the CNT radius to the size scale dependent parameters ratio, tends to increase the critical buckling temperature thresholds, as compared to the classical continuum theory. This is mainly due to the stiffening effect of the CNT-based nanobeam in the presence of higher-order strain gradient deformations. That to say that the strain gradient effects are considerably related to the stiffness of any considered nanostructure [32].

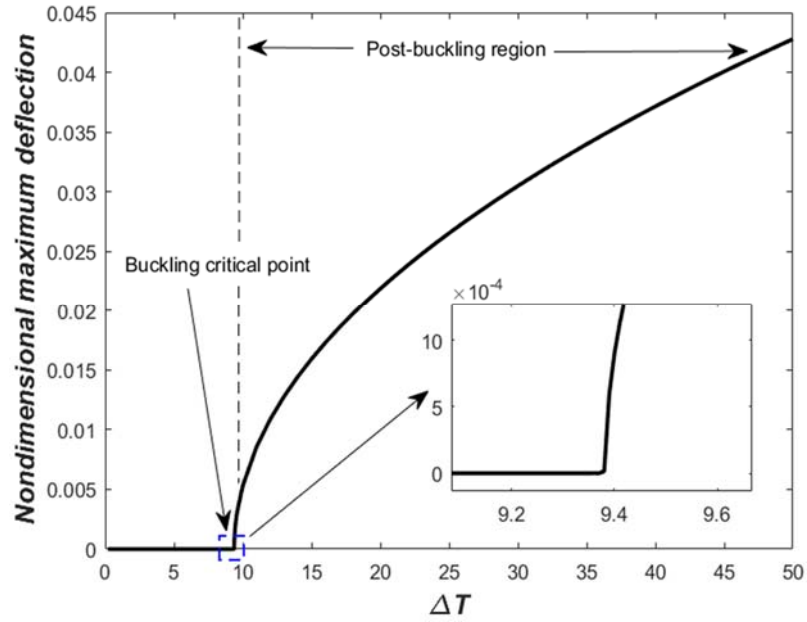


Figure 4.11: Variation of CNT maximum static deflection with an assumed temperature gradient excitation and while assuming a SGT parameters of $l_0 = l_1 = l_2 = l = 1 \text{ nm}$.

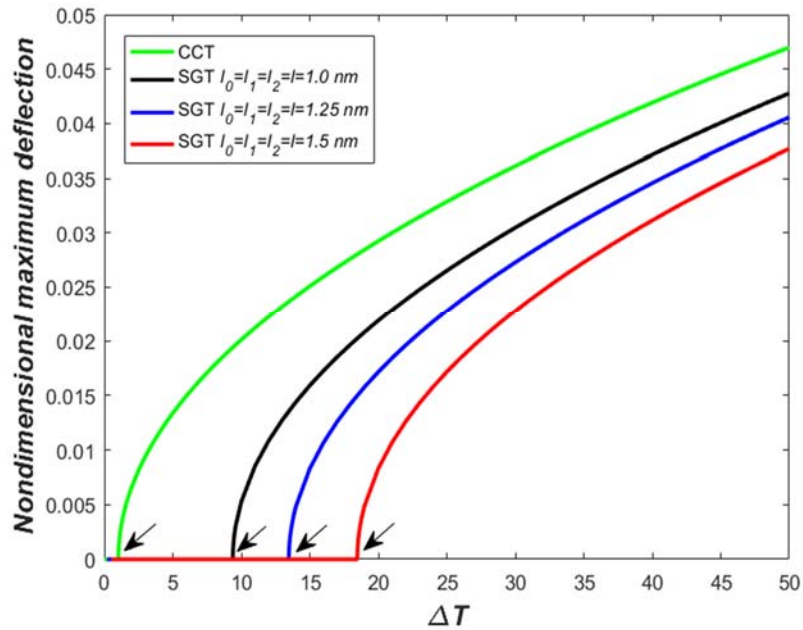


Figure 4.12: Variation of the CNT maximum static deflection with an assumed temperature gradient excitation and while varying the strain gradient parameters as follows: $l = 0 \text{ nm}$ (the classical continuum theory case), $l = 1.0 \text{ nm}$, $l = 1.25 \text{ nm}$, and $l = 1.5 \text{ nm}$.

CHAPTER 5

EIGENVALUE PROBLEM

In this chapter, we propose to investigate the size scale dependent and thermal gradient effects on the variation of the natural frequencies of the doubly-clamped carbon nanotube with various static DC actuating voltages. Toward this, we consider an un-damped eigenvalue problem while including the geometric nonlinearity, nonlinear electrostatic force, size-dependent and thermal gradient in the CNT equation of motion. All the obtained results then are compared with those obtained using classical theory.

5.1. Linearized Eigenvalue Problem Derivation

We first derive the linearized eigenvalue problem (LEVP) to investigate the size scale dependent and thermal gradient effects on the natural frequency of CNT-based nanobeam. The normalized equation of motion with the respective boundary conditions of the doubly clamped CNT beam with slack can be re-written as:

$$\begin{aligned} \ddot{\hat{w}} = & -\beta_0 \hat{w}^{vi} - \hat{w}^{iv} + \beta_3 F_e(\hat{x}, \hat{t}) + \\ & + \left[-\beta_2 \alpha_T \Delta T + \beta_1 \left(\int_0^1 (\hat{w}')^2 d\hat{x} - 2 \int_0^1 (\hat{w}' \hat{w}'_0)^2 d\hat{x} \right) \right] (\hat{w}'' - \hat{w}''_0) \end{aligned} \quad (5.1)$$

Considering the Galerkin decomposition of Eq. (3.38) and substituting it into the above un-damped equation of motion, we obtain the following normalized equations function of the time-varying modal coordinates and the space function mode shapes, respectively:

$$\begin{aligned}
& \int_0^1 \left(\frac{\partial}{\partial \hat{t}} \left(\frac{\partial \sum_{i=1}^n u_i(i) \phi_i(\hat{x})}{\partial \hat{t}} \right) \phi_j(\hat{x}) \right) dx = -\beta_0 \int_0^1 \left(\frac{\partial^6 \left[\sum_{i=1}^n u_i(i) \phi_i(\hat{x}) \right]}{\partial \hat{x}^6} \right) \phi_j(\hat{x}) dx - \int_0^1 \left(\frac{\partial^4 \left[\sum_{i=1}^n u_i(i) \phi_i(\hat{x}) \right]}{\partial \hat{x}^4} \right) \phi_j(\hat{x}) dx + \\
& + \beta_3 \int_0^1 \left(\frac{(V_{dc} + V_{ac} \cos(\Omega \hat{t}))^2}{\sqrt{\left(1 - \sum_{i=1}^n u_i(i) \phi_i(\hat{x}) - w_0\right) \left(1 - \sum_{i=1}^n u_i(i) \phi_i(\hat{x}) - \hat{w}_0 + 2\hat{r}\right)} \cos^{-1} \left(\frac{1 - \sum_{i=1}^n u_i(i) \phi_i(\hat{x}) - \hat{w}_0}{\hat{r}} \right)} \right)^2 \phi_j(\hat{x}) dx + \\
& + \int_0^1 \left(-\beta_2 \alpha_T \Delta T + \beta_1 \int_0^1 \left(\frac{\partial \left[\sum_{i=1}^n u_i(i) \phi_i(\hat{x}) \right]}{\partial \hat{x}} \right)^2 dx - 2 \int_0^1 \left(\frac{\partial \left[\sum_{i=1}^n u_i(i) \phi_i(\hat{x}) \right]}{\partial \hat{x}} \right) \hat{w}_0' dx \right) \left(\frac{\partial^2 \left[\sum_{i=1}^n u_i(i) \phi_i(\hat{x}) \right]}{\partial \hat{x}^2} - \hat{w}_0'' \right) \phi_j(\hat{x}) dx.
\end{aligned} \tag{5.2}$$

Eq. (5.2) can be written in the state-space representation as follows:

$$\dot{\mathbf{U}} = \mathbf{R}(\mathbf{U}), \tag{5.3}$$

where,

$$\mathbf{U} = [x_1 \quad x_2 \quad \dots \quad x_n] = [u_1 \quad \dot{u}_1 \quad u_2 \quad \dot{u}_2 \quad \dots \quad u_n \quad \dot{u}_n], \tag{5.4}$$

The above vector \mathbf{U} represents the modal coordinate vector and $\mathbf{R}(u)$ is the right-hand side vector representing the stiffness coefficients and all the nonlinear terms in Eq. (5.2). We can clearly notice that the vector $\mathbf{R}(u)$ is a nonlinear function of modal coordinate $u_1(t)$. Then, by splitting \mathbf{U} into a static part denoted by \mathbf{U}_{static} , representing the equilibrium position due to the DC actuation, and a dynamic part denoted by $\mathbf{U}_{dynamic}(t)$ representing the small oscillations around the equilibrium position, the vector \mathbf{U} can be written as:

$$\mathbf{U} = \mathbf{U}_{static} + \mathbf{U}_{dynamic}(t), \tag{5.5}$$

Substituting Eq. (5.5) into Eq. (5.4), using a Taylor series expansion for small variation of $\mathbf{U}_{dynamic}(t)$, eliminating the higher-order terms, and imposing that $R(\mathbf{U}_{static}) = 0$, we are left with the below truncated Taylor's series expression:

$$\dot{\mathbf{U}}_{dynamic} \approx \mathbf{J}(\mathbf{U}_{static})\mathbf{U}_{dynamic} + \text{h.o.t.}, \quad (5.6)$$

where $\mathbf{J}(\mathbf{U}_{static})$ is the Jacobian matrix computed at the equilibrium points [24, 109] and h.o.t stands for higher-order terms. If one assume n -modes in the Galerkin decomposition ROM process, the Jacobian matrix will be an $n \times n$ matrix and can then be calculated as follows:

$$\mathbf{J}(x_1, x_2, \dots, x_n) = \begin{bmatrix} \frac{\partial f_1(x_1, x_2, \dots, x_n)}{\partial x_1} & \dots & \frac{\partial f_1(x_1, x_2, \dots, x_n)}{\partial x_n} \\ \vdots & \ddots & \vdots \\ \frac{\partial f_n(x_1, x_2, \dots, x_n)}{\partial x_1} & \dots & \frac{\partial f_n(x_1, x_2, \dots, x_n)}{\partial x_n} \end{bmatrix}, \quad (5.7)$$

where f are the state space form of the EOM for n^{th} mode-shapes.

To compute the natural frequencies of the CNT with any corresponding DC electrostatic voltage, one should substitute the stable static response solution, \mathbf{U}_{static} into the matrix \mathbf{J} and then calculate its corresponding eigenvalues, using the below equation:

$$|\mathbf{J}(\mathbf{U}_{static}) - \lambda I_{matrix}| = 0, \quad (5.8)$$

where I_{matrix} is the identity matrix. Finally, the natural frequencies of the system can be obtained by taking the square roots of the Jacobian matrix eigenvalues.

5.2. Linearized Eigenvalue Problem of straight CNT

5.2.1. Considering one mode LEVP using classical continuum theory

By considering classical continuum theory, the normalized form of equation of motion considering one mode shape can be written as:

$$\ddot{u}_1(\hat{t}) = -Ku_1(\hat{t}) + \alpha_1 \Gamma u_1^3(\hat{t}) + \alpha_2 (V_{dc})^2 \int_0^1 \frac{\phi_1(\hat{x})}{\sqrt{(1-u_1(\hat{t})\phi_1(\hat{x}))(1-u_1(\hat{t})\phi_1(\hat{x})+2\hat{r})} \left(\cos^{-1} \left(1 + \frac{1-u_1(\hat{t})\phi_1(\hat{x})}{\hat{r}} \right) \right)^2} dx \quad (5.9)$$

$$\alpha_1 = 2 \left(\frac{d}{r} \right)^2, \quad \alpha_2 = \frac{\pi \varepsilon_0 L^4}{E I d^2}, \quad (5.10)$$

$$K = \int_0^1 \phi_1^{iv}(\hat{x}) \phi_1(\hat{x}) d\hat{x}, \quad \Gamma = \int_0^1 \left\{ \left(\int_0^1 (\phi_1'(\hat{x}))^2 dx \right) \phi_1''(\hat{x}) \phi_1(\hat{x}) \right\} dx, \quad (5.11)$$

Next, by defining matrix U ,

$$U = \begin{bmatrix} x_1 \\ x_2 \end{bmatrix} = \begin{bmatrix} u_1 \\ \dot{u}_1 \end{bmatrix}, \quad (5.12)$$

Then, 1-mode form of the Jacobian matrix can be written as:

$$J(x_1) = \begin{bmatrix} \frac{\partial f_1(x_1, x_2)}{\partial x_1} & \frac{\partial f_1(x_1, x_2)}{\partial x_2} \\ \frac{\partial f_2(x_1, x_2)}{\partial x_1} & \frac{\partial f_2(x_1, x_2)}{\partial x_2} \end{bmatrix}, \quad (5.13)$$

where,

$$\begin{aligned} f_1(x_1, x_2) &= x_2 \\ f_2(x_1, x_2) &= -Kx_1 + \alpha_1 \Gamma x_1^3 + \alpha_2 (V_{dc})^2 \int_0^1 \frac{\phi_1(\hat{x})}{\sqrt{(1-x_1\phi_1(\hat{x}))(1-x_1\phi_1(\hat{x})+2\hat{r})} \left(\cos^{-1} \left(1 + \frac{1-x_1\phi_1(\hat{x})}{\hat{r}} \right) \right)^2} d\hat{x} \end{aligned} \quad (5.14)$$

The results for case 1 of Table 4.2 are depicted in Figure 5.1.

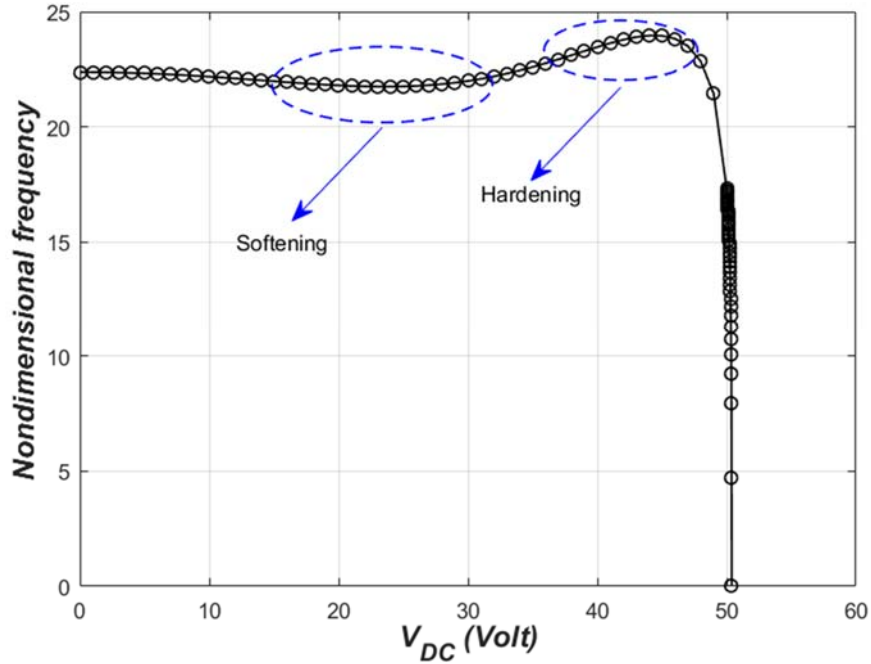


Figure 5.1: Variation of the first in-plane (fundamental) natural frequency with the DC load of the CNT of case 1 of Table 4.2 assuming the classical continuum theory.

The figure shows the natural frequency of CNT-based nanobeam with large diameter. The frequency is slightly decreasing while increasing the actuation load until 30 Volt, showing the softening effect due to quadratic nonlinearity is more prominence. Applying the larger actuation load near the pull-in, the frequency increases indicating the hardening effect due to prominent cubic nonlinearity, then it suddenly drop to zero exactly at the pull-in voltage.

To more investigate the natural frequency on the smaller diameter of CNT-based doubly clamped nanobeam, we consider case 3 of Table 4.2 as the next numerical example. The results are depicted in the Figure 5.2. The figure is showing slightly different characteristic compared to Figure 5.1. As one can see that for the beam with

large length-to-radius ratio (L/r), the softening behavior is not observed. The natural frequency dramatically increases with the increases of actuation load without any decreasing point, and suddenly drop to zero at the pull-in voltage. The absent of softening behavior is due to the mid-plane stretching effect is more prominent over the electrostatic actuating load.

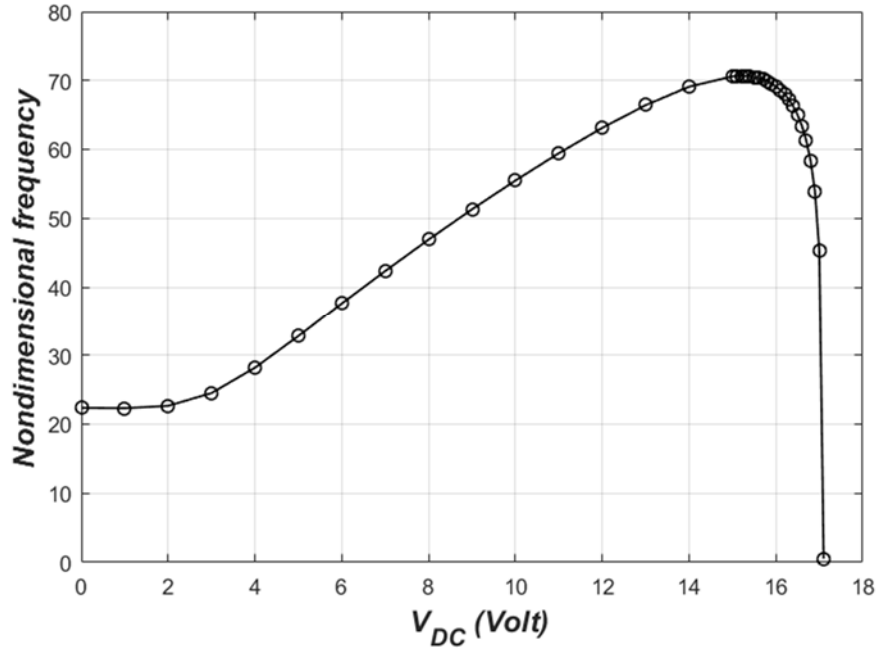


Figure 5.2: Variation of the first in-plane (fundamental) natural frequency with the DC load of the CNT of case 3 of Table 4.2 assuming the classical continuum theory.

5.2.2. Considering five mode LEVP using classical continuum theory

Next, we consider LEVP up to five modes using classical theory. One modify the Eq. (5.1) by dropping strain gradient effect and slack function,

$$\begin{aligned} \ddot{\hat{w}} &= -\hat{w}^{iv} + \alpha_2 F_e(\hat{x}, \hat{t}) + \alpha_1 \left(\int_0^1 (\hat{w}')^2 d\hat{x} \right) \hat{w}_o'', \\ w(\hat{x}, \hat{t}) &\approx \sum_{n=1}^5 u_n(\hat{t}) \phi_n(\hat{x}), \end{aligned} \quad (5.15)$$

We define the matrix \mathbf{U} as:

$$U = [x_1 \ x_2 \ x_3 \ x_4 \ x_5 \ x_6 \ x_7 \ x_8 \ x_9 \ x_{10}] = [u_1 \ \dot{u}_1 \ u_2 \ \dot{u}_2 \ u_3 \ \dot{u}_3 \ u_4 \ \dot{u}_4 \ u_5 \ \dot{u}_5], \quad (5.16)$$

We assume a straight CNT of the case 1 and 3 of Table 4.2 as numerical cases to be investigated. The results are plotted in Figure 5.3(a) and Figure 5.3(b). In the case 1, one can see that the higher mode natural frequencies of the large radius beam are almost insensitive to the electrostatic actuation load while considering CNT with large radii. The CNT with smaller radii is more sensitive to the actuation load as shown by the stiffening effect occurrences even for small gate voltage. For both case, stiffening effects of the higher modes are prominent near the pull-in. Nevertheless, both cases show that first mode frequency is dropping to zero at the pull-in voltage.

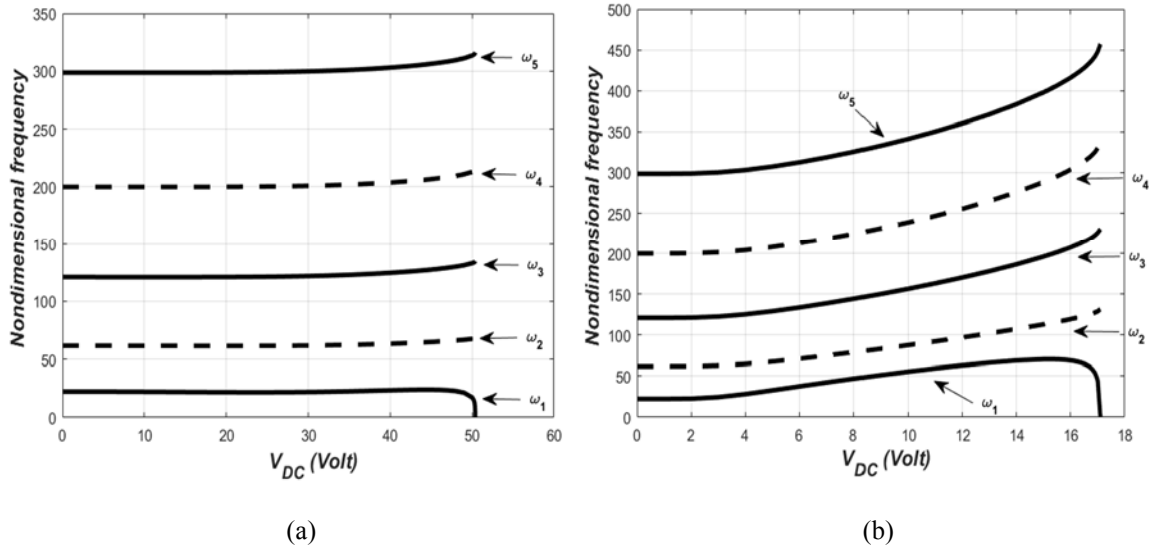


Figure 5.3: Variation of the first five in-plane natural frequencies with the DC load assuming the classical continuum theory of the CNT of (a) case 1 from Table 4.2. (b) case 3 from Table 4.2.

5.2.3. Considering five mode LEVP using strain gradient theory

In this part, we will use all the procedure presented in section 5.1 to calculate the natural frequency of CNT-based nanobeam in the present of strain gradient effect. The only part in the equation that should be dropped is the thermal gradient, which will be discussed in the next section. As a first case study in this eigenvalue problem section, we assume a straight CNT of the case 2 of Table 4.2. We propose in the below to compute the variation of its natural frequencies with the DC load and while varying the size scale dependent parameters as well. Note here that we considered both symmetric and asymmetric mode-shape in the below calculation in order to capture all possible modes: the odd and even in-plane natural frequencies of the CNT nanobeam.

Figures 5.4(a) and 5.4(b) depict the variation of the normalized and dimensional fundamental frequency with the DC voltage and for various size scale parameters, respectively. As clearly observed from Figure 5.4(a), the non-classical theory tends to underestimate the normalized frequencies of the CNT. In fact, for all simulated cases in the same figure, it can be noted that the fundamental frequency is decreasing slightly in for low values of the gate voltage, and then start to sharply increase for higher DC values and more particularly near the pull-in voltage instability, where a suddenly drop to zero of the frequency is observed. Watching judiciously Figure 5.4(b), which represents another version of Figure 5.4(a) but while considering dimensional unit for the fundamental frequency, we can conclude that in the low voltage actuation regime, the non-classical effect tends to increase the natural frequency of the nanobeam, but this phenomenon then reciprocally changes when the actuation load increases near the pull-in

instability. As to that, we can notice that in for gate voltages higher that 20 Volt, the results of SGT are lower than the classical results.

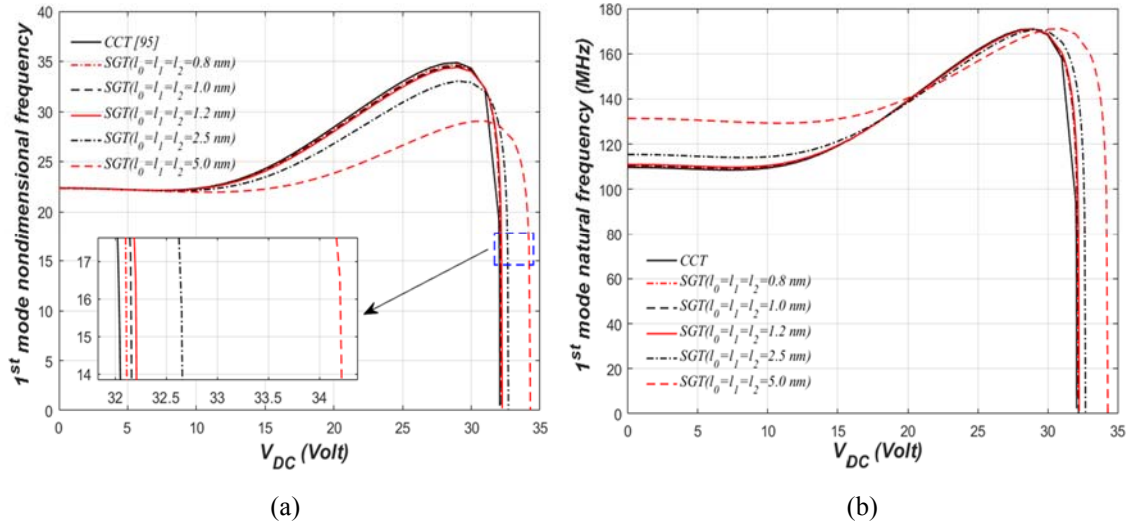


Figure 5.4: Variation of the first in-plane (fundamental) natural frequency with the DC load of the CNT of case 2 from Table 4.2 [95] assuming both the classical continuum theory and the strain gradient theory: (a) nondimensional form, and (b) dimensional form (in *MHz*).

Next, we propose to study the length scale parameters effects on the higher symmetric and anti-symmetric modes of vibrations of the CNT-based nanobeam. Thus, the variation of the second and higher frequencies versus DC voltage are plotted in both Figure 5.5 and Figure 5.6 to look into the effect of the length scale parameters. Figure 5.5 shows the nonlinear variation with the DC load of the second mode natural frequency. Figure 5.5(a) states again that the classical theory overestimates the normalized second frequency whereas Figure 5.5(b) clearly displays the stiffening effect of the SGT model as depicted by the increase of natural frequency mainly in the lower values of the DC voltage. Moreover, this stiffening effect tend to decrease when the DC load is approaching the pull-in voltage. These eigenvalue problem results are consistent with the

static analysis both stating that the stiffening behavior is more dominant in the low gate voltage regime.

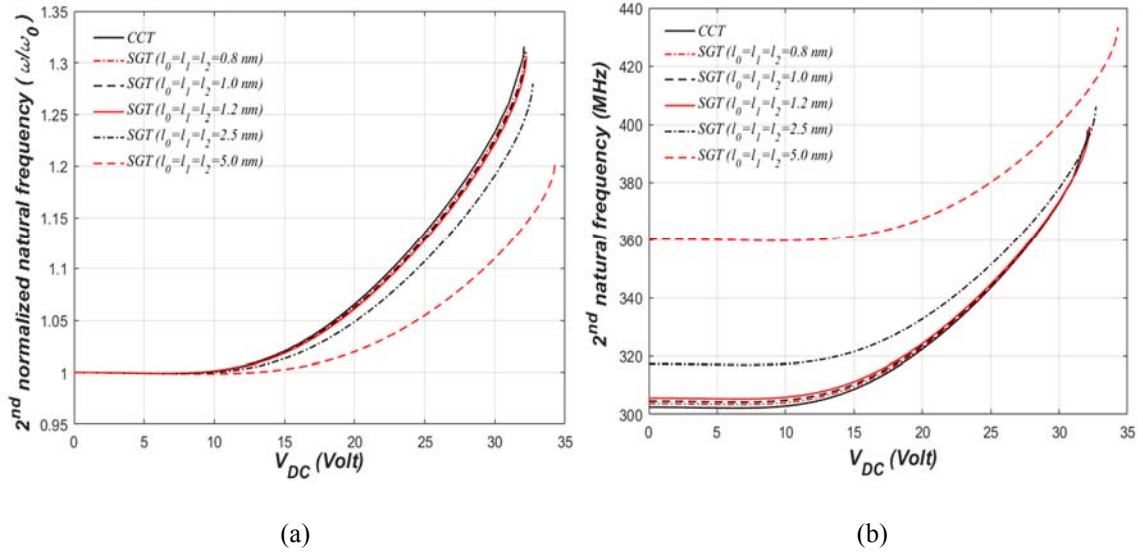


Figure 5.5: Variation of the second in-plane natural frequency with the DC load of the CNT of case 2 from Table 4.2 [95] assuming both the classical continuum theory and the strain gradient theory: (a) nondimensional form, and (b) dimensional form (in MHz).

To further study what happens in the higher order modes, we plot the variation of the higher frequency with the DC load and for various length scale parameters. As depicted in Figure 5.6, the qualitative behavior of the second up to the fifth frequencies are similar, but different from the first fundamental frequency. In fact, as explained before, the first fundamental frequency exhibits a slight decrease followed by an increase for increasing DC voltage before the occurrence of pull-in instability. Increasing the values of the length scale parameter leads to an increase in the fundamental frequency for low DC voltages and then the opposite effect is observed in addition to a further growth of the pull-in voltage. Furthermore, when the length scale parameters increase, all the higher order frequencies (second up to the fifth) are

increasing, and this increase is more and more prominent for the higher frequencies. Finally, the same figure shows that for a straight CNT case study, the natural frequency are highly tunable while varying the magnitude of DC gate voltage. All higher frequencies are drastically increasing with the DC load and more particularly near the pull-in instability. Furthermore, their variation profiles with the DC load showed not a single possibility of modes veering or even modes crossing.

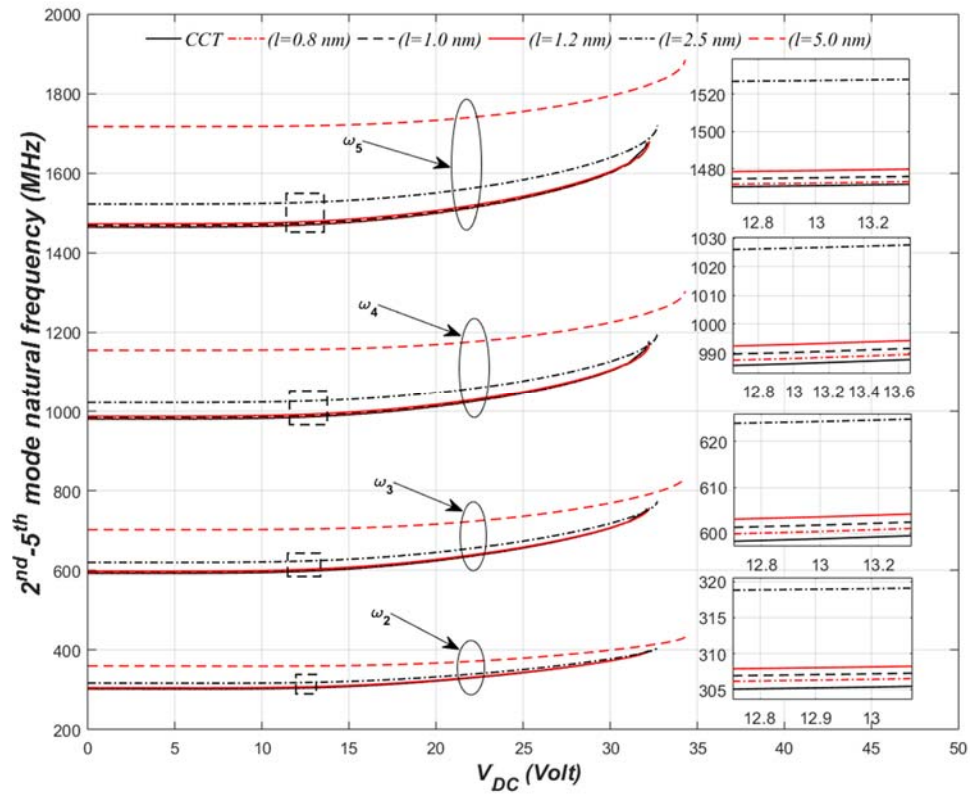


Figure 5.6: Variation of the second, third, fourth and fifth in-plane natural frequencies (in MHz) with the DC load of the CNT of case 2 from Table 4.2 [95] assuming both the classical continuum theory and the strain gradient theory.

5.3. Linearized Eigenvalue Problem of Slacked CNT

In this section, we propose to investigate both effects of the CNT initial curvature (slack) as well as the size scale dependent parameters. As a first case study, one consider

the same CNT's parameters as previously reported in [24]. One also compute the natural frequencies for zero gate voltage while varying the slack and the size scale dependent parameters. Here, one assume the CNT initial curvature as described by the following profile function $w_0(x) = (b_0/d) \sin(\pi x)$ [96]. Then, the level of slack are computed as follows: $\text{Slack}(\%) = (L' - L) / L$, where L' is the CNT length in the deformed/slacked state and L is its length in the perfectly straight state.

5.3.1. Considering classical theory

One modify Eq. (5.2) by dropping the size scale dependent and thermal gradient terms in order to get the normalized equation of motion of classical Euler-Bernoulli beam theory. The equation can be written as:

$$\begin{aligned} \frac{\partial}{\partial t} \left(\frac{\partial \sum_{i=1}^n u_i(\hat{i}) \phi_i(\hat{x})}{\partial \hat{t}} \right) = & - \frac{\partial^4 \left[\sum_{i=1}^n u_i(\hat{i}) \phi_i(\hat{x}) \right]}{\partial \hat{x}^4} + \\ & + \alpha_2 \frac{(V_{dc})^2}{\sqrt{\left(1 - \sum_{i=1}^n u_i(\hat{i}) \phi_i(\hat{x}) - w_0\right) \left(1 - \sum_{i=1}^n u_i(\hat{i}) \phi_i(\hat{x}) - \hat{w}_0 + 2r\right)} \left(\cos^{-1} \left[1 + \frac{1 - \sum_{i=1}^n u_i(\hat{i}) \phi_i(\hat{x}) - \hat{w}_0}{r} \right] \right)^2 + \\ & + \alpha_1 \left[\int_0^1 \left(\frac{\partial \left[\sum_{i=1}^n u_i(\hat{i}) \phi_i(\hat{x}) \right]}{\partial \hat{x}} \right)^2 d\hat{x} - 2 \int_0^1 \left(\frac{\partial \left[\sum_{i=1}^n u_i(\hat{i}) \phi_i(\hat{x}) \right]}{\partial \hat{x}} \right)^2 \hat{w}_0' dx \right] \left(\frac{\partial^2 \left[\sum_{i=1}^n u_i(\hat{i}) \phi_i(\hat{x}) \right]}{\partial \hat{x}^2} - \hat{w}_0'' \right), \end{aligned} \quad (5.17)$$

As previously reported in [24], for the case of initially curved CNTs, and assuming classical continuum theory, mode-veering states occur between two adjacent asymmetric (odd) modes, while mode-crossing states also arise between two nearby symmetric and anti-symmetric modes, respectively. Then, and while varying the size scale dependent parameters, we intend to observe any possibility of mode veering and mode crossing. In the below reported figures, we used red circle to mark the mode-veering locations and red

arrows to mark the mode-crossing positions. One calculate until first five modes in this investigation. Figure 5.7 shows the results exactly the same with the results reported by Ouakad and Younis [24] in despite of the used of fewer modes which were considered in the calculation. We will discuss this results along with analysis of strain gradient effect for this similar case in the next coming part.

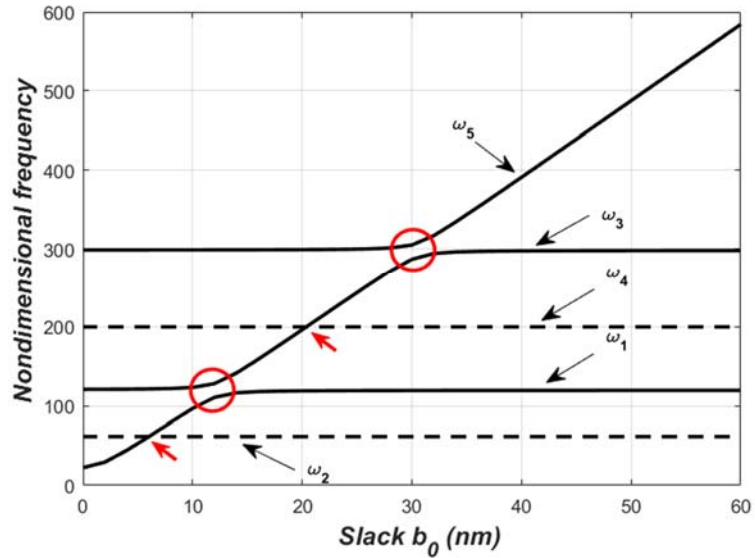


Figure 5.7: Variation of the first five nondimensional in-plane natural frequencies with the slack level and for zero DC load of the CNT of case 8 from Table 4.2 assuming the classical continuum theory.

5.3.2. Considering strain gradient theory

Next, we use the Eqs. (5.2) and (5.17) to calculate the natural frequency of the slacked CNT-based nanobeam both using classical and non-classical theory and then compare the results. We investigate the case of zero gate voltage as well as gate voltage variations. The same red circle and red arrow marks are still used to make clear understanding of the plots. These plots are useful to further predict how many mode veering and crossing points could possibly occur while varying the gate voltages.

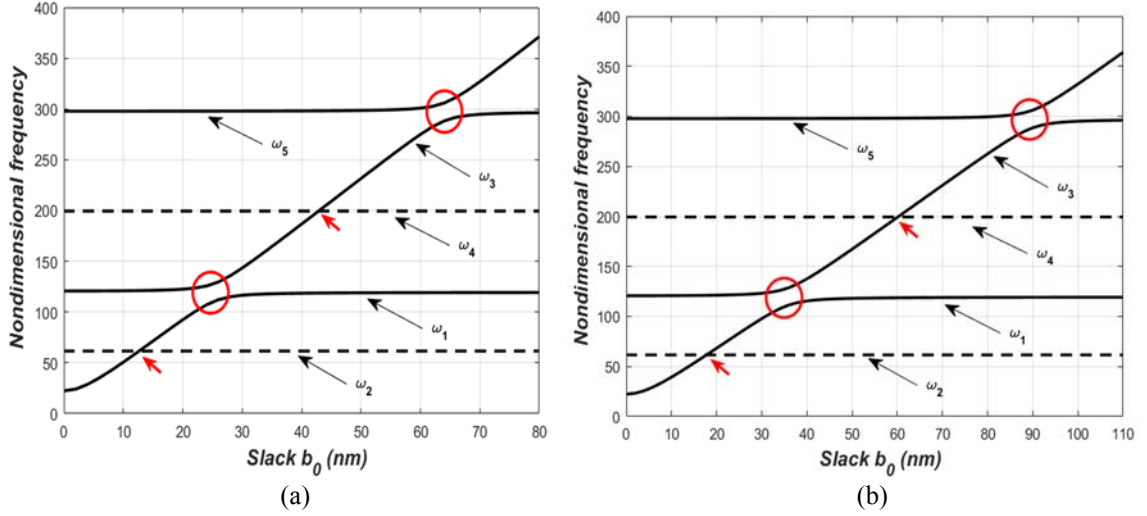


Figure 5.8: Variation of the first five nondimensional in-plane natural frequencies with the slack level and for zero DC load of the CNT of case 8 from Table 4.2 assuming the strain gradient theory (SGT) with: (a) $l = 1.0 \text{ nm}$, and (b) $l = 1.5 \text{ nm}$.

First, one compares the variation of the first five natural frequencies with the slack levels and for zero DC load while considering the classical continuum theory and the strain gradient theory as depicted in the Figure 5.7 and Figure 5.8, respectively. The figure is illustrating some interesting results. It can first be observed that the size dependent parameter slightly affect the results for low slack levels, however it significantly deviates from the classical continuum outcomes for higher slack levels. The figure reveals that the mode-veering and mode-crossing locations are all shifted to higher slack values while increasing of the size scale dependent parameters. This indicates that taking into account the higher order strain gradient is somehow reducing the effective slack effect of the structure. Therefore, the mode-veering and crossing predictions could be erroneous if assuming classical continuum theory.

To more elucidate on the size-dependent parameters effect on the mode-veering and mode-crossing locations, we summarize in Figure 5.9 the occurrence locations of the

mode-veering and crossing slack levels for various size scale dependent parameters ranging from zero (representing the classical continuum theory) and up to values around 1.5 nm. Note that we considered here only the first five modes (both symmetric and anti-symmetric). The dimensional slack level b_0 (nm) and the one in percentage (%) level are both displayed in Figure 5.9(a) and Figure 5.9(b), respectively. Figure 5.9(a) and Figure 5.9(b) show that the modes veering and crossing as a consequence of slackness are significantly affected by size scale dependent parameter l . One takes a point in the following discussion, by assuming classical theory (i.e. $l = 0$), it is clearly shown in the Figure 5.9(a) that a curved CNT profile with $b_0 = 20$ nm slack triggers a veering point and two crossing points symbolized by (○), (□) and (★), respectively. However, while the SGT-parameter with $l = 0.5$ nm is taken into account, the mode 3-4 (★) crossing point is not observed. Moreover, by taking another numerical case in Figure 5.9(b), while assuming SGT-parameter of $l = 1.5$ nm, one point of veering and one crossing are predicted on the CNT beam with $b_0 = 90$ nm. On the other hand, while assuming classical theory, the two points of veering and crossing (i.e. four points) as predicted by Ouakad and Younis [24]. The results indicate that the effective slack effect was reduced with the increase of size scale dependent. Figure 5.9(a) and Figure 5.9(b) also show that the nonlinearity of this effect is more prominent in the higher modes. Hence, we show the possibility that taking into account the higher order strain gradient will significantly affect the natural frequency of slacked CNT.

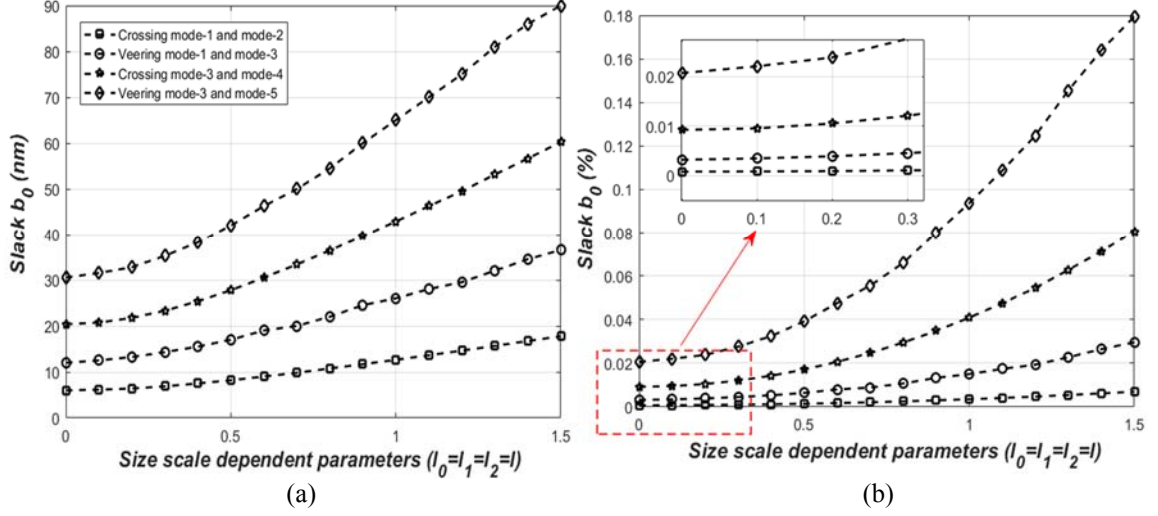
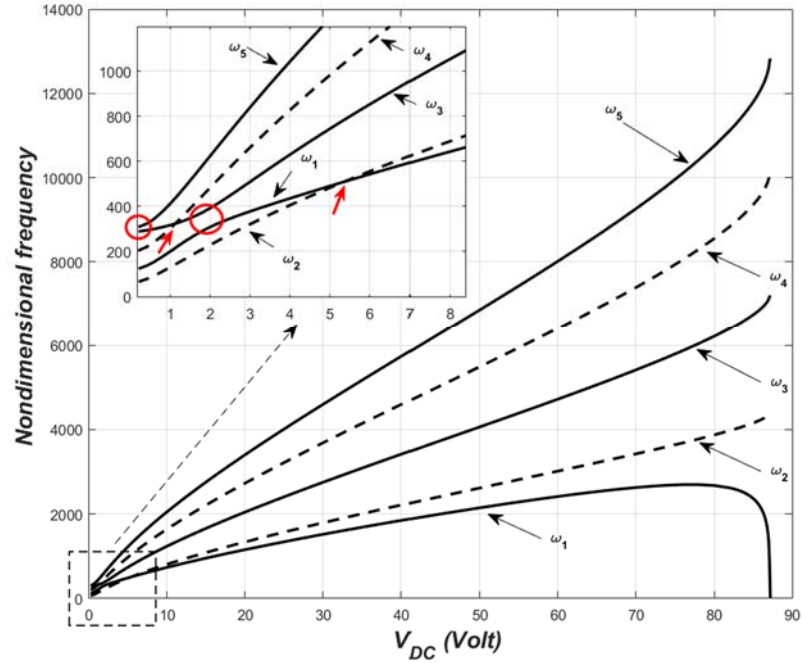


Figure 5.9: Variation of the modes-veering and modes-crossing locus with the SGT size dependent parameter and while assuming: (a) dimensional slack level b_0 in nm , and (b) slack levels in percentage.

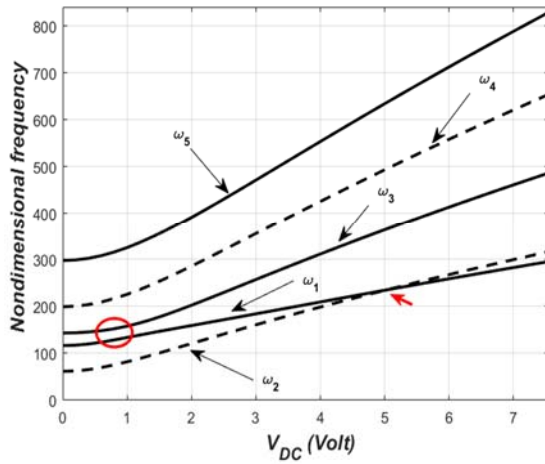
In order to investigate further the higher order strain gradient effect to the mode veering and crossing, we calculate the natural frequency of the assumed CNT-based nanobeam while varying gate voltage. One assumes two slack values as numerical cases, i.e. CNT with slack of 30 nm and 60 nm . Next, we calculated the natural frequency of both slack cases using the classical theory as well as the non-classical theory. In the non-classical theory calculations, two size scale dependent parameters of $l = 1.0\text{ nm}$ and $l = 1.5\text{ nm}$ are assumed. Figure 5.10(a) shows the natural frequency variation versus DC gate voltage of classical CNT-beam with slack of 30 nm . Then, to see the strain gradient effect of non-classical CNT-beam, while assuming the above mentioned two SGT parameters, we calculate the natural frequency variations using Eq. (5.2) as depicted in the Figure 5.10(b) and Figure 5.10(c). Looking carefully the zoomed low gate voltage regime of Figures 5.10(a)-(b), it is clearly shown that the veering and crossing points are significantly changing around the low gate voltage regime below 8 volt. In the Figure

5.10(a), two veering and two crossing points were observed. Surprisingly, we only observe one veering and one crossing frequency in the Figure 5.10(b), then even all the veering is disappear, predicting only one crossing point shown in the Figure 5.10(c) which is considering higher value of SGT parameters.

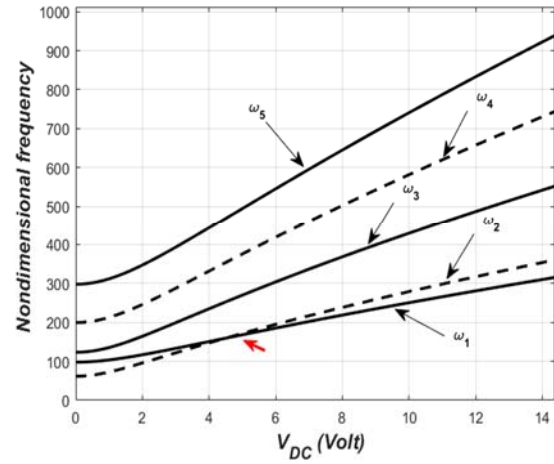
To ensure that these effects are consistent in the larger slack, we assume the slack of $b_0 = 60 \text{ nm}$. As depicted in Figures 5.11(a)-(c), the effective slack effects which are suspected responsible for the veering and crossing occurrence are somehow reduced by the higher order strain gradient effects. These results also confirm that the effects of size dependent parameter are more prominent in the low gate voltage regime as well as in higher mode, as discussed in the static analysis. Again, these results show that the effective slack effects are significantly reduced while taking into account the strain gradient terms in the LEVP. It is worth noting here that the natural frequency dispersions of higher DC gate voltages which are obtained by classical theory are almost showing similar trend compared to those obtained by non-classical theory. Therefore, one plot the LEVP results until the pull-in point for the case of classical theory, and specifically only the zoomed low gate voltage regimes for the non-classical theory LEVP calculations.



(a)

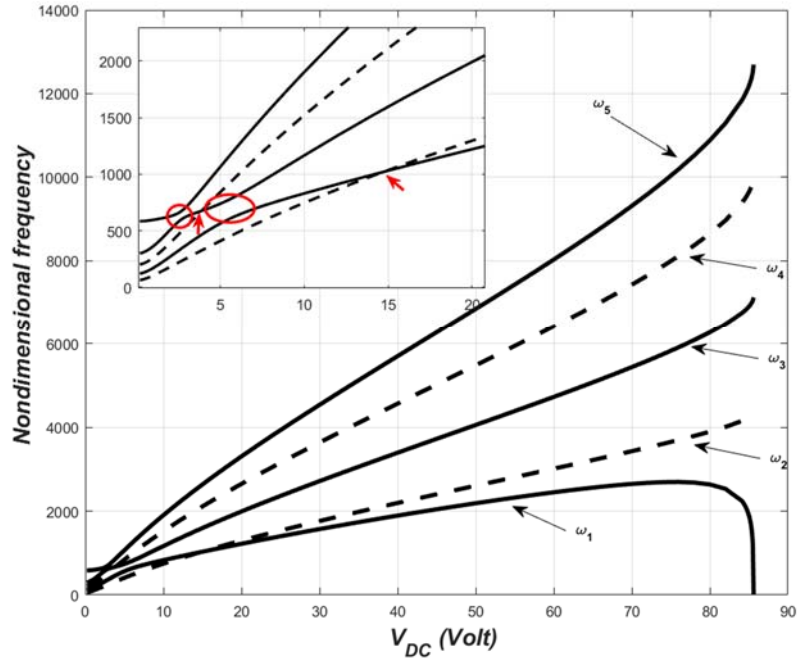


(b)

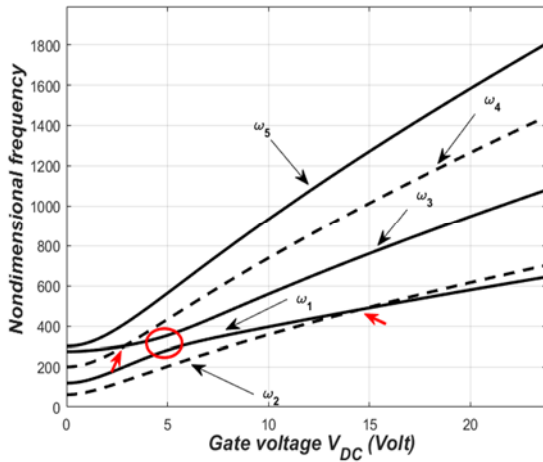


(c)

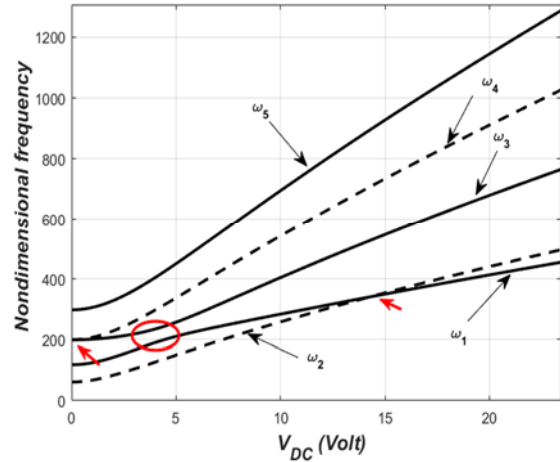
Figure 5.10: Variation of the first five nondimensional in-plane natural frequencies with the DC load, for a slack level of $b_0 = 30 \text{ nm}$ of the CNT of case 8 from Table 4.2 while assuming: (a) the classical continuum theory $l = 0 \text{ nm}$, (b) the strain gradient theory $l = 1.0 \text{ nm}$, and (c) the strain gradient theory $l = 1.5 \text{ nm}$.



(a)



(b)



(c)

Figure 5.11: Variation of the first five nondimensional in-plane natural frequencies with the DC load, for a slack level of $b_0 = 60 \text{ nm}$ of the CNT of case 8 from Table 4.2 while assuming: (a) the classical continuum theory $l = 0 \text{ nm}$, (b) the strain gradient theory $l = 1.0 \text{ nm}$, and (c) the strain gradient theory $l = 1.5 \text{ nm}$.

5.4. Thermal Gradient Effects on The Natural Frequency of CNT-based Nanobeam

In this section, we propose to investigate the natural frequency dispersion of the doubly-clamped CNT-based nanobeam while considering various temperature gradients. It was clearly discussed in the static analysis (Chapter 4) that the temperature gradients are significant in the low gate voltage regime. In order to examine the thermal gradient effect on the natural frequencies dispersion of the doubly clamped straight carbon nanotube, we adopted the following steps: we first examine the variation of the CNT fundamental natural frequency with the DC voltage and for various thermal gradient loads (low and high regimes). Next, we propose to study the effect of the thermal gradient load on the natural frequencies with zero gate voltage in order to predict any possibilities of modes crossing and modes veering in the case of higher temperature gradients. In the last part of this sub-chapter, the dispersion curves for the straight CNT first five natural frequencies are computed through varying the DC actuating amplitude in the low gate voltage regime. It is worth noting here that we propose to analyze all of the above case studies while assuming the strain gradient theory where all size scale dependent parameters are equal to $l_0 = l_1 = l_2 = l = 1 \text{ nm}$. In addition, the geometric mid-plane stretching nonlinearity, post-buckling deflection, the actuating force nonlinearity, and the temperature gradient are all taken into account in the below simulations.

5.4.1. Considering one mode LEVP

In the below simulations, we first consider the linearized EVP with only considering one mode in the ROM and with including the temperature gradient term. We examine the both cases of low and high temperature gradients then we display both

outcomes using two separate figures: Figure 5.12 and 5.12 respectively. In these figures, we display the variation of the first fundamental natural frequency of the CNT of case 5 from Table 4.2.

For the fundamental frequency dispersion in the low temperature gradient regime, Figure 5.12, the results indicate a significant deviation especially around the low gate voltage domain. This is attributed to the dominance of the mid-plane stretching stiffening effect mainly governed by the low temperature gradient in the low DC gate voltage regime. In fact, one can realize that considering low actuating voltage regime (DC voltage below 3 *Volt*), a low temperature gradient tends to increase the natural frequency of the CNT. However this phenomenon is in contrast changing when the DC load increases beyond 3 *Volt* until reaching the pull-in instability, where the frequency drops to zero. This can be attributed to the decrease of the effective CNT length due to a tensile like thermal gradient load. Therefore, the effective mid-plane stretching effect, which principally stiffen the CNT, is then decreased by a tensile load in this low thermal gradient regime. In addition, we can understand from the same plot that for high gate DC voltages, the fundamental frequency values are slightly lower as compared to the room temperature case where $\Delta T \approx 0$. This is mainly due to the dominance of the electrostatic force nonlinearity, at high DC load amplitudes, which is essentially of quadratic (softening) type.

Next, Figure 5.13 depicts the same dispersion of the CNT first natural frequency with the DC load but while assuming high temperature gradients. The obtained results are significantly different as compared to the low temperature gradient results of Figure 5.12. We can visibly comprehend that, in this case, the fundamental frequency increases with

the increase of temperature gradients. This is recognized as the post buckling structural behavior which contributes more than the temperature gradient effect which tends to increase the frequency of the CNT for all assumed values of the DC actuating load. As was previously discussed in Chapter 4, doubly-clamped CNT subjected to high thermal loading tends to expand the length of the CNT. This expansion contributes mostly to curve the straight CNT due to the both clamping boundary conditions right after exhibiting the critical buckling temperature instability. This structural behavior tends to let the cubic geometric nonlinearity to be more dominant, therefore increasing the natural frequency of the CNT based nanobeam. It also can be inferred from Figure 5.13 that the natural frequencies of CNT when assuming high temperature gradients drop earlier to zero (near pull-in) than the case of the room temperature where $\Delta T \approx 0$.

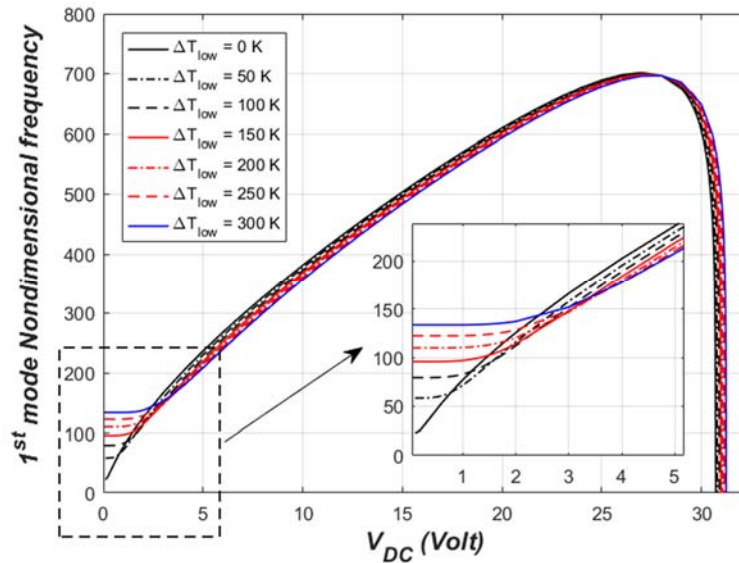


Figure 5.12: Variation of the first nondimensional in-plane (fundamental) natural frequency with the DC load, for zero slack level of the CNT of case 5 from Table 4.2 and for various low temperature gradients, and while assuming SGT with $l = 1 \text{ nm}$.

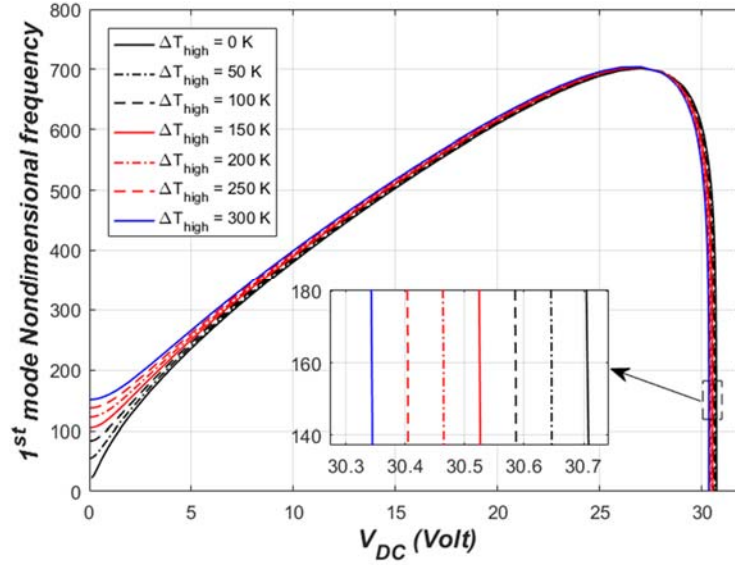


Figure 5.13: Variation of the first nondimensional in-plane (fundamental) natural frequency with the DC load, for zero slack level of the CNT of case 5 from Table 4.2 and for various high temperature gradients, and while assuming SGT with $l = 1 \text{ nm}$.

5.4.2. Considering five mode LEVP

Afterward, we propose to assess the high temperature gradient effect of the doubly clamped CNT-based nanobeam while assuming zero gate voltage. We assume here zero actuation load in order to investigate the CNT mid-plane stretching effect which will be here mainly ruled by any assumed thermal gradient load. As was formerly argued in Chapter 4, doubly clamped CNT based nanobeam behaves like slacked CNT when operated above a critical buckling temperature threshold. To this end, we propose to investigate any possibility of crossing and veering between the first few lower CNT natural frequencies. First, to more understand the above pronounced results of Figure 5.13, we consider the first five modes of vibration in the linearized eigenvalue problem while varying the higher temperature gradient from 0 to 500 K and while assuming the SGT size scale dependent parameters all equal to $l = 1 \text{ nm}$. The results are displayed in Figures 5.14. It can be observed from the figure that the first natural frequency is

increasing nonlinearly with the thermal gradient effect to finally saturate for $\Delta T > 50 K$. It also can be observed that the third and fifth frequencies are also sensitive to the temperature gradients. They both increase nonlinearly as we increase the temperature gradient. The second and fourth frequencies are completely unaffected by the temperature gradient changes, as indicated with the first and second straight dashed lines.

Two mode crossings are observed here (labeled by red arrows in Figure 5.14): the first is occurring for a temperature gradient around 25 K between the first mode and the second one, the second is happening at around 100 K temperature gradient involving the third mode and the fourth mode. Hence, the results of Figure 5.14 show that when the temperature gradient is varied from zero to a value greater than 100 K, two modes crossing will possibly occur. These results also indicate that the mid-plane stretching effect due to the buckling deflection is more prevailing in the post-buckling regime.

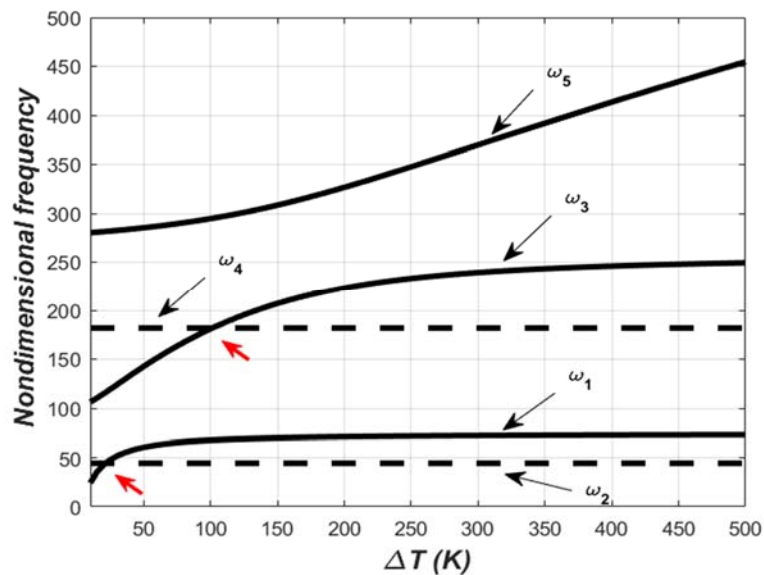


Figure 5.14: Variation of the normalized first five in-plane natural frequencies with various higher temperature gradients, for zero DC load, and while assuming SGT with $l = 1 \text{ nm}$.

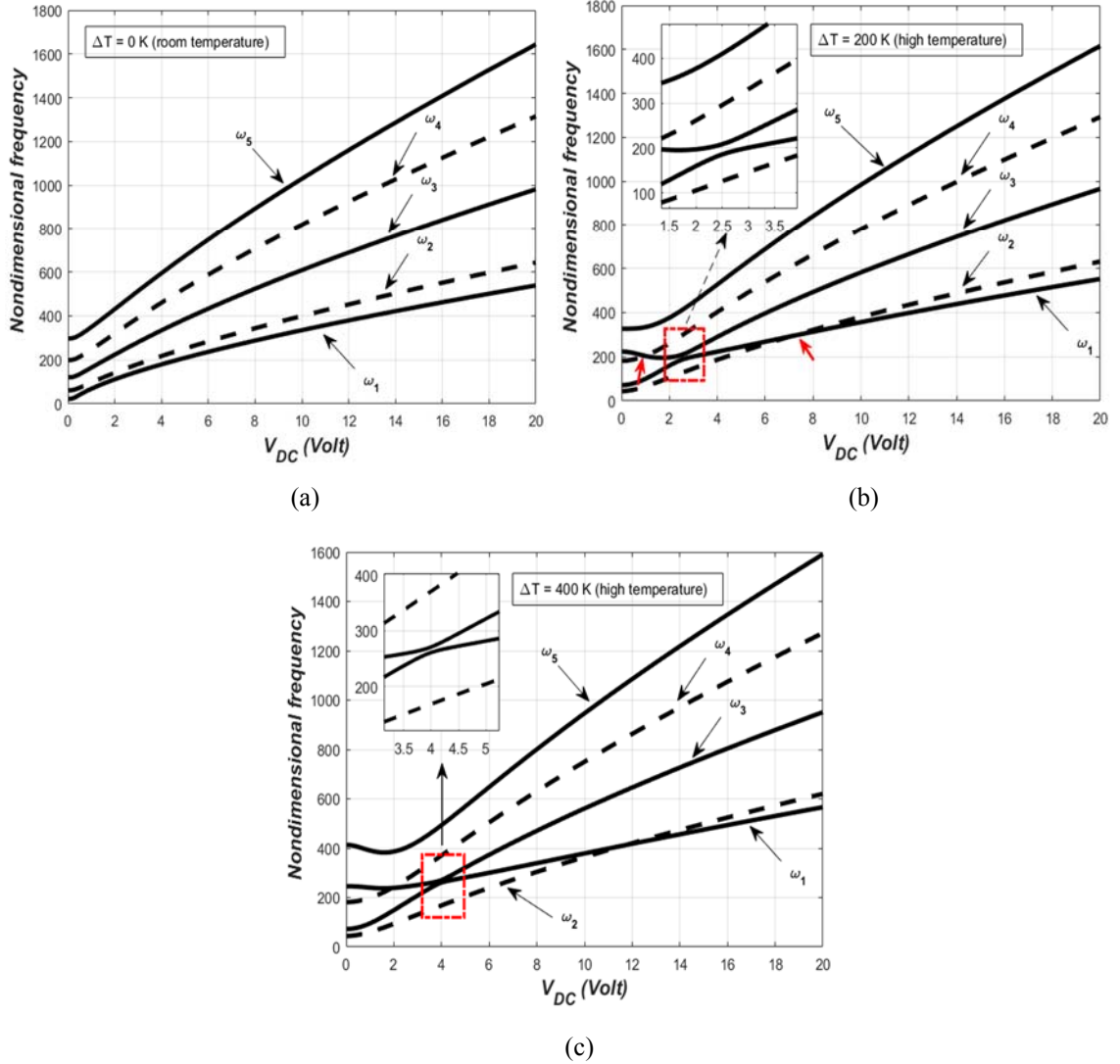


Figure 5.15: Variation of the first five nondimensional in-plane natural frequencies with the DC load, for a straight CNT ($b_0 = 0$ nm) of case 8 from Table 4.2 assuming a strain gradient theory with $l = 1.0$ nm, and for (a) $\Delta T_{high} = 0$ K (room temperature condition), (b) $\Delta T_{high} = 200$ K, and (c) $\Delta T_{high} = 400$ K.

Subsequently, to more clarify the above discussed mode veering and mode crossing issues when assuming high temperature gradients with zero gate voltage, we propose next to investigate these mode interactions options with including the DC electrostatic actuating load. To this end, we consider three different temperature gradient cases:

$\Delta T = 0 K$ (room temperature condition), $\Delta T_{high} = 200 K$ and $\Delta T_{high} = 400 K$, Figures 5.15(a)-(c), respectively. Figure 5.15(a) shows the variation of normalized first five natural frequencies with the applied DC voltage for the room temperature condition. We can observe from the figure that for the case of straight CNT in a room temperature condition, the frequencies dispersion is showing not a single potential of modes crossing or modes veering. These results are in perfect agreement with the outcomes of [24] which reported on the straight CNTs natural frequencies dispersion without considering any thermal gradient effect.

Increasing further the thermal gradient amplitude to higher values as compared to the room temperature situation, Figures 5.15(b) and 5.15(c) display the straight CNT normalized first five in-plane natural frequencies dispersion with the applied DC load and for two different temperature gradient values of $\Delta T_{high} = 200 K$ and $\Delta T_{high} = 400 K$, respectively. We can initially observe from Figure 5.15(b), that assuming temperature gradient $\Delta T_{high} = 200 K$, one modes veering (indicated in the figure by a red dashed square) and two modes crossing (designated by two red arrows) were introduced at low gate voltages, i.e. $0 Volt < V_{DC} < 10 Volt$. A veering between the first mode and the third one is occurring around a gate voltage of $2.5 Volt$, however this was not predicted in the case of room temperature condition, Figure 5.15(a). In addition, when we increased the temperature gradient to $\Delta T_{high} = 400 K$, Figure 5.15(c), we observed that the extra thermal gradient load resulted into an extra thermal expansion and therefore an addition deflection in new post-buckling state of the CNT. We can also see that the additional thermal gradient loads resulted into altering the modes veering and modes crossing

locations. It is clearly shown in Figure 5.15(c) that the first-third modes veering location is shifted to a higher gate voltage around 4 *Volt*, as compared to 2.5 *Volt* in the case of $\Delta T_{high} = 200 K$. The modes crossing positions are also moved to higher gate voltages as we increased of the higher temperature gradient. Moreover, one can observe that the third and fifth natural frequencies are slightly decreasing in low gate voltage regime to then increase with the increase of the DC load. This indicate that the CNT is of softening effect governed by its initial post-buckling deflection state in the low gate voltage regime, to the become less dominant as compared to geometric cubic nonlinearity with tends to stiffen the nano-structure when increasing the gate voltage amplitude.

Lastly, we consider next studying the low temperature gradient effect with assuming two different cases, $\Delta T_{low} = -200 K$, Figure 5.16(a), and $\Delta T_{low} = -400 K$, Figure 5.16(b), for the sake of verifying the integrity of the static buckling analysis of Chapter 4, where we indicated that the CNT length reduction effect is dominant in the low gate voltage regime. We can clearly see from both figures the dominance of the stiffening effect (increase of all natural frequencies) in the CNT structural behavior for all considered DC amplitudes and in the low temperature gradient conditions.

It can similarly be observed that there are no possibilities of modes veering and modes crossing occurrences. This is mainly attributed to the reason that assuming low thermal gradient loads would always result into straight CNT based nanobeam configuration. In addition, the natural frequencies dispersion in this case of CNT operating under very low ambient temperature values indicate exactly the same trend as for the case of straight CNT with ambient temperature condition. The straight CNT with low thermal gradient values will remain straight due to the reduction in its effective

length. Indeed, decreasing the temperature will increase the natural frequency in the low gate voltage, therefore the hardening mid-plane stretching effect convert to be more dominant than the softening electrostatic actuation term in these loading conditions.

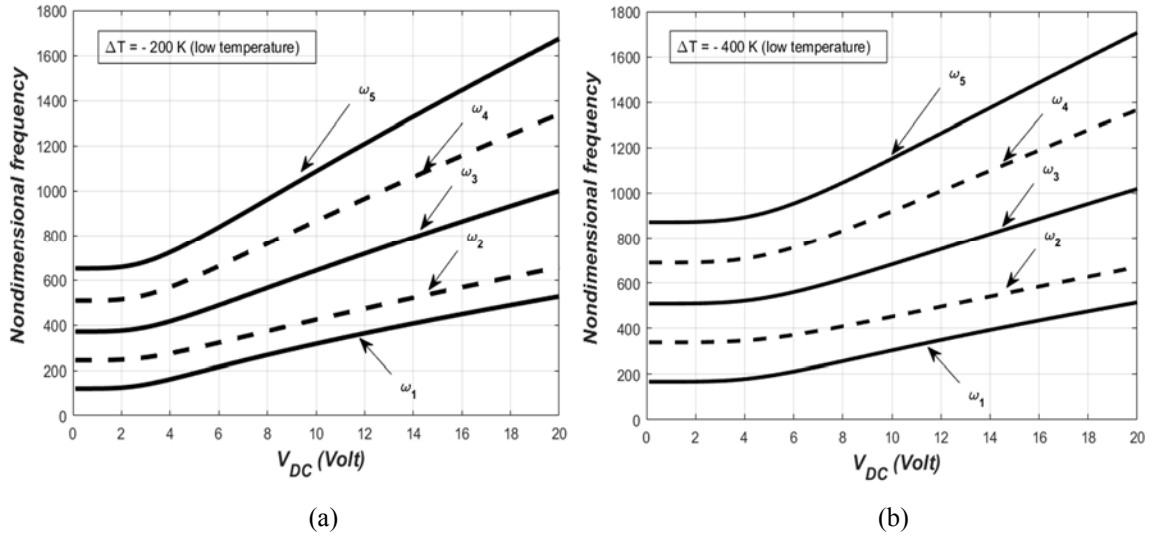


Figure 5.16: Variation of the first five nondimensional in-plane natural frequencies with the DC load, for a straight CNT ($b_0 = 0$ nm) of case 8 from Table 4.2 assuming a strain gradient theory with $l = 1.0$ nm, and for (a) $\Delta T_{low} = -200$ K , and (b) $\Delta T_{low} = -400$ K .

CHAPTER 6

DYNAMIC ANALYSIS

In this chapter, we propose to investigate the dynamic response of the doubly clamped CNT-based nano-resonator under DC static and AC harmonic loads. We prescribe a ROM using the first (fundamental) in-plane mode-shape then used it to integrate numerically the ordinary differential equation of motion in the time domain. By using a long time integration technique while assuming a 4th order Runge-Kutta method, we consider very small gate voltage to investigate the dynamic responses of the CNT, ensuring converged results without much hysteretic and nonlinear behaviors. The effects of alternating current gate voltage, size scale dependent parameters, and quality factor will be then analyzed and discussed.

6.1. Reduced Order Model Prescription for Dynamic Analysis

6.1.1. Classical continuum theory

By considering classical continuum theory, the equation of motion considering first in-plane mode shape can be written as [95]:

$$u_1(\hat{t}) \frac{\partial^4 \phi_1(\hat{x})}{\partial \hat{x}^4} + \phi_1(x) \frac{\partial^2 u_1(\hat{t})}{\partial \hat{t}^2} + C \phi_1(\hat{x}) \frac{\partial u_1(\hat{t})}{\partial \hat{t}} = \alpha_1 \left(u_1^3(\hat{t}) \int_0^L \left(\frac{\partial \phi_1(\hat{x})}{\partial \hat{x}} \right)^2 d\hat{x} \right) \frac{\partial^2 \phi_1(\hat{x})}{\partial \hat{x}^2} + \alpha_2 F_e(\hat{x}, \hat{t}), \quad (6.1)$$

The normalized electrostatic force term $F_e(\hat{x}, \hat{t})$ in Eq. (6.1) is expressed as:

$$F_e(\hat{x}, \hat{t}) = \frac{(V_{DC} + V_{AC} \cos(\hat{\Omega}\hat{t}))^2}{\sqrt{(1-u_1(\hat{t})\phi_1(\hat{x}))(1-u_1(\hat{t})\phi_1(\hat{x})+2\hat{r})} \left(\cosh^{-1} \left(1 + \frac{1-u_1(\hat{t})\phi_1(\hat{x})}{\hat{r}} \right) \right)^2, \quad (6.2)$$

where $u_1(t)$ is first in-plane modal coordinate, α_1 and α_2 are given by Eq. (2.9). Next, one apply the orthogonality condition of the mode shape $\phi_1(\hat{x})$, the equation can be written as [95]:

$$\begin{aligned} u_1(\hat{t}) \int_0^1 \frac{\partial^4 \phi_1}{\partial \hat{x}^4} \phi_1 d\hat{x} + \frac{\partial^2 u_1(\hat{t})}{\partial \hat{t}^2} \int_0^1 \phi_1 \phi_1 d\hat{x} + \hat{C}_{classic} \frac{\partial u_1(\hat{t})}{\partial \hat{t}} \int_0^1 \phi_1 \phi_1 d\hat{x} = \\ = \alpha_1 u_1^3(\hat{t}) \int_0^1 \left(\int_0^1 \left(\frac{\partial \phi_1}{\partial \hat{x}} \right)^2 d\hat{x} \right) \frac{\partial^2 \phi_1}{\partial \hat{x}^2} \phi_1 d\hat{x} + \int_0^1 \alpha_2 F_e(\hat{x}, \hat{t}) \phi_1 d\hat{x}, \end{aligned} \quad (6.3)$$

Eq. (6.3) can be re-written as:

$$\begin{aligned} \ddot{u}_1(\hat{t}) + \hat{C}_{classic} \dot{u}_1(\hat{t}) + u_1(\hat{t})\Gamma = \alpha_1 u_1^3(\hat{t})\Pi + \\ + \int_0^1 \frac{\alpha_2 (V_{DC} + V_{AC} \cos(\hat{\Omega}\hat{t}))^2}{\sqrt{(1-u_1(\hat{t})\phi_1(\hat{x}))(1-u_1(\hat{t})\phi_1(\hat{x})+2\hat{r})} \left(\cosh^{-1} \left(1 + \frac{1-u_1(\hat{t})\phi_1(\hat{x})}{\hat{r}} \right) \right)^2} \phi_1(\hat{x}) d\hat{x}, \end{aligned} \quad (6.4)$$

where,

$$\Gamma = \int_0^1 \frac{\partial^4 \phi_1}{\partial \hat{x}^4} \phi_1 d\hat{x}, \quad (6.5)$$

$$\Pi = \left[\int_0^1 \left(\frac{\partial \phi_1}{\partial \hat{x}} \right)^2 d\hat{x} \right] \left[\int_0^1 \left(\frac{\partial^2 \phi_1}{\partial \hat{x}^2} \phi_1 \right) d\hat{x} \right] \quad (6.6)$$

$$C = \rho A \omega_n / Q, \quad \hat{C}_{classic} = C \frac{L^4}{EIT_{classic}}, \quad \hat{\Omega} = \frac{\Omega}{\omega_n}, \quad (6.7)$$

And where, Q is the quality factor of the resonator, C is the damping coefficient, ρ is mass density, ω_n is the natural frequency, $\hat{\Omega}$ is the AC harmonic load frequency, and $T_{classic}$ is given by Eq. (2.9).

Next, by assuming the state space variable,

$$\begin{bmatrix} x_1 \\ x_2 \end{bmatrix} = \begin{bmatrix} u_1 \\ \dot{u}_1 \end{bmatrix} \quad (6.8)$$

One substitutes Eq. (6.8) into Eq. (6.4),

$$\begin{aligned} \dot{u}_1 &= x_2, \\ \ddot{u}_1 &= -x_1 \Gamma - C x_2 + \alpha_1 x_1^3 \Pi + \int_0^1 \frac{\alpha_2 (V_{DC} + V_{AC} \cos(\hat{\Omega} \hat{t}))^2}{\sqrt{(1-x_1 \phi_1)(1-x_1 \phi_1 + 2\hat{r})} \left(\cosh^{-1} \left(1 + \frac{1-x_1 \phi_1}{\hat{r}} \right) \right)^2} \phi_1 d\hat{x}, \end{aligned} \quad (6.9)$$

6.1.2. Strain gradient theory

One assumes $\hat{w}(\hat{x}, \hat{t}) \approx q_1(\hat{t}) \phi_1(\hat{x})$, where $q_1(\hat{t})$ represent the first in-plane modal coordinate and $\phi_1(\hat{x})$ is the first in-plane mode shape. Next, by considering strain gradient theory, the equation of motion considering first in-plane mode shape can be written as:

$$\beta_0 q_1 \phi_1^{vi} + q_1 \phi_1^{iv} + \ddot{q}_1 \phi_1 + \tilde{C} q_1' \phi_1 = \beta_1 q_1^3 \left(\int_0^1 (\phi_1')^2 d\hat{x} \right) \phi_1'' + \beta_3 F_e(\hat{x}, \hat{t}), \quad (6.10)$$

where, β_0 , β_1 , β_3 are given by Eq. (3.36), and the electrostatic load is given by:

$$\begin{aligned} F_e(\hat{x}, \hat{t}) &= \frac{(V_{DC} + V_{AC} \cos(\hat{\Omega} \hat{t}))^2}{\sqrt{(1-q_1 \phi_1)(1-q_1 \phi_1 + 2\hat{r})} \left(\cos^{-1} \left(1 + \frac{1-q_1 \phi_1}{\hat{r}} \right) \right)^2}, \\ C &= \rho A \omega_n / Q; \quad \hat{C} = C \frac{L^4}{EIT}, \end{aligned} \quad (6.11)$$

here, T is given by $T = \sqrt{\frac{\rho AL^4}{P}}$ and P is given by Eq. (3.19).

Next, by applying the orthogonality condition of the mode shape $\phi_1(x)$, the equation can be re-written as:

$$\beta_0 q_1 \int_0^1 (\phi_1^{vi} \phi_1) d\hat{x} + q_1 \int_0^1 (\phi_1^{iv} \phi_1) d\hat{x} + \ddot{q}_1 \int_0^1 (\phi_1 \phi_1) d\hat{x} + \hat{C} \dot{q}_1 \int_0^1 \phi_1 \phi_1 d\hat{x} = \int_0^1 \left\{ \beta_1 q_1^3 \left(\int_0^1 (\phi_1')^2 d\hat{x} \right) \phi_1'' \phi_1 \right\} d\hat{x} + \beta_3 \int_0^1 (F_e(\hat{x}, \hat{t}) \phi_1) d\hat{x}, \quad (6.12)$$

Eq. (6.12) can be simplified as:

$$\ddot{q}_1(\hat{t}) = -\hat{C} \dot{q}_1 - (\beta_0 \Gamma_1 + \Gamma_2) q_1 + \beta_1 \Pi_1 \Pi_2 q_1^3 + \beta_3 \int_0^1 (F_e(\hat{x}, \hat{t}) \phi_1) d\hat{x}, \quad (6.13)$$

where,

$$\Gamma_1 = \int_0^1 (\phi_1^{vi} \phi_1) d\hat{x}, \quad \Gamma_2 = \int_0^1 (\phi_1^{iv} \phi_1) d\hat{x}, \quad \Pi_1 = \int_0^1 (\phi_1')^2 d\hat{x}, \quad \Pi_2 = \int_0^1 \phi_1'' \phi_1 d\hat{x} \quad (6.14)$$

Finally, one assumes the state space variable,

$$\begin{bmatrix} x_1 \\ x_2 \end{bmatrix} = \begin{bmatrix} q_1 \\ \dot{q}_1 \end{bmatrix} \quad (6.15)$$

We substitute Eq. (6.15) into Eqs. (6.13) and (6.14), hence, one obtains the one mode normalized equation of motion in the state space form.

$$\begin{aligned} \dot{q}_1 &= x_2, \\ \ddot{q}_1(\hat{t}) &= -(\beta_0 \Gamma_1 + \Gamma_2) x_1 - \hat{C}_v x_2 + \beta_1 \Pi_1 \Pi_2 x_1^3(\hat{t}) + \beta_3 \int_0^1 (F_e(\hat{x}, \hat{t}) \phi_1) dx, \end{aligned} \quad (6.16)$$

where,

$$F_e = \frac{\left(V_{dc} + V_{ac} \cos(\hat{\Omega}t)\right)^2}{\sqrt{(1-x_1\phi_1)(1-x_1\phi_1 + 2\hat{r})} \left(\cos^{-1}\left(1 + \frac{1-x_1\phi_1}{\hat{r}}\right)\right)^2} \quad (6.17)$$

6.2. Dynamic Response

6.2.1. The size scale dependent effect

In this section, we propose to investigate the effects of the size scale dependent parameters to the dynamical behavior of the doubly-clamped CNT-based nanoresonator. The CNTs of cases 1, 3 and 8 were considered in the simulation to study the size dependent effect on the dynamical behavior of the doubly clamped CNT based nanobeam. We also assume different size scale dependent parameters as follows: $l = 0$ which represents the classical continuum theory, $l = 1.0 \text{ nm}$, $l = 1.25 \text{ nm}$, and $l = 1.5 \text{ nm}$ in the below simulations.

Next, we use the 4th Runge-Kutta method to get the dynamic response of the straight CNT under static DC and harmonic AC harmonic load. Figure 6.1 shows the dynamic response of case number 1 of Table 4.2 subjected to a static 2 Volt DC load superimposed to a dynamic 2 Volt AC harmonic load with forcing frequency near the CNT-based nanobeam fundamental frequency ($\Omega \approx 22$). In the same figure, we are assuming a quality factor of $Q = 100$, and zero initial conditions for the modal coordinates. The damping coefficient in these simulations is related to the quality factor Q as given by Eq. (6.11). One can observe that the CNT time history dynamic response at its mid-point is reaching the steady-state response for values of normalized time greater than 50.

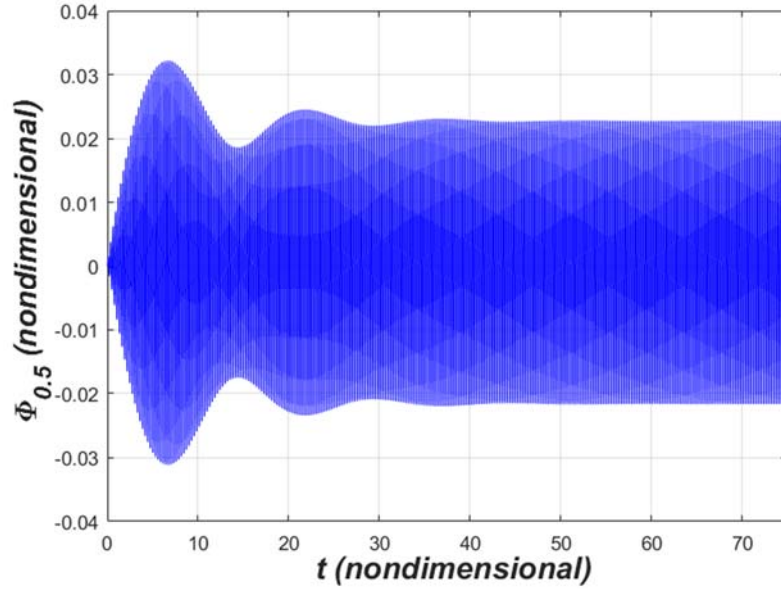


Figure 6.1: Time history curve of the maximum dynamic response of the CNT of case 1 of Table 4.2 at a forcing frequency of $\Omega \approx 22$, forcing amplitude of $V_{DC} = V_{AC} = 2$ Volt, a SGT parameter of $l = 1$ nm , and a quality factor of $Q = 100$.

Then, we develop an algorithm to compute the frequency response curves displaying the CNT based nanobeam converged dynamical solutions while varying the AC harmonic input excitation frequency as denoted by Ω . The values of the normalizing frequency ω_n are obtained from the results of the linear eigenvalue problem which mainly depend on the value of static DC load. Figure 6.2 shows the variation of the CNT of case 1 of Table 4.2 mid-point maximum dynamic values for various AC load frequency ranging from 20 to 30, and for various size scale dependent parameters. The figure demonstrates that in all cases, the CNT dynamic response exhibit a hardening behavior where the resonant frequency is greater than the natural frequency of the excited structure. Moreover, as the strain gradient parameters tend to increase, the resonance frequency of the CNT increase as well. In fact, these results infer a consistent consequence of the previously discussed conclusion of the linearized eigenvalue problem

that the strain gradient theory is by all means altering the rigidity of the CNT-based nanobeam by making it stiffer.

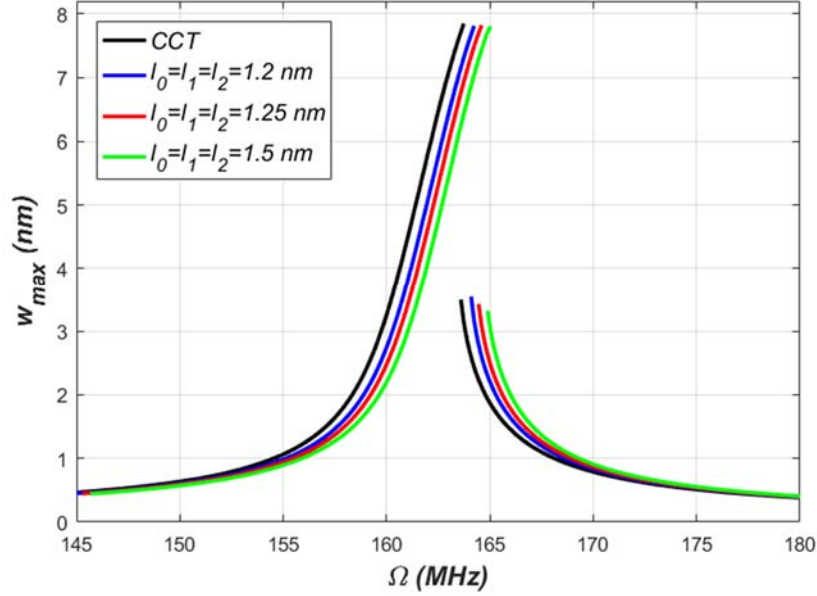


Figure 6.2: Frequency-response curve of the CNT of case 1 of Table 4.2 for various strain gradient parameters values, $V_{DC}=V_{AC}=2$ Volt, and a quality factor of $Q = 100$.

As previously identified from the linearized eigenvalue problem simulations, the strain gradient effect is more prominent for CNT with smaller radii, consequently we propose next to simulate the CNT dynamic responses of the case 3 and 8 of Table 4.2, Figures 6.3 and 6.4 respectively. Both figures are illustrating similar frequency response curves shapes all demonstrating hardening behaviors with increasing resonance frequencies. Indeed, through comparing all reproduced frequency response curves, Figures 6.2-6.4, we can deduce that the discrepancies between the results when assuming classical continuum mechanics as compared to those obtained using the strain gradient theory are becoming higher when the CNT radius is decreased. Moreover, the resonance frequency shift is more significant as the CNT radii are reduced to smaller values. It can be concluded that the strain gradient effect is definitely more evident when the

geometrical dimensions of the CNT are closer to the strain gradient parameters. These results again show the capability of the strain gradient theory to capture the size scale dependent effect especially while considering very small CNT structural geometry. Finally, it can be comprehended from Figure 6.4 that the strain gradient effects are not altering only the location of the resonant frequency, but also change the CNT dynamic response through reducing its maximum dynamic oscillation, therefore stiffening its overall structural behavior. This significant outcome may explain one of the causes behind the discrepancies reported in the literature when comparing the results of classical continuum mechanics to experimental data for CNTs driven harmonically at resonance near their fundamental modes.

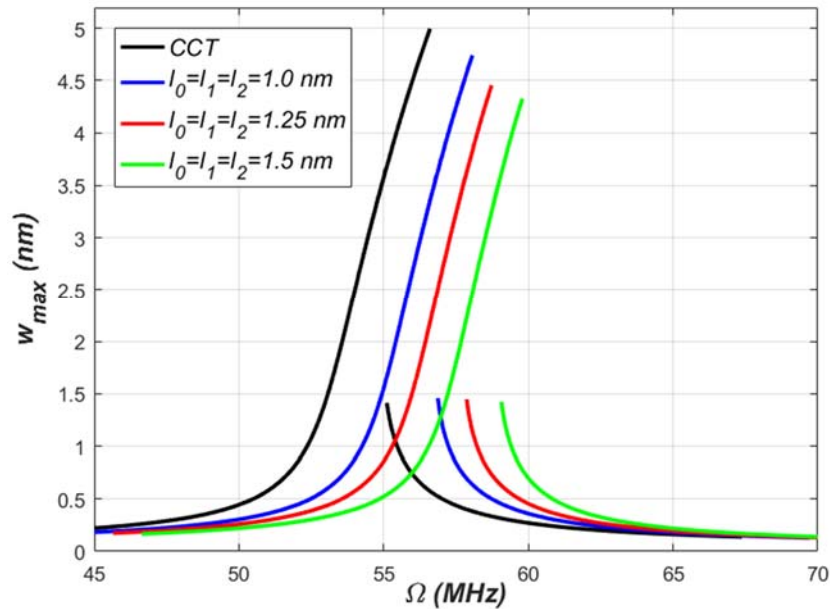


Figure 6.3: Frequency-response curve of the CNT of case 3 of Table 4.2 for various strain gradient parameters values, $V_{DC} = V_{AC} = 0.25$ Volt, and a quality factor of $Q = 100$.

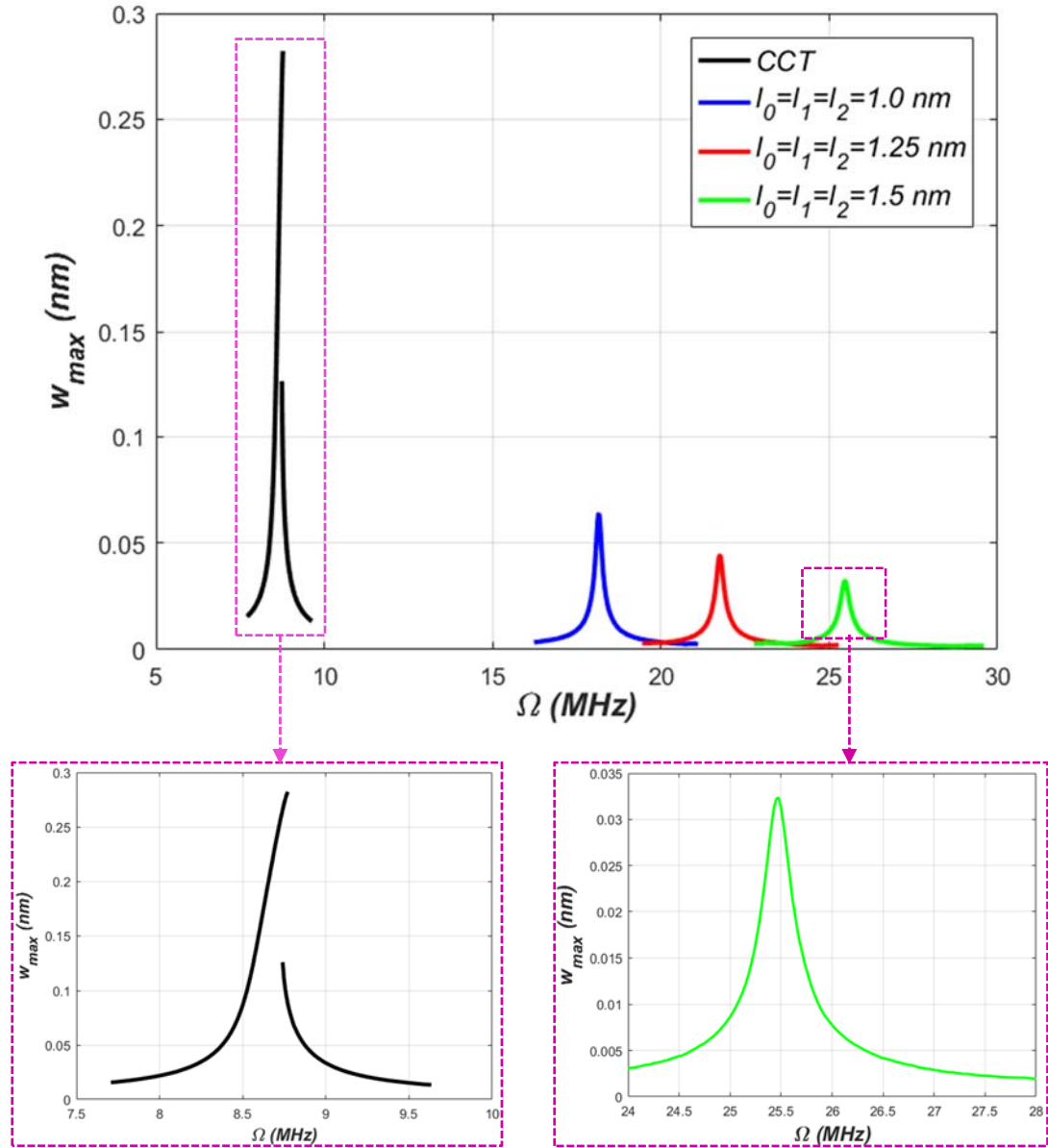


Figure 6.4: Frequency-response curve of the CNT of case 8 of Table 4.2 for various strain gradient parameters values, $V_{DC}=10$ milliVolt, $V_{AC}=2$ milliVolt, and a quality factor of $Q = 100$.

6.2.2. The effect of alternating current gate voltage (V_{AC})

Figures 6.5 and Figure 6.6 show the effect of applied AC voltage on the oscillation amplitude and resonance frequency. In these simulations, cases 1 and 3 of Table 4.2 are considered to observe the effect of V_{AC} while assuming a quality factor of $Q = 100$. The

results indicate that increasing the V_{AC} tends to increase the hardening type of nonlinearity and the oscillation amplitudes of the resonator. The resonance frequencies are also slightly shifted as the increased of V_{AC} .

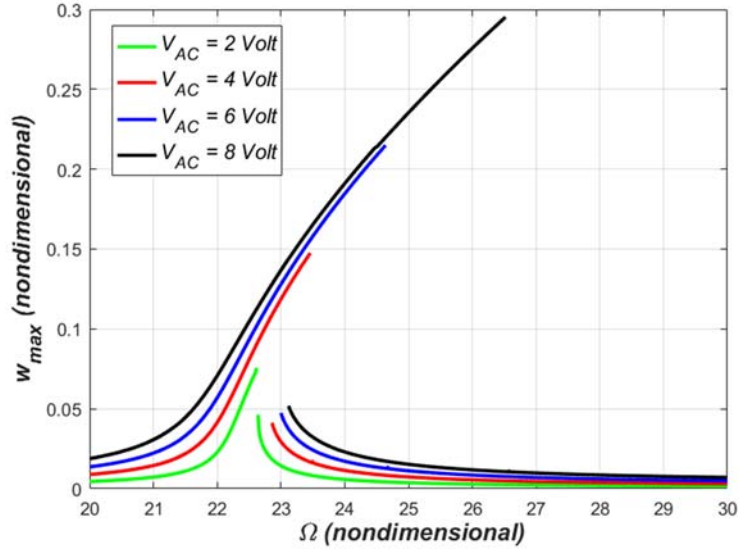


Figure 6.5: Frequency-response curve for case 1 of Table 4.2 showing the effect of V_{AC} and considering a quality factor of $Q = 100$ and $V_{DC} = 2$ Volt and assuming SGT parameter of $l = 0.8$ nm.

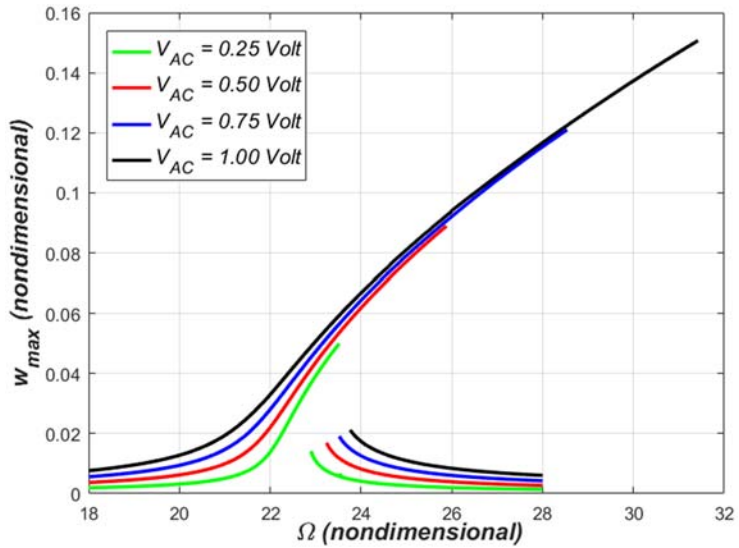


Figure 6.6: Frequency-response curve for case 3 of Table 4.2 showing the effect of V_{AC} and considering a quality factor of $Q = 100$ and $V_{DC} = 0.25$ Volt and assuming SGT parameter of $l = 0.8$ nm.

6.2.3. The effect of quality factor (Q)

Figure 6.7 shows the amplitudes versus excitation frequencies for four different quality factors for case 3 of Table 4.2. In order to observe the quality factor effect to dynamical response, $V_{AC} = 0.25 \text{ Volt}$ and $V_{DC} = 1 \text{ Volt}$ are selected such that the vibrations occur in the nonlinear vibration regime. It is clearly observed that the quality factor effect tends to decrease the amplitude of the vibrations as well as enlarge the frequency bandwidth. The hardening type nonlinearity effect is also intervened while decreasing the quality factor. One can observe that the energy losses are increases for CNT with lower quality factor as indicated by the decreases of oscillation amplitudes which mean that the solutions are converged faster. The resonators with high quality factor have low damping ratio, hence the CNT can vibrate longer. High quality factor is favorable characteristic in the design of CNT-based NEMS resonators.

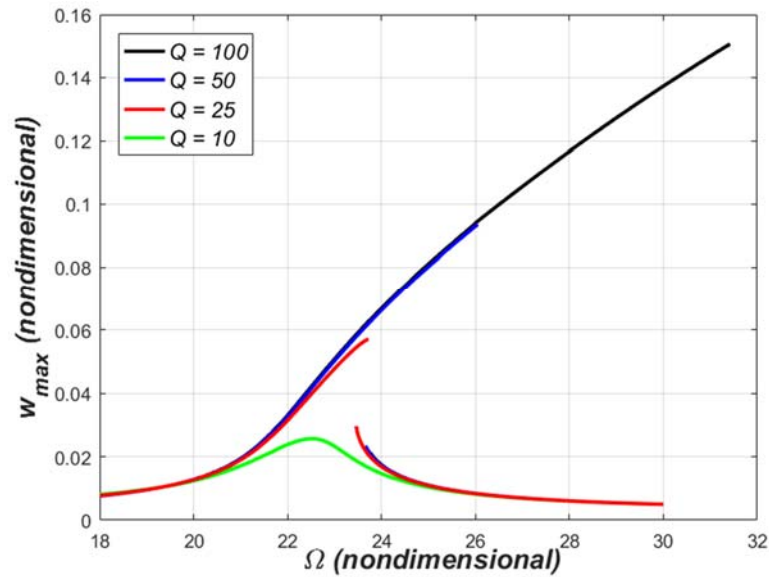


Figure 6.7: The effect of quality factor (Q) on the frequency response curve for case 3 of Table 4.2, considering the voltage values of $V_{AC} = 0.25 \text{ Volt}$ and $V_{DC} = 1 \text{ Volt}$ and assuming SGT parameter of $l = 0.8 \text{ nm}$.

CHAPTER 7

CONCLUSIONS AND FUTURE RECOMMENDATIONS

7.1. Conclusions

Based on the strain gradient deformation beam theory, a size-dependent nanobeam model, which assumes three higher-order material size scale dependent parameters related to the material nanostructures, is developed to investigate the static and free vibration of a CNT based nanobeam. The higher-order governing equations, taking into account the geometric nonlinearities due to von Karman nonlinear strains and slack effect, temperature gradient and their respective boundary conditions were derived using the Hamilton principle. The Galerkin based reduced order modeling along with the Jacobian method were both employed to analyze the variation of the CNT static deflection and natural frequencies of the with the DC load as well as its slack level. The effects of the size scale dependent parameters, the slack level, the CNT length-to-radius ratio, and temperature gradient characteristics were all discussed.

A static analysis was carried out through varying the SGT size scale dependent parameters as well as the temperature gradient. In addition, the natural frequencies of straight and slacked CNT based nanobeam were investigated. From both static and free vibration analysis, it is concluded that the size effect on the static and free vibration characteristics of the CNT based nanobeam is significant when the CNT radius is smaller

than the length scale parameters especially in the low gate voltage regime. The CNT frequencies are significantly varying when the size scale dependent parameters are changing. A stiffening effect, mainly due to the strain gradient effects, were observed to be significant at the low temperature gradient regime. Other outcomes showed also the a CNT assuming higher temperature gradient is showing a similar static behavior as a slacked CNT as was previously reported in [24].

A substantial conclusion of this study is that the natural frequencies variations assuming low gate voltages were showing remarkable discrepancies between classical theory and the strain gradient theory, which therefore should not be ignored in analyzing nanoscale structures. In addition, the effect of the size scale dependent parameters and temperature gradients on the modes veering and modes crossing occurrence of slacked CNT based nanobeam was shown to be prominent in altering these modal interactions. Therefore, assuming a strain gradient theory indicated a decrease in the effective slack effect on the vibrational behavior of initially curved CNT.

In addition, the temperature gradient effects were also shown to play significant role in the modes veering and modes crossing occurrences. Computed natural frequency dispersion curves showed that for cases assuming higher temperature gradients are significantly affecting the existence of modes veering and modes crossing. On the other hand, when assuming cases with low temperature gradients, the CNT frequency dispersions curved were not showing any single possibility of modes veering and modes crossing. The model also confirmed the stiffening effect behavior while operating the resonator in a low temperature gradient conditions. Succeeding the free-vibration analysis, a forced vibration analysis under low gate actuation was conducted to

investigate the size scale dependent effect to the dynamical behavior of the CNT based nano-resonator. Three different CNT geometrical parameters were assumed in order to study the size scale effect. Results showed that the discrepancies between the CNT dynamic responses obtained when using the classical continuum mechanics and those when assuming the strain gradient model are becoming more significant while assuming smaller CNT geometries. The obtained results allow better understanding of the nonlinear behavior of CNT based nanoresonators and can guide NEMS engineers accordingly in the design consideration stages.

7.2. Future Recommendations

The below listed future works are recommended as further extension of this current work:

1. The velocity gradient effect can be added to the kinetic energy, somehow it will be useful to capture a unique behavior in the dynamic regime.
2. A thorough dynamic analysis should be conducted using more robust technique such as shooting technique and method of multiple scale to capture the nonlinear effects and therefore gaining more accuracy in getting the CNT resonant frequencies at high DC and AC amplitudes.
3. A global dynamic analysis can be carried out in order to study the size dependent and temperature gradient effect in the nonlinear regime.
4. A systematic procedure should be developed in order to estimate the specific value of size scale dependent parameters by conducting experimental work using the comprehensive method and accurate measurement tools.

Appendix

Doubly-clamped Slacked CNT-based Nanobeam Equation of Motion Derivation Based on Strain Gradient Theory

Based on Lam et al (2003), the strain energy density U of a linear elastic continuum for the entire region of \forall is given as a function of the symmetric strain tensor ε_{ij} , the dilation gradient vector γ_i , the deviatoric stretch gradient tensor η_{ijk}^1 and the symmetric rotation gradient tensor χ_{ij} , as follows:

$$U = \frac{1}{2} \int_{\forall} (\boldsymbol{\sigma}_{pq} \boldsymbol{\varepsilon}_{pq} + \mathbf{p}_p \boldsymbol{\gamma}_p + \boldsymbol{\tau}_{pqr}^1 \boldsymbol{\eta}_{pqr}^1 + \mathbf{m}_{pq} \boldsymbol{\chi}_{pq}) dV \quad (\text{A.1})$$

where $\boldsymbol{\sigma}_{pq}$ represents the Cauchy stress tensor, and \mathbf{p}_p , $\boldsymbol{\tau}_{pqr}^1$ and \mathbf{m}_{pq} are the higher-order stress tensors corresponding to the higher-order tensor terms. The remaining parameters in Eq. (A.1) are summarized below:

$$\varepsilon_{pq} = \frac{1}{2} (u_{p,q} + u_{q,p}), \quad (\text{A.2})$$

$$\gamma_i = \varepsilon_{mm,i}, \quad (\text{A.3})$$

$$\begin{aligned} \eta_{pqr}^1 = & \frac{1}{3} (\varepsilon_{qr,p} + \varepsilon_{rp,q} + \varepsilon_{pq,r}) - \frac{1}{15} \delta_{pq} (\varepsilon_{ss,r} + 2\varepsilon_{sr,s}) + \\ & - \frac{1}{15} [\delta_{qr} (\varepsilon_{ss,p} + 2\varepsilon_{sp,s}) + \delta_{rp} (\varepsilon_{ss,q} + 2\varepsilon_{sq,q})], \end{aligned} \quad (\text{A.4})$$

$$\chi_{pq} = \frac{1}{2} (\theta_{p,q} + \theta_{q,p}), \quad (\text{A.5})$$

$$\theta_p = \frac{1}{2}(\text{curl}(u))_p, \quad (\text{A.6})$$

$$\sigma_{pq} = \lambda[\varepsilon]^T \delta_{pq} + 2G\varepsilon_{pq}, \quad (\text{A.7})$$

$$p_p = 2Gl_0^2\gamma_p, \quad (\text{A.8})$$

$$\tau_{pqr}^1 = 2Gl_1^2\eta_{pqr}^1, \quad (\text{A.9})$$

$$m_{pq} = 2Gl_2^2\chi_{pq}, \quad (\text{A.10})$$

$$\lambda = \frac{\nu E}{(1+\nu)(1-2\nu)}, \quad (\text{A.11})$$

$$G = \frac{E}{2(1+\nu)}, \quad (\text{A.12})$$

where u_p is the CNT axial displacement, θ_p is the rotation vector, γ_p is the dilatation gradient vector, δ_{pq} is the Kronecker's delta operator, λ and G are the Lamé constants, respectively. The size scale dependent parameters noted above as l_0 , l_1 , and l_2 are the dilatation, the deviatoric stretch, and the rotation gradients, respectively.

By assuming an Euler-Bernoulli beam model, the carbon nanotube displacement field can be expressed as:

$$u_1 = u(x, t) - z \left\{ \frac{\partial w(x, t)}{\partial x} - \frac{dw_0(x)}{dx} \right\}; u_2 = 0; u_3 = w(x, t) - w_0(x), \quad (\text{A.13})$$

Considering the von-Karman nonlinearity of the clamped-clamped CNT for mid-plane stretching effect, the first order nonlinear strain-displacement relations for an initially curved beam can be written as follows [62, 87, 101]:

$$\varepsilon_{11} = \varepsilon_{11}^0 + z\kappa_{11}, \quad (\text{A.14})$$

$$\varepsilon_{11}^0 = \frac{\partial u}{\partial x} + \frac{1}{2} \left(\frac{\partial w(x,t)}{\partial x} \right)^2 - \frac{1}{2} \left(\frac{dw_0(x)}{dx} \right)^2; \quad \kappa_{11} = - \left(\frac{\partial^2 w(x,t)}{\partial x^2} - \frac{d^2 w_0(x)}{dx^2} \right), \quad (\text{A.15})$$

$$\varepsilon_{11} = \frac{\partial u}{\partial x} + \frac{1}{2} \left(\frac{\partial w(x,t)}{\partial x} \right)^2 - \frac{1}{2} \left(\frac{dw_0(x)}{dx} \right)^2 - z \left(\frac{\partial^2 w(x,t)}{\partial x^2} - \frac{d^2 w_0(x)}{dx^2} \right), \quad (\text{A.16})$$

Evaluating the higher strain terms as function of the beam displacement components, we are left with the following expressions:

$$\gamma_1 = \frac{\partial \varepsilon_{11}}{\partial x} = \frac{\partial^2 u}{\partial x^2} + \frac{\partial w}{\partial x} \frac{\partial^2 w}{\partial x^2} - \frac{dw_0}{dx} \frac{d^2 w_0}{dx^2} - \left(z \frac{\partial^3 w}{\partial x^3} - \frac{d^3 w_0}{dx^3} \right), \quad (\text{A.17})$$

$$\gamma_3 = \frac{\partial \varepsilon_{11}}{\partial z} = - \left(\frac{\partial^2 w}{\partial x^2} - \frac{d^2 w_0}{dx^2} \right), \quad (\text{A.18})$$

$$\begin{aligned} \chi_{12} = \chi_{21} &= \frac{1}{2} \left(\frac{\partial}{\partial y} \left(\frac{1}{2} (\nabla \times \mathbf{u})_1 \right) + \frac{\partial}{\partial x} \left(\frac{1}{2} (\nabla \times \mathbf{u})_2 \right) \right) \\ &= \frac{1}{2} \left\{ \frac{\partial}{\partial y} \left(\frac{1}{2} \frac{\partial u_3}{\partial y} - \frac{1}{2} \frac{\partial u_2}{\partial z} \right) + \frac{\partial}{\partial x} \left(\frac{1}{2} \frac{\partial u_3}{\partial x} - \frac{1}{2} \frac{\partial u_1}{\partial z} \right) \right\} = - \left(\frac{\partial^2 w}{\partial x^2} - \frac{d^2 w_0}{dx^2} \right), \end{aligned} \quad (\text{A.19})$$

Expanding the indices of Eq (A.4) and Eqs, (A.8)-(A.10), while imposing a non-zero deviatoric stretch gradient tensor components, we are left with the following non-zero terms:

$$\eta_{111}^1 = \frac{2}{5} \left(\frac{\partial^2 u}{\partial x^2} + \frac{\partial w}{\partial x} \frac{\partial^2 w}{\partial x^2} - \frac{dw_0}{dx} \frac{d^2 w_0}{dx^2} - z \left(\frac{\partial^3 w}{\partial x^3} - \frac{d^3 w_0}{dx^3} \right) \right), \quad (\text{A.20})$$

$$\eta_{113}^1 = \eta_{311}^1 = \eta_{131}^1 = - \frac{4}{15} \left(\frac{\partial^2 w}{\partial x^2} - \frac{d^2 w_0}{dx^2} \right), \quad (\text{A.21})$$

$$\eta_{122}^1 = \eta_{133}^1 = \eta_{212}^1 = \eta_{221}^1 = \eta_{313}^1 = \eta_{331}^1 = - \frac{1}{5} \left(\frac{\partial^2 u}{\partial x^2} + \frac{\partial w}{\partial x} \frac{\partial^2 w}{\partial x^2} - \frac{dw_0}{dx} \frac{d^2 w_0}{dx^2} - z \left(\frac{\partial^3 w}{\partial x^3} - \frac{d^3 w_0}{dx^3} \right) \right), \quad (\text{A.22})$$

$$\eta_{223}^1 = \eta_{232}^1 = \eta_{332}^1 = \frac{1}{15} \left(\frac{\partial^2 w}{\partial x^2} - \frac{d^2 w_0}{dx^2} \right); \quad \eta_{333}^1 = \frac{1}{5} \left(\frac{\partial^2 w}{\partial x^2} - \frac{d^2 w_0}{dx^2} \right), \quad (\text{A.23})$$

$$p_1 = 2l_0^2 G \gamma_1; \quad p_3 = 2l_0^2 G \gamma_3, \quad (\text{A.24})$$

$$m_{12} = m_{21} = 2Gl_2^2 \chi_{12} = 2Gl_2^2 \chi_{21}, \quad (\text{A.25})$$

$$\tau_{111}^1 = 2Gl_1^2 \eta_{111}^1, \quad (\text{A.26})$$

$$\tau_{113}^1 = \tau_{131}^1 = \tau_{311}^1 = -\frac{8}{15} Gl_1^2 \left(\frac{\partial^2 w}{\partial x^2} - \frac{d^2 w_0}{dx^2} \right), \quad (\text{A.27})$$

$$\tau_{122}^1 = \tau_{133}^1 = \tau_{212}^1 = \tau_{221}^1 = \tau_{313}^1 = \tau_{331}^1 = -\frac{2}{5} Gl_1^2 \left(\frac{\partial^2 u}{\partial x^2} + \frac{\partial w}{\partial x} \frac{\partial^2 w}{\partial x^2} - \frac{dw_0}{dx} \frac{d^2 w_0}{dx^2} - z \left(\frac{\partial^3 w}{\partial x^3} - \frac{d^3 w_0}{dx^3} \right) \right), \quad (\text{A.28})$$

$$\tau_{223}^1 = \tau_{232}^1 = \tau_{322}^1 = -\frac{2}{15} Gl_1^2 \left(\frac{\partial^2 w}{\partial x^2} - \frac{d^2 w_0}{dx^2} \right), \quad (\text{A.29})$$

$$\tau_{333}^1 = 2Gl_1^2 \eta_{333}^1, \quad (\text{A.30})$$

Then, substituting the all above expressions into the strain energy density function, Eq.

(A.1).

$$U = \frac{1}{2} \int_{\forall} \left(\begin{aligned} & \sigma_{11} \varepsilon_{11} + p_1 \gamma_1 + p_3 \gamma_3 + \tau_{111}^1 \eta_{111}^1 + \tau_{113}^1 \eta_{113}^1 + \tau_{122}^1 \eta_{122}^1 + \tau_{131}^1 \eta_{131}^1 + \tau_{133}^1 \eta_{133}^1 + \tau_{212}^1 \eta_{212}^1 + \dots \\ & + \tau_{221}^1 \eta_{221}^1 + \tau_{223}^1 \eta_{223}^1 + \tau_{232}^1 \eta_{232}^1 + \tau_{311}^1 \eta_{311}^1 + \tau_{313}^1 \eta_{313}^1 + \tau_{331}^1 \eta_{331}^1 + \tau_{332}^1 \eta_{332}^1 + \tau_{333}^1 \eta_{333}^1 + \dots \\ & + m_{12} \chi_{12} + m_{21} \chi_{21} \end{aligned} \right) dv \quad (\text{A.31})$$

$$U = \frac{1}{2} \int_{\forall} \left(\begin{aligned} & E \left(\frac{\partial u}{\partial x} + \frac{1}{2} \left(\frac{\partial w}{\partial x} \right)^2 - \frac{1}{2} \left(\frac{dw_0}{dx} \right)^2 - z \left(\frac{\partial^2 w}{\partial x^2} - \frac{d^2 w_0}{dx^2} \right) \right)^2 + \dots \\ & + 2l_0^2 G \left(\frac{\partial^2 u}{\partial x^2} + \frac{\partial w}{\partial x} \frac{\partial^2 w}{\partial x^2} - \frac{dw_0}{dx} \frac{d^2 w_0}{dx^2} - z \left(\frac{\partial^3 w}{\partial x^3} - \frac{d^3 w_0}{dx^3} \right) \right)^2 + \dots \\ & + 2l_0^2 G \left(\frac{\partial^2 w}{\partial x^2} - \frac{d^2 w_0}{dx^2} \right)^2 + \frac{4}{5} l_1^2 G \left(\frac{\partial^2 u}{\partial x^2} + \frac{\partial w}{\partial x} \frac{\partial^2 w}{\partial x^2} - \frac{dw_0}{dx} \frac{d^2 w_0}{dx^2} - z \left(\frac{\partial^3 w}{\partial x^3} - \frac{d^3 w_0}{dx^3} \right) \right)^2 + \dots \\ & + \frac{8}{12} l_1^2 G \left(\frac{\partial^2 w}{\partial x^2} - \frac{d^2 w_0}{dx^2} \right)^2 + l_2^2 G \left(\frac{\partial^2 w}{\partial x^2} - \frac{d^2 w_0}{dx^2} \right)^2 \end{aligned} \right) dv \quad (\text{A.32})$$

$$U = \frac{1}{2} \int_{\forall} \left(\begin{aligned} & E \left(\frac{\partial u}{\partial x} + \frac{1}{2} \left(\frac{\partial w}{\partial x} \right)^2 - \frac{1}{2} \left(\frac{dw_0}{dx} \right)^2 - z \left(\frac{\partial^2 w}{\partial x^2} - \frac{d^2 w_0}{dx^2} \right) \right)^2 + \dots \\ & + \left(2l_0^2 + \frac{4}{5} l_1^2 \right) G \left(\frac{\partial^2 u}{\partial x^2} + \frac{\partial w}{\partial x} \frac{\partial^2 w}{\partial x^2} - \frac{dw_0}{dx} \frac{d^2 w_0}{dx^2} - z \left(\frac{\partial^3 w}{\partial x^3} - \frac{d^3 w_0}{dx^3} \right) \right)^2 + \dots \\ & + \left(2l_0^2 + \frac{8}{12} l_1^2 + l_2^2 \right) G \left(\frac{\partial^2 w}{\partial x^2} - \frac{d^2 w_0}{dx^2} \right)^2 + \dots \end{aligned} \right) dv \quad (\text{A.33})$$

$$U = \frac{1}{2} \int_0^L \left(\begin{aligned} & \left(EI_y + GA \left(2l_0^2 + \frac{8}{12} l_1^2 + l_2^2 \right) \right) \left(\frac{\partial^2 w}{\partial x^2} - \frac{d^2 w_0}{dx^2} \right)^2 + GI_y \left(2l_0^2 + \frac{4}{5} l_1^2 \right) \left(\frac{\partial^3 w}{\partial x^3} - \frac{d^3 w_0}{dx^3} \right)^2 + \dots \\ & + EA \left(\frac{\partial u}{\partial x} + \frac{1}{2} \left(\frac{\partial w}{\partial x} \right)^2 - \frac{1}{2} \left(\frac{dw_0}{dx} \right)^2 \right)^2 + GA \left(2l_0^2 + \frac{4}{5} l_1^2 \right) \left(\frac{\partial^2 u}{\partial x^2} + \frac{\partial w}{\partial x} \frac{\partial^2 w}{\partial x^2} - \frac{dw_0}{dx} \frac{d^2 w_0}{dx^2} \right)^2 \end{aligned} \right) dv \quad (\text{A.34})$$

$$U = \frac{1}{2} \int_0^L \left(P \left(\frac{\partial^2 w}{\partial x^2} - \frac{d^2 w_0}{dx^2} \right)^2 + Q ()^2 + EA \left(\frac{\partial u}{\partial x} + \frac{1}{2} \left(\frac{\partial w}{\partial x} \right)^2 - \frac{1}{2} \left(\frac{dw_0}{dx} \right)^2 \right)^2 + \dots \right. \\ \left. + R \left(\frac{\partial^2 u}{\partial x^2} + \frac{\partial w}{\partial x} \frac{\partial^2 w}{\partial x^2} - \frac{dw_0}{dx} \frac{d^2 w_0}{dx^2} \right)^2 \right) dx \quad (\text{A.35})$$

and where the constants P , Q , and R , are defined with the following explicit expressions

$$P = \left(EI_y + GA \left(2l_0^2 + \frac{8}{15} l_1^2 + l_2^2 \right) \right), \quad Q = GI_y \left(2l_0^2 + \frac{4}{5} l_1^2 \right), \quad R = GA \left(2l_0^2 + \frac{4}{5} l_1^2 \right), \quad (\text{A.36})$$

The lengthen scales noted above as l_0 , l_1 , and l_2 are the dilatation, the deviatoric stretch, and the rotation gradients, respectively [32].

$$\delta U = \int_0^L P \left(\frac{\partial^2 w}{\partial x^2} - \frac{d^2 w_0}{dx^2} \right) \delta \left(\frac{\partial^2 w}{\partial x^2} - \frac{d^2 w_0}{dx^2} \right) dx + \int_0^L Q \left(\frac{\partial^3 w}{\partial x^3} - \frac{d^3 w_0}{dx^3} \right) \delta \left(\frac{\partial^3 w}{\partial x^3} - \frac{d^3 w_0}{dx^3} \right) dx + \\ + \int_0^L EA \left(\frac{\partial u}{\partial x} + \frac{1}{2} \left(\frac{\partial w}{\partial x} \right)^2 - \frac{1}{2} \left(\frac{dw_0}{dx} \right)^2 \right) \delta \left(\frac{\partial u}{\partial x} + \frac{1}{2} \left(\frac{\partial w}{\partial x} \right)^2 - \frac{1}{2} \left(\frac{dw_0}{dx} \right)^2 \right) dx + \quad (\text{A.37}) \\ + \int_0^L R \left(\frac{\partial^2 u}{\partial x^2} + \frac{\partial w}{\partial x} \frac{\partial^2 w}{\partial x^2} - \frac{dw_0}{dx} \frac{d^2 w_0}{dx^2} \right) \delta \left(\frac{\partial^2 u}{\partial x^2} + \frac{\partial w}{\partial x} \frac{\partial^2 w}{\partial x^2} - \frac{dw_0}{dx} \frac{d^2 w_0}{dx^2} \right) dx$$

$$\begin{aligned}
\delta U = & P \left(\frac{\partial^2 w}{\partial x^2} - \frac{d^2 w_0}{dx^2} \right) \frac{\partial(\delta w)}{\partial x} \Big|_0^L - P \int_0^L \left(\frac{\partial}{\partial x} \left(\frac{\partial^2 w}{\partial x^2} - \frac{d^2 w_0}{dx^2} \right) \frac{\partial(\delta w)}{\partial x} \right) dx + \\
& + P \int_0^L \left(\left(\frac{\partial^2 w}{\partial x^2} - \frac{d^2 w_0}{dx^2} \right) \frac{d^2(\delta w_0)}{dx^2} \right) dx + Q \left(\frac{\partial^3 w}{\partial x^3} - \frac{d^3 w_0}{dx^3} \right) \frac{\partial^2(\delta w)}{\partial x^2} \Big|_0^L + \\
& - Q \int_0^L \left(\frac{\partial}{\partial x} \left(\frac{\partial^3 w}{\partial x^3} - \frac{d^3 w_0}{dx^3} \right) \frac{\partial^2(\delta w)}{\partial x^2} \right) dx - Q \int_0^L \left(\left(\frac{\partial^3 w}{\partial x^3} - \frac{d^3 w_0}{dx^3} \right) \frac{d^3(\delta w)}{dx^3} \right) dx + \\
& + EA \left(\frac{\partial u}{\partial x} + \frac{1}{2} \left(\frac{\partial w}{\partial x} \right)^2 - \frac{1}{2} \left(\frac{dw_0}{dx} \right)^2 \right) \delta u \Big|_0^L - EA \int_0^L \left(\frac{\partial}{\partial x} \left(\frac{\partial u}{\partial x} + \frac{1}{2} \left(\frac{\partial w}{\partial x} \right)^2 - \frac{1}{2} \left(\frac{dw_0}{dx} \right)^2 \right) \delta u \right) dx + \\
& + EA \left(\frac{\partial u}{\partial x} + \frac{1}{2} \left(\frac{\partial w}{\partial x} \right)^2 - \frac{1}{2} \left(\frac{dw_0}{dx} \right)^2 \right) \frac{\partial w}{\partial x} \delta w \Big|_0^L - EA \int_0^L \left(\frac{\partial}{\partial x} \left(\left(\frac{\partial u}{\partial x} + \frac{1}{2} \left(\frac{\partial w}{\partial x} \right)^2 - \frac{1}{2} \left(\frac{dw_0}{dx} \right)^2 \right) \frac{\partial w}{\partial x} \right) \delta w \right) dx + \\
& - EA \int_0^L \left(\left(\frac{\partial u}{\partial x} + \frac{1}{2} \left(\frac{\partial w}{\partial x} \right)^2 - \frac{1}{2} \left(\frac{dw_0}{dx} \right)^2 \right) \frac{dw_0}{dx} \frac{d(\delta w_0)}{dx} \right) dx + R \left(\frac{\partial^2 u}{\partial x^2} + \frac{\partial w}{\partial x} \frac{\partial^2 w}{\partial x^2} - \frac{dw_0}{dx} \frac{d^2 w_0}{dx^2} \right) \frac{\partial(\delta u)}{\partial x} \Big|_0^L + \\
& - R \int_0^L \left(\frac{\partial}{\partial x} \left(\frac{\partial^2 u}{\partial x^2} + \frac{\partial w}{\partial x} \frac{\partial^2 w}{\partial x^2} - \frac{dw_0}{dx} \frac{d^2 w_0}{dx^2} \right) \frac{\partial(\delta u)}{\partial x} \right) dx + R \left(\frac{\partial^2 u}{\partial x^2} + \frac{\partial w}{\partial x} \frac{\partial^2 w}{\partial x^2} - \frac{dw_0}{dx} \frac{d^2 w_0}{dx^2} \right) \frac{\partial^2 w}{\partial x^2} \delta w \Big|_0^L + \\
& - R \int_0^L \left(\frac{\partial}{\partial x} \left(\left(\frac{\partial^2 u}{\partial x^2} + \frac{\partial w}{\partial x} \frac{\partial^2 w}{\partial x^2} - \frac{dw_0}{dx} \frac{d^2 w_0}{dx^2} \right) \frac{\partial^2 w}{\partial x^2} \right) \delta w \right) dx + R \left(\frac{\partial^2 u}{\partial x^2} + \frac{\partial w}{\partial x} \frac{\partial^2 w}{\partial x^2} - \frac{dw_0}{dx} \frac{d^2 w_0}{dx^2} \right) \frac{\partial w}{\partial x} \frac{\partial(\delta w)}{\partial x} \Big|_0^L + \\
& - R \int_0^L \left(\frac{\partial}{\partial x} \left(\left(\frac{\partial^2 u}{\partial x^2} + \frac{\partial w}{\partial x} \frac{\partial^2 w}{\partial x^2} - \frac{dw_0}{dx} \frac{d^2 w_0}{dx^2} \right) \frac{\partial w}{\partial x} \right) \frac{\partial(\delta w)}{\partial x} \right) dx - R \int_0^L \left(\left(\frac{\partial^2 u}{\partial x^2} + \frac{\partial w}{\partial x} \frac{\partial^2 w}{\partial x^2} - \frac{dw_0}{dx} \frac{d^2 w_0}{dx^2} \right) \delta \left(\frac{dw_0}{dx} \frac{d^2 w_0}{dx^2} \right) \right) dx, \quad (\text{A.38})
\end{aligned}$$

Subsequently, and in order to include the effect of nonlinear geometric mid-plane stretching, we consider the following axial strain energy function due to residual axial stress denoted as U_A , and defined as follows:

$$U_A = \int_0^L \left\{ \sigma_A \int_A \varepsilon_{11} dA \right\} dx = \int_0^L \frac{N_0}{A} \left(\int_A \varepsilon_{11} dA \right) dx = \int_0^L N_0 \left(\frac{\partial u}{\partial x} + \frac{1}{2} \left(\frac{\partial w}{\partial x} \right)^2 - \frac{1}{2} \left(\frac{dw_0}{dx} \right)^2 \right) dx, \quad (\text{A.39})$$

where N_0/A represents the residual axial stress, mainly assumed to be uniformly distributed over the cross-sectional area of the beam. The above expression, as will be embedded in the equation of motion, would account for both linear part (normal force),

and the nonlinear part (mid-term stretching effect) of the residual stress force. Next, using Eq. (A.39), we can approximate the variational of the axial strain energy as follows:

$$\delta U_A = \int_0^L N_0 \left(\frac{\partial(\delta u)}{\partial x} + \frac{\partial w}{\partial x} \frac{\partial(\delta w)}{\partial x} \right) dx = N_0 \delta u + N_0 \frac{\partial w}{\partial x} \delta w \Big|_0^L - N_0 \int_0^L \frac{\partial^2 w}{\partial x^2} \delta w dx, \quad (\text{A.40})$$

The variational of kinetic energy function δT can simply be defined as:

$$\begin{aligned} \delta T &= \int_0^L \left(\frac{\partial u}{\partial t} \frac{\partial}{\partial t} \delta(u) + \frac{\partial w}{\partial t} \frac{\partial}{\partial t} \delta(w) \right) dx, \\ \int_{t_1}^{t_2} \delta T dt &= \rho A \left(\left[\int_0^L \frac{\partial u}{\partial t} \delta(u) dx \right]_{t_1}^{t_2} - \int_{t_1}^{t_2} \left(\int_0^L \frac{\partial^2 u}{\partial t^2} \delta(u) dx \right) dt + \left[\int_0^L \frac{\partial w}{\partial t} \delta(w) dx \right]_{t_1}^{t_2} - \int_{t_1}^{t_2} \left(\int_0^L \frac{\partial^2 w}{\partial t^2} \delta(w) dx \right) dt \right), \\ \int_{t_1}^{t_2} \delta T dt &= -\rho A \int_{t_1}^{t_2} \left(\int_0^L \frac{\partial^2 u}{\partial t^2} \delta(u) dx + \int_0^L \frac{\partial^2 w}{\partial t^2} \delta(w) dx \right) dt, \end{aligned} \quad (\text{A.41})$$

One assume that the terms with red arrow are much smaller than the quadratic integration terms then it could be neglected. The last component that will be included in Hamilton's principle is the work of non-conservative forces, denoted by δW , and can be expressed as:

$$\delta W = \int_0^L F_e(x, t) \delta w dx + \int_0^L F_{ax}(x, t) \delta u dx - C_s \int_0^L \frac{\partial^2 w}{\partial t \partial x} \delta w dx - C_v \int_0^L \frac{\partial w}{\partial t} \delta w dx, \quad (\text{A.42})$$

where F_e and F_{ax} symbolizes the electrostatic and axial forces, respectively, and the quantities C_s , and C_v are the structural and the viscous damping coefficient terms, respectively. Finally, we can get the CNT-based nanobeam equation of motion by substituting Eqs. (A.38), (A.40), (A.41), and (A.42) into the following extended Hamilton's principle equation:

$$\int_{t_1}^{t_2} \delta L dt = \int_{t_1}^{t_2} (\delta T - \delta U - \delta U_A + \delta W) dt = 0, \quad (\text{3.24})$$

From the above expression, by straightforwardly separating “ δu ” and “ δw ”, we impose two equation of motions represent the transversal displacement w and axial displacement u .

Derivation steps of transversal displacement:

$$\begin{aligned}
0 = & \rho A \frac{\partial^2 w}{\partial t^2} + P \left(\frac{\partial^4 w}{\partial x^4} - \frac{d^4 w_0}{dx^4} \right) - Q \left(\frac{\partial^6 w}{\partial x^6} - \frac{d^6 w_0}{dx^6} \right) - \frac{\partial}{\partial x} \left(EA \frac{\partial}{\partial x} \left(\frac{\partial u}{\partial x} + \frac{1}{2} \left(\frac{\partial w}{\partial x} \right)^2 - \frac{1}{2} \left(\frac{dw_0}{dx} \right)^2 \right) \right) + \\
& -R \frac{\partial}{\partial x} \left(\left(\frac{\partial^2 u}{\partial x^2} + \frac{\partial w}{\partial x} \frac{\partial^2 w}{\partial x^2} - \frac{dw_0}{dx} \frac{d^2 w_0}{dx^2} \right) \frac{\partial^2 w}{\partial x^2} \right) + R \frac{\partial^2}{\partial x^2} \left(\left(\frac{\partial^2 u}{\partial x^2} + \frac{\partial w}{\partial x} \frac{\partial^2 w}{\partial x^2} - \frac{dw_0}{dx} \frac{d^2 w_0}{dx^2} \right) \frac{\partial w}{\partial x} \right) + \\
& -N_0 \frac{\partial^2 w}{\partial x^2} + C_s \frac{\partial^2 w}{\partial t \partial x} + C_v \frac{\partial w}{\partial t} - F_e(x, t),
\end{aligned} \tag{A.44}$$

$$\begin{aligned}
0 = & \rho A \frac{\partial^2 w}{\partial t^2} + P \left(\frac{\partial^4 w}{\partial x^4} - \frac{d^4 w_0}{dx^4} \right) - Q \left(\frac{\partial^6 w}{\partial x^6} - \frac{d^6 w_0}{dx^6} \right) + \\
& - \frac{\partial}{\partial x} \left(\frac{\partial w}{\partial x} \left(N_0 + EA \left(\frac{\partial u}{\partial x} + \frac{1}{2} \left(\frac{\partial w}{\partial x} \right)^2 - \frac{1}{2} \left(\frac{dw_0}{dx} \right)^2 \right) - R \frac{\partial}{\partial x} \left(\frac{\partial^2 u}{\partial x^2} + \frac{\partial w}{\partial x} \frac{\partial^2 w}{\partial x^2} - \frac{dw_0}{dx} \frac{d^2 w_0}{dx^2} \right) \right) \right) + \tag{A.45} \\
& + C_s \frac{\partial^2 w}{\partial t \partial x} + C_v \frac{\partial w}{\partial t} - F_e(x, t),
\end{aligned}$$

$$\begin{aligned}
0 = & \rho A \frac{\partial^2 w}{\partial t^2} + P \left(\frac{\partial^4 w}{\partial x^4} - \frac{d^4 w_0}{dx^4} \right) - Q \left(\frac{\partial^6 w}{\partial x^6} - \frac{d^6 w_0}{dx^6} \right) + \\
& - \frac{\partial}{\partial x} \left(\frac{\partial w}{\partial x} \left(N_0 + EA \left(\frac{\partial u}{\partial x} + \frac{1}{2} \left(\frac{\partial w}{\partial x} \right)^2 - \frac{1}{2} \left(\frac{dw_0}{dx} \right)^2 \right) - R \frac{\partial^2}{\partial x^2} \left(\frac{\partial u}{\partial x} + \frac{1}{2} \left(\frac{\partial w}{\partial x} \right)^2 - \frac{1}{2} \left(\frac{dw_0}{dx} \right)^2 \right) \right) \right) + \tag{A.46} \\
& + C_s \frac{\partial^2 w}{\partial t \partial x} + C_v \frac{\partial w}{\partial t} - F_e(x, t),
\end{aligned}$$

The axial displacement can be written as:

$$\frac{\partial}{\partial x} \left(EA \left(\frac{\partial u}{\partial x} + \frac{1}{2} \left(\frac{\partial w}{\partial x} \right)^2 - \frac{1}{2} \left(\frac{dw_0}{dx} \right)^2 \right) - R \frac{\partial^2}{\partial x^2} \left(\frac{\partial u}{\partial x} + \frac{1}{2} \left(\frac{\partial w}{\partial x} \right)^2 - \frac{1}{2} \left(\frac{dw_0}{dx} \right)^2 \right) \right) + F_{ax}(x, t) = \rho A \frac{\partial^2 u}{\partial t^2} \delta u, \tag{A.47}$$

Note here that as the longitudinal dynamics is low prominent for a flexible structure as compared to its transverse dynamics, the inertia term in Eq. (A.47) can be assumed small and therefore can be neglected. Also note that in the above Eqs. (A.46) and (A.47), the internal axial force due to a temperature gradient is considered through the axial force function F_{ax} . For this, we consider the conventional thermal elasticity theory, where the thermal axial force can be written as follows $F_{ax} = EA\alpha_T\Delta T$, where α_T is the coefficient of thermal expansion (CTE) of the CNT, and ΔT is the temperature gradient. By rearranging Eq. (A.47),

$$\frac{\partial}{\partial x} \left(EA \left(\frac{\partial u}{\partial x} + \frac{1}{2} \left(\frac{\partial w}{\partial x} \right)^2 - \frac{1}{2} \left(\frac{dw_0}{dx} \right)^2 \right) \right) = R \frac{\partial^2}{\partial x^2} \left(\frac{\partial u}{\partial x} + \frac{1}{2} \left(\frac{\partial w}{\partial x} \right)^2 - \frac{1}{2} \left(\frac{dw_0}{dx} \right)^2 \right) + EA\alpha_T\Delta T, \quad (\text{A.48})$$

One substitutes the above expression into Eq. (A.46), the below expression can be obtained,

$$\begin{aligned} 0 = & \rho A \frac{\partial^2 w}{\partial t^2} + P \left(\frac{\partial^4 w}{\partial x^4} - \frac{d^4 w_0}{dx^4} \right) - Q \left(\frac{\partial^6 w}{\partial x^6} - \frac{d^6 w_0}{dx^6} \right) + \\ & - \frac{\partial}{\partial x} \left(\frac{\partial w}{\partial x} (N_0 + EA\alpha_T\Delta T) \right) + C_s \frac{\partial^2 w}{\partial t \partial x} + C_v \frac{\partial w}{\partial t} - F_e(x, t), \end{aligned} \quad (\text{A.49})$$

Then, we compute the internal axial force by integrating the axial stress of a discretionary beam cross-section as follows:

$$N = N_0 + \int_A E \varepsilon_{11} dA = N_0 + \int_A E \left(\frac{\partial u}{\partial x} + \frac{1}{2} \left(\frac{\partial w(x, t)}{\partial x} \right)^2 - \frac{1}{2} \left(\frac{dw_0(x)}{dx} \right)^2 \right) dA \quad (\text{A.50})$$

Assuming a uniformly distributed axial force induced by transverse deflection and zero external axial force ($N = 0$), the geometric nonlinearity due to the mid-plane stretching of

the beam along the x -axis can be described by the average of its stretching axial force over the whole beam length and shown in the integral-differential term, hence Eq. (A.50) reduces to:

$$N_0 = -\frac{EA}{2L} \int_0^L \left[\left(\frac{\partial w}{\partial x} \right)^2 - \left(\frac{dw_0}{dx} \right)^2 \right] dx \quad (\text{A.51})$$

Substituting Eq. (A.51) into Eq. (A.49), we get the subsequent equation of motion with its respective corresponding boundary conditions governing the transverse displacement of the CNT based nanobeam, and while considering both the size dependent parameters as well as the thermal gradient effects:

$$\begin{aligned} & \rho A \frac{\partial^2 w}{\partial t^2} + C_s \frac{\partial^2 w}{\partial t \partial x} + C_v \frac{\partial w}{\partial t} - Q \left(\frac{\partial^6 w}{\partial x^6} - \frac{d^6 w_0}{dx^6} \right) + P \left(\frac{\partial^4 w}{\partial x^4} - \frac{d^4 w_0}{dx^4} \right) + \\ & + \left(EA \alpha_T \Delta T - \frac{EA}{2L} \int_0^L \left[\left(\frac{\partial w}{\partial x} \right)^2 - \left(\frac{dw_0}{dx} \right)^2 \right] dx \right) \frac{\partial^2 w}{\partial x^2} = F_e(x, t), \end{aligned} \quad (\text{A.52})$$

$$w(0, t) = w(L, t) = 0, \quad \frac{\partial w}{\partial x} \Big|_{x=0} = \frac{\partial w}{\partial x} \Big|_{x=L} = 0, \quad \frac{\partial^2 w}{\partial x^2} \Big|_{x=0} = \frac{\partial^2 w}{\partial x^2} \Big|_{x=L} = 0, \quad (\text{A.53})$$

Note that in Eq. (A.53), the first four boundary conditions are the classical one and the last two are quoted as the non-classical one both associated with the clamped-clamped nanostructure. The electrostatic force function for a carbon nanotube under a parallel-plates electric field assumption can be written as [23-25, 95]:

$$F_e(x, t) = \frac{\pi \epsilon_0 (V_{dc} + V_{ac} \cos(\Omega t))^2}{\sqrt{(d-w-w_0)(d-w-w_0+2r)} \left(\cosh^{-1} \left(1 + (d-w-w_0)/r \right) \right)^2}, \quad (\text{A.54})$$

REFERENCES

1. <http://www.zyvex.com/nanotech/feynman.html>, 1959.
2. Iijima, S., *Helical microtubules of graphitic carbon*. Nature, 1991. **354**(6348): p. 56-58.
3. Sazonova, V., et al., *A tunable carbon nanotube electromechanical oscillator*. Nature, 2004. **431**(7006): p. 284-287.
4. Chiu, H.-Y., et al., *Atomic-Scale Mass Sensing Using Carbon Nanotube Resonators*. Nano Letters, 2008. **8**(12): p. 4342-4346.
5. Rueckes, T., et al., *Carbon Nanotube-Based Nonvolatile Random Access Memory for Molecular Computing*. Science, 2000. **289**(5476): p. 94-97.
6. Chaste, J., et al., *A nanomechanical mass sensor with yoctogram resolution*. Nat Nano, 2012. **7**(5): p. 301-304.
7. Moser, J., et al., *Ultrasensitive force detection with a nanotube mechanical resonator*. Nat Nano, 2013. **8**(7): p. 493-496.
8. Moser, J., et al., *Nanotube mechanical resonators with quality factors of up to 5 million*. Nat Nano, 2014. **9**(12): p. 1007-1011.
9. Thostenson, E.T., Z. Ren, and T.-W. Chou, *Advances in the science and technology of carbon nanotubes and their composites: a review*. Composites Science and Technology, 2001. **61**(13): p. 1899-1912.
10. Isaac Elishakoff, D.P., Kevin Dujat, Claudia Versaci, Giuseppe Muscolino, Joel Storch, Simon Bucas, Noel Challamel, Toshiaki Natsuki, *Carbon Nanotubes and Nanosensors, Vibration, Buckling and Ballistic Impact*. 2012: John Wiley & Sons, Inc.
11. Rafiee, R. and R.M. Moghadam, *On the modeling of carbon nanotubes: A critical review*. Composites Part B: Engineering, 2014. **56**: p. 435-449.
12. Dequesnes, M., S.V. Rotkin, and N.R. Aluru, *Parameterization of Continuum Theories for Single Wall Carbon Nanotube Switches by Molecular Dynamics Simulations*. Journal of Computational Electronics, 2002. **1**(3): p. 313-316.
13. Legoas, S.B., et al., *Molecular-Dynamics Simulations of Carbon Nanotubes as Gigahertz Oscillators*. Physical Review Letters, 2003. **90**(5): p. 055504.
14. Liew, K.M., X.Q. He, and C.H. Wong, *On the study of elastic and plastic properties of multi-walled carbon nanotubes under axial tension using molecular dynamics simulation*. Acta Materialia, 2004. **52**(9): p. 2521-2527.
15. Sears, A.T., *Carbon Nanotube Mechanics: Continuum Model Development from Molecular Mechanics Virtual Experiments*, in *Engineering Mechanics*. 2006, Virginia Polytechnic Institute and State University: Virginia.

16. Cao, G. and X. Chen, *Buckling of single-walled carbon nanotubes upon bending: Molecular dynamics simulations and finite element method*. Physical Review B, 2006. **73**(15): p. 155435.
17. Han, Y. and J. Elliott, *Molecular dynamics simulations of the elastic properties of polymer/carbon nanotube composites*. Computational Materials Science, 2007. **39**(2): p. 315-323.
18. Wan, H. and F. Delale, *A structural mechanics approach for predicting the mechanical properties of carbon nanotubes*. Meccanica, 2010. **45**(1): p. 43-51.
19. Alamusi, et al., *Prediction of thermal expansion properties of carbon nanotubes using molecular dynamics simulations*. Computational Materials Science, 2012. **54**: p. 249-254.
20. Sundararaghavan, V. and A. Waas, *Non-local continuum modeling of carbon nanotubes: Physical interpretation of non-local kernels using atomistic simulations*. Journal of the Mechanics and Physics of Solids, 2011. **59**(6): p. 1191-1203.
21. Lau, K.-T., et al., *On the effective elastic moduli of carbon nanotubes for nanocomposite structures*. Composites Part B: Engineering, 2004. **35**(2): p. 95-101.
22. Yakobson, B.I., C.J. Brabec, and J. Bernholc, *Nanomechanics of Carbon Tubes: Instabilities beyond Linear Response*. Physical Review Letters, 1996. **76**(14): p. 2511-2514.
23. Ouakad, H.M. and M.I. Younis, *Nonlinear dynamics of electrically actuated carbon nanotube resonators*. Journal of Computational and Nonlinear Dynamics, 2010. **5**(1): p. 1-13.
24. Ouakad, H.M. and M.I. Younis, *Natural frequencies and mode shapes of initially curved carbon nanotube resonators under electric excitation*. Journal of Sound and Vibration, 2011. **330**(13): p. 3182-3195.
25. Ouakad, H.M. and M.I. Younis, *Dynamic response of slacked single-walled carbon nanotube resonators*. Nonlinear Dynamics, 2011. **67**(2): p. 1419-1436.
26. Thai, H.-T., *A nonlocal beam theory for bending, buckling, and vibration of nanobeams*. International Journal of Engineering Science, 2012. **52**: p. 56-64.
27. Xu, T. and M.I. Younis, *Nonlinear Dynamics of Carbon Nanotubes Under Large Electrostatic Force*. Journal of Computational and Nonlinear Dynamics, 2015. **11**(2): p. 021009-021009.
28. Bouchaala, A., A.H. Nayfeh, and M.I. Younis, *Frequency Shifts of Micro and Nano Cantilever Beam Resonators Due to Added Masses*. Journal of Dynamic Systems, Measurement, and Control, 2016. **138**(9): p. 091002-091002.
29. Namazu, T., Y. Isono, and T. Tanaka, *Evaluation of size effect on mechanical properties of single crystal silicon by nanoscale bending test using AFM*. Journal of Microelectromechanical Systems, 2000. **9**(4): p. 450-459.

30. Fleck, N.A., et al., *Strain gradient plasticity: Theory and experiment*. Acta Metallurgica et Materialia, 1994. **42**(2): p. 475-487.
31. Yang, F., et al., *Couple stress based strain gradient theory for elasticity*. International Journal of Solids and Structures, 2002. **39**(10): p. 2731-2743.
32. Lam, D.C.C., et al., *Experiments and theory in strain gradient elasticity*. Journal of the Mechanics and Physics of Solids, 2003. **51**(8): p. 1477-1508.
33. Peddieson, J., G.R. Buchanan, and R.P. McNitt, *Application of nonlocal continuum models to nanotechnology*. International Journal of Engineering Science, 2003. **41**(3-5): p. 305-312.
34. Lei, J., et al., *Size-dependent vibration of nickel cantilever microbeams: Experiment and gradient elasticity*. AIP Advances, 2016. **6**(10): p. 105202.
35. Arash, B. and Q. Wang, *A review on the application of nonlocal elastic models in modeling of carbon nanotubes and graphenes*. Computational Materials Science, 2012. **51**(1): p. 303-313.
36. Lim, C.W., G. Zhang, and J.N. Reddy, *A higher-order nonlocal elasticity and strain gradient theory and its applications in wave propagation*. Journal of the Mechanics and Physics of Solids, 2015. **78**: p. 298-313.
37. Shaat, M. and A. Abdelkefi, *On a second-order rotation gradient theory for linear elastic continua*. International Journal of Engineering Science, 2016. **100**: p. 74-98.
38. Li, C. and T.-W. Chou, *Axial and radial thermal expansions of single-walled carbon nanotubes*. Physical Review B, 2005. **71**(23): p. 235414.
39. Zhang, C.-L. and H.-S. Shen, *Temperature-dependent elastic properties of single-walled carbon nanotubes: Prediction from molecular dynamics simulation*. Applied Physics Letters, 2006. **89**(8): p. 081904.
40. SINGH, B.P. and A. VERMA, *THERMAL EXPANSION IN SINGLE-WALLED CARBON NANOTUBES AT DIFFERENT TEMPERATURES*. International Journal of Nanoscience, 2008. **07**(06): p. 305-313.
41. Jiang, J.-W., J.-S. Wang, and B. Li, *Thermal expansion in single-walled carbon nanotubes and graphene: Nonequilibrium Green's function approach*. Physical Review B, 2009. **80**(20): p. 205429.
42. Ansari, R., M. Hemmatnezhad, and J. Rezapour, *The thermal effect on nonlinear oscillations of carbon nanotubes with arbitrary boundary conditions*. Current Applied Physics, 2011. **11**(3): p. 692-697.
43. Chen, W.-H., et al., *A theoretical investigation of thermal effects on vibrational behaviors of single-walled carbon nanotubes*. Computational Materials Science, 2012. **53**(1): p. 226-233.
44. Kang, D.-K., H.-I. Yang, and C.-W. Kim, *Thermal effects on mass detection sensitivity of carbon nanotube resonators in nonlinear oscillation regime*. Physica E: Low-dimensional Systems and Nanostructures, 2015. **74**: p. 39-44.

45. Truax, S., et al., *Axially Tunable Carbon Nanotube Resonators Using Co-integrated Microactuators*. Nano Letters, 2014. **14**(11): p. 6092-6096.
46. Li, M., H.X. Tang, and M.L. Roukes, *Ultra-sensitive NEMS-based cantilevers for sensing, scanned probe and very high-frequency applications*. Nat Nano, 2007. **2**(2): p. 114-120.
47. Hüttel, A.K., et al., *Carbon Nanotubes as Ultrahigh Quality Factor Mechanical Resonators*. Nano Letters, 2009. **9**(7): p. 2547-2552.
48. Eichler, A., et al., *Nonlinear damping in mechanical resonators made from carbon nanotubes and graphene*. Nat Nano, 2011. **6**(6): p. 339-342.
49. Island, J.O., et al., *Few-Hundred GHz Carbon Nanotube Nanoelectromechanical Systems (NEMS)*. Nano Letters, 2012. **12**(9): p. 4564-4569.
50. Kong, J., et al., *Nanotube Molecular Wires as Chemical Sensors*. Science, 2000. **287**(5453): p. 622-625.
51. Ilic, B., Y. Yang, and H.G. Craighead, *Virus detection using nanoelectromechanical devices*. Applied Physics Letters, 2004. **85**(13): p. 2604-2606.
52. Lin, Y., et al., *Advances toward bioapplications of carbon nanotubes*. Journal of Materials Chemistry, 2004. **14**(4): p. 527-541.
53. Domon, B. and R. Aebersold, *Mass Spectrometry and Protein Analysis*. Science, 2006. **312**(5771): p. 212-217.
54. Burg, T.P., et al., *Weighing of biomolecules, single cells and single nanoparticles in fluid*. Nature, 2007. **446**(7139): p. 1066-1069.
55. Naik, A.K., et al., *Towards single-molecule nanomechanical mass spectrometry*. Nat Nano, 2009. **4**(7): p. 445-450.
56. Fennimore, A.M., et al., *Rotational actuators based on carbon nanotubes*. Nature, 2003. **424**(6947): p. 408-410.
57. Fukuda, T., et al., *Nanofabrication, nanoinstrumentation and nanoassembly by nanorobotic manipulation*. International Journal of Robotics Research, 2009. **28**(4): p. 537-547.
58. Kuznetsov, S.S., Y.E. Lozovik, and A.M. Popov, *The nanoactuator based on a carbon nanotube*. Physics of the Solid State, 2007. **49**(5): p. 1004-1012.
59. Sudak, L.J., *Column buckling of multiwalled carbon nanotubes using nonlocal continuum mechanics*. Journal of Applied Physics, 2003. **94**(11): p. 7281-7287.
60. Zhang, Y.Q., G.R. Liu, and X.Y. Xie, *Free transverse vibrations of double-walled carbon nanotubes using a theory of nonlocal elasticity*. Physical Review B, 2005. **71**(19): p. 195404.
61. Wang, Q. and V.K. Varadan, *Vibration of carbon nanotubes studied using nonlocal continuum mechanics*. Smart Materials and Structures, 2006. **15**(2): p. 659.

62. Reddy, J.N., *Nonlocal theories for bending, buckling and vibration of beams*. International Journal of Engineering Science, 2007. **45**(2–8): p. 288-307.
63. Duan, W.H., C.M. Wang, and Y.Y. Zhang, *Calibration of nonlocal scaling effect parameter for free vibration of carbon nanotubes by molecular dynamics*. Journal of Applied Physics, 2007. **101**(2): p. 024305.
64. Lu, P., et al., *Application of nonlocal beam models for carbon nanotubes*. International Journal of Solids and Structures, 2007. **44**(16): p. 5289-5300.
65. Kumar, D., C. Heinrich, and A.M. Waas, *Buckling analysis of carbon nanotubes modeled using nonlocal continuum theories*. Journal of Applied Physics, 2008. **103**(7): p. 073521.
66. Reddy, J.N. and S.D. Pang, *Nonlocal continuum theories of beams for the analysis of carbon nanotubes*. Journal of Applied Physics, 2008. **103**(2): p. 023511.
67. Hu, Y.-G., et al., *Nonlocal shell model for elastic wave propagation in single- and double-walled carbon nanotubes*. Journal of the Mechanics and Physics of Solids, 2008. **56**(12): p. 3475-3485.
68. Narendar, S., D. Roy Mahapatra, and S. Gopalakrishnan, *Prediction of nonlocal scaling parameter for armchair and zigzag single-walled carbon nanotubes based on molecular structural mechanics, nonlocal elasticity and wave propagation*. International Journal of Engineering Science, 2011. **49**(6): p. 509-522.
69. Ansari, R. and S. Sahmani, *Small scale effect on vibrational response of single-walled carbon nanotubes with different boundary conditions based on nonlocal beam models*. Communications in Nonlinear Science and Numerical Simulation, 2012. **17**(4): p. 1965-1979.
70. Seyyed Fakhrabadi, M.M., A. Rastgoo, and M. Taghi Ahmadian, *Size-dependent instability of carbon nanotubes under electrostatic actuation using nonlocal elasticity*. International Journal of Mechanical Sciences, 2014. **80**: p. 144-152.
71. Seyyed Fakhrabadi, M.M., A. Rastgoo, and M.T. Ahmadian, *Nonlinear dynamic analysis of electrostatically actuated single-walled carbon nanotubes using nonlocal elasticity*. Latin American Journal of Solids and Structures, 2015. **12**(7): p. 1224-1240.
72. Ansari, R., J. Torabi, and M. Faghih Shojaei, *An efficient numerical method for analyzing the thermal effects on the vibration of embedded single-walled carbon nanotubes based on nonlocal shell model*. Mechanics of Advanced Materials and Structures, 2017: p. 0-0.
73. Tang, Y., Y. Liu, and D. Zhao, *Wave dispersion in viscoelastic single walled carbon nanotubes based on the nonlocal strain gradient Timoshenko beam model*. Physica E: Low-dimensional Systems and Nanostructures, 2017. **87**: p. 301-307.
74. Shaat, M. and A. Abdelkefi, *Reporting the sensitivities and resolutions of CNT-based resonators for mass sensing*. Materials & Design, 2017. **114**: p. 591-598.
75. Mindlin, R., *Influence of couple-stresses on stress concentrations*. Experimental Mechanics, 1963. **3**(1): p. 1-7.

76. Kong, S., et al., *The size-dependent natural frequency of Bernoulli–Euler micro-beams*. International Journal of Engineering Science, 2008. **46**(5): p. 427-437.
77. Wang, B., J. Zhao, and S. Zhou, *A micro scale Timoshenko beam model based on strain gradient elasticity theory*. European Journal of Mechanics - A/Solids, 2010. **29**(4): p. 591-599.
78. Kahrobaiyan, M.H., et al., *A nonlinear strain gradient beam formulation*. International Journal of Engineering Science, 2011. **49**(11): p. 1256-1267.
79. Akgöz, B. and Ö. Civalek, *Analysis of micro-sized beams for various boundary conditions based on the strain gradient elasticity theory*. Archive of Applied Mechanics, 2012. **82**(3): p. 423-443.
80. Seyyed Fakhrabadi, M.M., *Prediction of small-scale effects on nonlinear dynamic behaviors of carbon nanotube-based nano-resonators using consistent couple stress theory*. Composites Part B: Engineering, 2016. **88**: p. 26-35.
81. Kong, S., et al., *Static and dynamic analysis of micro beams based on strain gradient elasticity theory*. International Journal of Engineering Science, 2009. **47**(4): p. 487-498.
82. Binglei, W., et al., *Size-dependent pull-in instability of electrostatically actuated microbeam-based MEMS*. Journal of Micromechanics and Microengineering, 2011. **21**(2): p. 027001.
83. AKGÖZ, B. and Ö. CİVALEK, *Investigation of Size Effects on Static Response of Single-Walled Carbon Nanotubes based on Strain Gradient Elasticity*. International Journal of Computational Methods, 2012. **09**(02): p. 1240032.
84. Zhao, J., et al., *Nonlinear microbeam model based on strain gradient theory*. Applied Mathematical Modelling, 2012. **36**(6): p. 2674-2686.
85. Fakhrabadi, M.M.S., A. Rastgoo, and M.T. Ahmadian, *Dynamic behaviours of carbon nanotubes under dc voltage based on strain gradient theory*. Journal of Physics D: Applied Physics, 2013. **46**(40).
86. Fakhrabadi, M.M.S., A. Rastgoo, and M.T. Ahmadian, *Non-linear behaviors of carbon nanotubes under electrostatic actuation based on strain gradient theory*. International Journal of Non-Linear Mechanics, 2014. **67**: p. 236-244.
87. Farid, T., et al., *Size-dependent bistability of an electrostatically actuated arch NEMS based on strain gradient theory*. Journal of Physics D: Applied Physics, 2015. **48**(24): p. 245503.
88. Pradiptya, I. and H.M. Ouakad. *The effect of size scale parameters on the structural behavior of carbon nanotube based nano-actuator*. in *2016 12th IEEE/ASME International Conference on Mechatronic and Embedded Systems and Applications (MESA)*. 2016.
89. Mindlin, R.D., *Micro-structure in linear elasticity*. Archive for Rational Mechanics and Analysis, 1964. **16**(1): p. 51-78.

90. Mindlin, R.D., *Second gradient of strain and surface-tension in linear elasticity*. International Journal of Solids and Structures, 1965. **1**(4): p. 417-438.
91. Mir Masoud Seyyed, F., R. Abbas, and A. Mohammad Taghi, *Dynamic behaviours of carbon nanotubes under dc voltage based on strain gradient theory*. Journal of Physics D: Applied Physics, 2013. **46**(40): p. 405101.
92. Miandoab, E.M., et al., *Nano-resonator frequency response based on strain gradient theory*. Journal of Physics D: Applied Physics, 2014. **47**(36).
93. Miandoab, E.M., H.N. Pishkenari, and A. Yousefi-Koma, *Dynamic Analysis of Electrostatically Actuated Nanobeam Based on Strain Gradient Theory*. International Journal of Structural Stability and Dynamics, 2015. **15**(04): p. 1450059.
94. Jiang, H., et al., *Thermal Expansion of Single Wall Carbon Nanotubes*. Journal of Engineering Materials and Technology, 2004. **126**(3): p. 265-270.
95. Ouakad, H.M., *Nonlinear Structural Mechanics of Micro and Nano Systems*, in *Mechanical Engineering*. 2010, State University of New York: New York.
96. Mayoof, F.N. and M.A. Hawwa, *Chaotic behavior of a curved carbon nanotube under harmonic excitation*. Chaos, Solitons & Fractals, 2009. **42**(3): p. 1860-1867.
97. Kang, J.W., et al., *A study on carbon nanotube bridge as a electromechanical memory device*. Physica E: Low-dimensional Systems and Nanostructures, 2005. **27**(3): p. 332-340.
98. Üstünel, H., D. Roundy, and T.A. Arias, *Modeling a Suspended Nanotube Oscillator*. Nano Letters, 2005. **5**(3): p. 523-526.
99. Garcia-Sanchez, D., et al., *Mechanical Detection of Carbon Nanotube Resonator Vibrations*. Physical Review Letters, 2007. **99**(8): p. 085501.
100. Gibson, R.F., E.O. Ayorinde, and Y.-F. Wen, *Vibrations of carbon nanotubes and their composites: A review*. Composites Science and Technology, 2007. **67**(1): p. 1-28.
101. Belardinelli, P., S. Lenci, and M. Brocchini, *Modeling and analysis of an electrically actuated microbeam based on nonclassical beam theory*. Journal of Computational and Nonlinear Dynamics, 2014. **9**(3).
102. Younis, M.I., E.M. Abdel-Rahman, and A. Nayfeh, *A reduced-order model for electrically actuated microbeam-based MEMS*. Journal of Microelectromechanical Systems, 2003. **12**(5): p. 672-680.
103. Mook, A.H.N.a.D.T., *Nonlinear Oscillations*. 1979, New York: Wiley.
104. Duffy, D.G., *Advanced Engineering Mathematics with MATLAB*. 2010.
105. Ghayesh, M.H., *Nonlinear size-dependent behaviour of single-walled carbon nanotubes*. Applied Physics A: Materials Science and Processing, 2014. **117**(3): p. 1393-1399.

106. Pugno, N., C.H. Ke, and H.D. Espinosa, *Analysis of Doubly Clamped Nanotube Devices in the Finite Deformation Regime*. Journal of Applied Mechanics, 2004. **72**(3): p. 445-449.
107. Wang, L., et al., *The thermal effect on vibration and instability of carbon nanotubes conveying fluid*. Physica E: Low-dimensional Systems and Nanostructures, 2008. **40**(10): p. 3179-3182.
108. Lee, H.-L. and W.-J. Chang, *A closed-form solution for critical buckling temperature of a single-walled carbon nanotube*. Physica E: Low-dimensional Systems and Nanostructures, 2009. **41**(8): p. 1492-1494.
109. Nayfeh, A.H. and B. Balachandran, *Applied Nonlinear Dynamics*. 1995, New York: Wiley.

VITAE

Name : Iswan Pradiptya
Nationality : Indonesian
Date of birth : January 10th, 1989
Email : ipradiptya@gmail.com
Academic background : B.Sc. in Mechanical Engineering
University of Diponegoro, Indonesia
Affiliation : PT. PLN (Persero), Indonesia

Outcomes (in progress):

1. **Iswan Pradiptya**, Hassen M. Ouakad (2017), *Size-Dependent Behavior of Carbon Nanotube Actuator Based on the Higher-Order Strain Gradient Theory*, submitted to Journal of Sound and Vibrations (Elsevier).
2. **Iswan Pradiptya**, Hassen M. Ouakad (2017), *Nonlinear Dynamics of Doubly-clamped CNT-based Nanoresonator Considering Size Scale Dependent and Thermal Gradient Effect*, submitted to Journal of Computational and Nonlinear Dynamics (ASME).
3. **Iswan Pradiptya**, Hassen M. Ouakad (2016), *The Effect of Size Scale Parameters on The Structural Behavior of Carbon Nanotube based Nano-actuator*, 12th IEEE/ASME International Conference on Mechatronic and Embedded Systems and Applications (MESA), Auckland, New Zealand. (Accepted and published)
4. **Iswan Pradiptya**, I. Haryanto, A. Widodo (2016), *Extended Mathematical Model of Galloping-based Energy Harvester*, International Conference on Engineering, Science and Nanotechnology (ICESNANO 2016), Solo, Indonesia. (Accepted)
5. I. Haryanto, A. Widodo, T. Prahasto, D. Satrijo, **I. Pradiptya**, H.M. Ouakad (2017), *A finite element model of the galloping-based piezoaeroelastic energy harvester*, International Joint Conference on Advanced Engineering and Technology (IJCAET 2017), Bali, Indonesia. (Submitted)